OPTIMIZATION OF THE AERODYNAMICS OF SMALL-SCALE FLAPPING AIRCRAFT IN HOVER

by

Sidney Lebental

Department of Mechanical Engineering
and Materials Science
Duke University

Date: _____

Approved:

_____
Kenneth C. Hall, Supervisor

_____
Donald B. Bliss

_____
John Dolbow

_____
Laurens E. Howle

_____
Jonathan Protz

Dissertation submitted in partial fulfillment of the requirements
for the degree of Doctor of Philosophy in the
Department of Mechanical Engineering
and Materials Science in the
Graduate School of
Duke University

2008

ABSTRACT

OPTIMIZATION OF THE AERODYNAMICS OF SMALL-SCALE FLAPPING AIRCRAFT IN HOVER

by

Sidney Lebental

Department of Mechanical Engineering
and Materials Science
Duke University

Date: _____

Approved:

_____
Kenneth C. Hall, Supervisor

_____
Donald B. Bliss

_____
John Dolbow

_____
Laurens E. Howle

_____
Jonathan Protz

An abstract of a dissertation submitted in partial fulfillment of the
requirements for the degree of Doctor of Philosophy
in the Department of Mechanical Engineering
and Materials Science in the
Graduate School of
Duke University

2008

Copyright © 2008 by Sidney Lebental
All rights reserved

Abstract

Flapping flight is one of the most widespread mean of transportation. It is a complex unsteady aerodynamic problem that has been studied extensively in the past century. Nevertheless, by its complex nature, flapping flight remains a challenging subject. With the development of micro air vehicles, researchers need new computational methods to design these aircrafts efficiently.

In this dissertation, I will present three different methods of optimization for flapping flight with an emphasis on hovering with each their advantages and drawbacks. The first method was developed by Hall et al. It is an extremely fast and powerful three-dimensional approach. However, the assumptions made to develop this theory limit its use to lightly loaded wings. In addition, it only models the motion of the trailing edge and not the actual motion of the wing.

In a second part, I will present a two-dimensional unsteady potential method. It uses a freely convected wake which removes the lightly loaded restriction. This method shows the existence of an optimal combination of plunging and pitching motion. The motion is optimal in the sense that for a required force vector, the aerodynamic power is minimal.

The last method incorporates the three-dimensional effects. These effects are especially important for low aspect ratio wings. Thus, a three-dimensional unsteady potential vortex method was developed. This method also exhibits the presence of an optimal flapping/pitching motion. In addition, it agrees really well with the two previous methods and with the actual kinematics of birds during hovering flapping flight.

To conclude, some preliminary design tools for flapping wings in forward and hovering flight are presented in this thesis.

Contents

Abstract **iv**

List of Figures **x**

List of Tables **xvii**

Acknowledgements **xx**

I Introduction **1**

I.1 General introduction 1

I.2 Dimensional analysis 2

I.3 Objectives 3

I.4 Outline of the thesis 4

II Literature Review **6**

II.1 Dimensional analysis overview 6

II.2 Kinematics and aerodynamic forces production 12

II.2.1 Biological study 12

a Forward flight case 12

b Hovering case 16

II.2.2 Experimental study 19

a Forward flight case 19

b Hovering case 19

II.2.3 Computational study 22

a Analytical methods 22

b Potential methods 23

b.1 Forward flight case 23
b.2 Hovering case 25
c Full Navier-Stokes methods 25
c.1 Forward flight case 25
c.2 Hovering case 28
II.3 Power requirements 29
III A Wake Approach to the Constrained Optimization Problem 36
III.1 Problem description 36
III.2 Approach 37
III.2.1 Minimizing the induced power 38
III.2.2 Minimizing the viscous power 43
III.2.3 The hovering case 48
III.3 Results 49
III.3.1 Stroke angle 49
III.3.2 Flapping frequency 51
IV Two-Dimensional Potential Method 55
IV.1 Problem description 55
IV.2 Literature review 55
IV.3 Approach 58
IV.3.1 Kinematics 58
IV.3.2 Potential method 59
a Inviscid formulation 59
b Viscous formulation 65
IV.3.3 Convergence study 66

a Small amplitudes 66
a.1 Sudden change in pitch 68
a.2 Plunging motion 69
a.3 Pitching motion 71
b Wake patterns 74
c Large amplitude in hover 76
c.1 Number of cycles 76
c.2 Number of iterations with the freestream on . 80
c.3 Number of panels 80
c.4 Number of points per cycle 81
c.5 Freestream velocity 82
c.6 Conclusion 82
IV.4 Results 82
IV.4.1 Inviscid case 84
IV.4.2 Viscous model 1 86
IV.4.3 Viscous model 2 90
V Three-Dimensional Potential Method 93
V.1 Problem description 93
V.2 Literature review 93
V.3 Approach 94
V.3.1 Kinematics 94
V.3.2 Potential method 95
a Inviscid formulation 95
a.1 Governing equations 95

a.2 Laplace's equation 97
a.3 Poisson's equation 100
a.4 The Kutta condition 103
a.5 The wake description 103
b Viscous formulation 109
V.3.3 Convergence study 110
a High aspect ratio with small amplitudes 110
a.1 Sudden change in pitch 110
a.2 Plunging motion 112
a.3 Pitching motion 118
b Finite aspect ratio wing 120
b.1 Vortex rings versus vortons in the wake 120
b.2 Sudden change of pitch for finite aspect ratio wings 123
c Convergence in hovering 125
c.1 Convergence in time 125
c.2 Cut-off radius 128
c.3 ϵ in vortex line 130
c.4 Freestream velocity 132
c.5 Number of iterations with the freestream on . 134
c.6 Time step 136
c.7 Number of panels in the chordwise direction . 138
c.8 Number of panels in the spanwise direction . 140
c.9 Parameters used 142

V.4 Results 142

V.4.1 Inviscid case 142

a Optimum motion 142

b Comparative study 149

V.4.2 Viscous model 2 155

VI Conclusion and Recommendations **158**

VI.1 Conclusion 158

VI.2 Further research 159

A Flow relations **161**

A.1 Potential flow identity 161

A.2 Actuator disk theory 161

B Mathematical methods **163**

B.1 Newton's Method 163

Bibliography **164**

Biography **170**

List of Figures

I.1 Data collected on various hovering flappers plotted as $\Pi_2 = f(\Pi_6)$. . 3

II.1 The great flight diagram. Reprinted from Tennekes [1]. 7

II.2 The relation between weight and wing loading represented in a proportional diagram. When the weight increases by a factor of 100, the wing loading increases by a factor of 5 and the forward speed by a factor of more than 2. Reprinted from Tennekes [1]. 9

II.3 Log-log plot of observed wingbeat frequency for various birds versus the frequency parameter. Reprinted from Pennycuick [2]. 11

II.4 Log-log plot of observed wingbeat wavelength for various birds versus the frequency parameter. Reprinted from Pennycuick [2]. 11

II.5 Spanwise vorticity contour with superimposed velocity field for three flight speeds $(5, 8, 11 m.s^{-1})$. Reprinted from Rosen [3]. 14

II.6 Vortex loop formation by Drosophilia. Reprinted from Dickinson [4]. 16

II.7 Clap and Fling mechanism. Dark arrows show the induced velocities, the light arrows the net force and the dark lines are the flow lines. Reprinted from Sane [5]. 17

II.8 Schema of thrust enhancement through the fling mechanism. The left drawing is an airfoil in upward plunging motion, the right drawing is an airfoil in upward plunging motion with the presence of the two vortices due to the fling. Dark arrows show the induced velocities, the light arrows the net force and the dark lines are the flow lines. . 18

II.9 Wing rotation mechanism. Reprinted from Dickinson [6]. 20

II.10 Development of vorticity during a stroke reversal for an axis of rotation located respectively at 0.8, 0.5, 0.2 chord (A, B, C). Reprinted from Dickinson [6]. 21

II.11 Force and moment coefficients versus α. The airfoil is pitching in freestream. Pitching rates (Ω^+) of 2.4, 1.6 and 0.5 are shown as squares, triangles and circles, respectively. Results for $Re = 100$ and $Re = 100000$ are shown as solid and dashed lines, respectively. Reprinted from Hamdani [7]. 28

II.12 The idealized lifting line power curve. Reprinted from Rayner [8]. . 32

II.13 Wake geometry and lift, thrust production as a function of the circulation model. Reprinted from Rayner [8]. 33

III.1 Rear view of the wings. The solid lines represent the position of the wing at the end of the upstroke and the dashed line at the end of the downstroke. 36

III.2 Control volume enclosing one period of the far wake. 39

III.3 ${C_l/C_{d0}}^2$ function of the angle of attack for different symmetrical airfoils at $Re = 1000$. 45

III.4 ${C_l/C_{d0}}^2$ function of the angle of attack for different non-symmetrical airfoils at $Re = 1000$. 45

III.5 Drag Polar for NACA 0009 for $Re_c = 3000, 5000, 8000$, the scaled C_d are scaled by $\sqrt{3000/Re_c}$. 47

III.6 Drag polar of Equation III.32 for three Reynolds numbers (3,000, 5,000, 8,000). 48

III.7 Coefficients of Power function of the flapping frequency. 53

III.8 Wing shape. 53

III.9 Rear view of optimal circulation distribution in the wake. 54

III.10 Top view of optimal circulation distribution in the wake. 54

IV.1 Schematic of the Jones et al. panel code. Reprinted from Jones [9]. 56

IV.2 Kinematics of the flat plate used in the present method 59

IV.3 Flat plate with linear vorticity distribution and its wake. 60

IV.4 Non dimensional lift for a sudden change in pitch. 69

IV.5 Wake pattern for a reduced frequency $k = \frac{\varpi c}{U} = 3.0$ and a plunging amplitude $h = 0.2$ obtained by Jones et al. [9]. 75

IV.6 Wake pattern for a reduced frequency $k = \frac{\varpi c}{U} = 3.0$ and a plunging amplitude $h = 0.2$ obtained with the present method. 75

IV.7 Wake patterns obtained by Platzer et al. [10] on the left side for various reduced frequencies $k = \frac{\varpi c}{U}$; wake patterns for the same conditions obtained with the present method on the right side. . . . 76

IV.8 Mean coefficient of power taken over one cycle as a function of the number of cycles elapsed. 79

IV.9 Mean coefficient of thrust taken over one cycle as a function of the number of cycles elapsed. 79

IV.10 *FOM* for a required coefficient of thrust function of the pitch angle and the pitch phase advance in the inviscid case. 85

IV.11 Non-dimensional flapping frequency ($\tilde{f}$) for a required coefficient of thrust function of the pitch angle and the pitch phase advance in the inviscid case. 85

IV.12 Drag polar of Equation IV.46 for three Reynolds numbers (3,000, 5,000, 8,000). 87

IV.13 *FOM* for a required coefficient of thrust function of the pitch angle and the pitch phase advance in the viscous 1 case. 89

IV.14 Non-dimensional flapping frequency ($\tilde{f}$) for a required coefficient of thrust function of the pitch angle and the pitch phase advance in the viscous 1 case. 89

IV.15 *FOM* for a required coefficient of thrust function of the pitch angle and the pitch phase advance in the viscous 2 case. 91

IV.16 Non-dimensional flapping frequency ($\tilde{f}$) for a required coefficient of thrust function of the pitch angle and the pitch phase advance in the viscous 2 case. 91

V.1 Schema of the wing. 94

V.2 Discretization of the wings using quadrilateral panels. The crosses are the collocation points. 98

V.3 Influence of a straight vortex line at point $P(x, y, z)$. 100

V.4 Regularization function $\xi(x)$ in V.24 with $\sigma = 0.1$. 101

V.5 Description of the near and far wake. The solid lines represent the wing, the dashed lines are the vortex rings of the near wake, the dots are the vortons. 105

V.6 Six models for the conversion of the near wake rings into vortons. The dashed lines are the vortex rings in the wake, the solid rectangle in the wake is the volume of integration and the double lined arrow is vortex line not included in the integration. 106

V.7 Notation for a ring panel. 107

V.8 Non dimensional lift for a sudden change in pitch. 112

V.9 "A description of the unknown and known buffer wake regions at the trailing edge of a wing. Notice also the conversion of the line vortices resulting from the constant strength dipoles, into point vortices." Reprinted from Willis et al. [11]. 116

V.10 Coefficient of lift function of time for a wing of aspect ratio $AR = 3$ undergoing flapping motion of $\phi_1 = 0.2°$ at a reduced frequency of $k = 0.0393$. The solid line represents the result with the ring method, the dotted lines the results using vortons with a frozen wake and dash-dot lines the results using vortons with a free wake. 121

V.11 Coefficient of thrust function of time for a wing of aspect ratio $AR = 3$ undergoing flapping motion of $\phi_1 = 0.2°$ at a reduced frequency of $k = 0.0393$. The solid line represents the result with the ring method, the dotted lines the results using vortons with a frozen wake and dash-dot lines the results using vortons with a free wake. 122

V.12 Coefficient of power function of time for a wing of aspect ratio $AR = 3$ undergoing flapping motion of $\phi_1 = 0.2°$ at a reduced frequency of $k = 0.0393$. The solid line represents the result with the ring method, the dotted lines the results using vortons with a frozen wake and dash-dot lines the results using vortons with a free wake. 122

V.13 The C_L evolution with time due to a sudden change of pitch. The top plot is reprinted from Willis et al. [11]. The (*) markers are results of Katz and Plotkin [12]. The bottom plot was obtained with present method. 124

V.14 Coefficient of thrust in hover for a wing in test configuration. 127

V.15 Coefficient of power in hover for a wing in test configuration. 127

V.16 Coefficient of thrust in hover for a wing in test configuration for different cut-off radii. 129

V.17 Coefficient of power in hover for a wing in test configuration for different cut-off radii. 129

V.18 Coefficient of thrust in hover for a wing in test configuration for different ϵ_K. 131

V.19 Coefficient of power in hover for a wing in test configuration for different ϵ_K. 131

V.20 Coefficient of thrust in hover for a wing in test configuration for different starting reduced frequencies. 133

V.21 Coefficient of power in hover for a wing in test configuration for different starting reduced frequencies. 133

V.22 Coefficient of thrust in hover for a wing in test configuration for different number of iterations with the freestream on (IT_{start}). . . . 135

V.23 Coefficient of power in hover for a wing in test configuration for different number of iterations with the freestream on (IT_{start}). . . . 135

V.24 Coefficient of thrust in hover for a wing in test configuration for different number of iterations per cycle (NTS). 137

V.25 Coefficient of power in hover for a wing in test configuration for different number of iterations per cycle (NTS). 137

V.26 Coefficient of thrust in hover for a wing in test configuration for different number of panels in the chordwise direction (N_i). 139

V.27 Coefficient of power in hover for a wing in test configuration for different number of panels in the chordwise direction (N_i). 139

V.28 Coefficient of thrust in hover for a wing in test configuration for different number of panels in the spanwise direction (N_j). 141

V.29 Coefficient of power in hover for a wing in test configuration for different number of panels in the spanwise direction (N_j). 141

V.30 FOM for a required coefficient of thrust function of the pitch angle and the pitch phase advance in the inviscid case. 144

V.31 Flapping frequency for a required coefficient of thrust function of the pitch angle and the pitch phase advance in the inviscid case. 144

V.32 Non-dimensional shed circulation for one converged flapping period along the non-dimensional span using Hall's method. 146

V.33 Non-dimensional shed circulation for one converged flapping period along the non-dimensional span using the present method. 146

V.34 Contour plot of the non-dimensional shed circulation for one converged flapping period along the non-dimensional span using Hall's method. 147

V.35 Contour plot of the non-dimensional shed circulation for one converged flapping period along the non-dimensional span using the present method. 147

V.36 Top view of the half wing and the vortons shed from the tip and midspan in the optimum motion case, for a non-dimensional flapping frequency of 0.97. 149

V.37 "Schematic diagram of the flapping *Drosophila* wing. The position of the wing is shown at three different times during the flapping cycle. The coordinate system $(x', y'z')$ is fixed to the wing, and the wing rotates about the z' axis throughout the cycle. R wing length; ϕ wingbeat amplitude." Reprinted from Ramamurti and Sandberg [13] 150

V.38 Kinematics of the flapping wing used by Ramamurti and Sandberg. From left to right, stroke and pitch angle; translational velocity of the wing tip and angular velocity; translational acceleration of the wing tip and angular acceleration as functions of time. Reprinted from Ramamurti and Sandberg [13]. 151

V.39 Kinematics of the flapping wing used in the present method. From left to right, stroke and pitch angle; translational velocity of the wing tip and angular velocity; translational acceleration of the wing tip and angular acceleration as functions of time. 151

V.40 Thrust as a function of time for one flapping period. The red lines are from Ramamurti and Sandberg [13] and the blue lines from Dickinson et al. [14]. Reprinted from Ramamurti and Sandberg [13]. 152

V.41 Thrust as a function of time for one flapping period using the present method. 152

V.42 Thrust as a function of time for one symmetrical flapping cycle in the inviscid case and in the viscous case computed by Ramamurti and Sandberg [13]. Reprinted from Ramamurti and Sandberg [13]. . 155

V.43 *FOM* for a required coefficient of thrust function of the pitch angle and the pitch phase advance in the viscous 2 case. 156

V.44 Flapping frequency for a required coefficient of thrust function of the pitch angle and the pitch phase advance in the viscous 2 case. . . . 156

A.1 Actuator disk theory. 162

List of Tables

III.1 Optimal coefficient of power as a function of the stroke angle. 50

IV.1 Error for the mean coefficient of thrust, power and peak lift coefficient obtained by the present two-dimensional method compared to the results of Theodorsen [15] and Garrick [16] for a pure plunging motion. 70

IV.2 Error for the mean coefficient of power and its peak obtained by the present two-dimensional method compared to the results of Theodorsen [15] and Garrick [16] for a pure plunging motion. 71

IV.3 Error for the mean coefficient of thrust, power and peak lift coefficient obtained by the present two-dimensional method compared to the results of Theodorsen [15] and Garrick [16] for a pure pitching motion about the elastic axis. 72

IV.4 Error for the mean coefficient of thrust and its peak obtained by the present two-dimensional method compared to the results of Theodorsen [15] and Garrick [16] for a pure pitching motion about the elastic axis. 73

IV.5 Averaged mean coefficients of thrust and power taken over cycles 10 to 19 or 20 to 29 and their standard deviations. 78

IV.6 Averaged mean coefficients of thrust and power taken over cycles 25 to 29, their standard deviations and their relative change due to an increase in number of panels. 80

IV.7 Averaged mean coefficients of thrust and power taken over cycles 10 to 19 or 20 to 29 with $N = 50$, their standard deviations and their relative change due to a decrease in time step. 81

IV.8 Averaged mean coefficients of thrust and power taken over cycles 10 to 19 with $N = 50$, $NTS = 50$, their standard deviations and their relative change due to an increase in k_{start}. 82

V.1 Error for the mean coefficient of thrust, power and peak lift coefficient obtained by the present three-dimensional method with $AR = 100$ compared to the results of Theodorsen [15] and Garrick [16] for a pure plunging motion. 114

V.2 Error for the mean coefficient of power and its peak obtained by the present three-dimensional method with $AR = 100$ compared to the results of Theodorsen [15] and Garrick [16] for a pure plunging motion. 115

V.3 Error for the mean coefficient of thrust, power and peak lift coefficient obtained by the present three-dimensional method with $AR = 100$ and $c_w = 0.5$ compared to the results of Theodorsen [15] and Garrick [16] for a pure plunging motion. 117

V.4 Error for the mean coefficient of thrust, power and peak lift coefficient obtained by the present three-dimensional method with $AR = 100$ compared to the results of Theodorsen [15] and Garrick [16] for a pure pitching motion about the elastic axis. 119

V.5 Error for the mean coefficient of thrust and its peak obtained by the present three-dimensional method with $AR = 100$ compared to the results of Theodorsen [15] and Garrick [16] for a pure pitching motion about the elastic axis. 120

V.6 Averaged mean coefficients of thrust and power for different averaging. 126

V.7 Averaged mean coefficients of thrust and power for different cut-off radii. The relative change is computed for an increase in cut-off radius. 128

V.8 Averaged mean coefficients of thrust and power for different ϵ_K. The relative change is computed for a decrease in ϵ_K. 130

V.9 Averaged mean coefficients of thrust and power for different starting velocities. The relative change is computed for a decrease in the reduced frequency. 132

V.10 Averaged mean coefficients of thrust and power for different IT_{start}. The relative change is computed for an increase in the number of iterations. 134

V.11 Averaged mean coefficients of thrust and power for different NTS. The relative change is computed for an increase in NTS. 136

V.12 Averaged mean coefficients of thrust and power for different N_i. The relative change is computed for an increase in the number of panels. 138

V.13 Averaged mean coefficients of thrust and power for different N_j. The relative change is computed for an increase in the number of panels. 140

Acknowledgements

I would like to thank a number of people who made this work possible. First, I would like to acknowledge my advisor Dr. Kenneth C. Hall for his guidance, his availability and his advice. Additionally, I would like to acknowledge the other four members of my committee, Dr. Donald B. Bliss, Dr. John Dolbow, Dr. Laurens E. Howle and Dr. Jonathan Protz for their review of this thesis.

I would also like to thank some of my friends and my family for their support.

Nomenclature

A	Surface bounding Trefftz volume
AR	Aspect ratio
B	Wingspan
C_L, C_T, C_P	Coefficients of lift, drag and power
C_d, C_l	Sectional drag and lift coefficients
C_{d0}	Parameter of drag coefficient curve fit
FOM	Figure of merit
L	Time-averaged lift
N	Number of panels on the plate or wing
N_i	Number of panels in the chordwise direction
N_j	Number of panels in the spanwise direction on a half-wing
N_{wake}	Number of panels in the wake
P	Time-averaged power
P_i, P_v	Time-averaged induced and viscous power
Re_c	Reynolds number based on the chord
S	Time-averaged aerodynamic side force
T	Time-averaged thrust
U	Flight velocity
V	Relative velocity of airfoil through fluid

V_{ij}	Fluid velocity induced at the ith panel by a unit-strength vortex ring at the jth panel
W	Upper surface of one period of the wake
ΔA_i	Area of the vortex lattice element
Δ_w	Length of a wake panel
Δ	Length of an airfoil panel
Γ	Circulation
Π_i	Lagrangian inviscid power
α	Angle of attack
ϵ	Vortex filament cut-off radius
γ	Vortex distribution over the airfoil
γ_w	Vortex distribution in the wake
$(\vec{e_x}, \vec{e_y}, \vec{e_z})$	Cartesian unit vectors
μ	Dynamic fluid viscosity
ν	Inequality constraint Lagrange multiplier, kinematic fluid viscocity
ϕ	Stroke angle, pitch phase shift
ρ	Fluid density
σ	Blob cut-off radius
θ	Pitch Angle
φ	Velocity potential
ϖ	Flapping angular velocity

$\vec{F}$	Time-averaged aerodynamic force vector
$\vec{\lambda}$	Vector of equality constraint Lagrange multipliers
$\vec{\xi}$	Kelvin linear impulse
$\vec{n}$	Unit normal vector
$\vec{w}$	Induced wash
b	Half chord
c	Aerodynamic chord
dt	Time-step size
e	Location of the pitch axis
f	Flapping frequency
g	Half-gap separating the two half-wings
h	Amplitude of the plunging motion
k	Reduced frequency
l	Sectional lift
m	Mass per unit length
s	Distance along airfoil path
T	Flapping period
V	Trefftz volume
W	Diagonal weighting matrix used in augmented Lagragian formulation

Chapter I

Introduction

I.1 General introduction

Flapping is one of the most complex modes of transportation; nevertheless, it is the most widespread among animals. Over a million of different species of insects fly and three-quarter of the warm blooded vertebrates fly. Flying animals take advantage of the three-dimensionality of the world compared to walking animals. Nature seems to have developed over 150 million years a really efficient way of flying. As a comparison, humans move at a top speed of 3-4 body lengths per second; the fastest mammal (Cheetah) can reach speeds of 75mph which is about 25 body lengths per second; a supersonic aircraft such as the SR-71 reaches speed of Mach 3, which is about 32 body lengths per second. While a common pigeon flies at 50mph which translates into 75 body lengths per second and swifts 140 body lengths per second. In addition to speed, flyers have a great maneuverability. Acrobatic aircraft can reach roll rates of 720 degrees per second compared to the Barn swallow which can have roll rates of 5000 degrees per second. According to Shyy et al. [17], birds can withstand acceleration 10-14 Gs compared to military aircraft 8-10 Gs.

To achieve these aerodynamic capabilities, flappers have developed complex kinematics and aeroelastic interactions. Tucker [18], Greenewalt [19], Pennycuick [20, 2] and more recently Spedding et al. [21, 3] and Dickinson et al. [22, 4] have studied the mechanisms of flapping for various birds and insects.

Engineers have only recently considered flapping as a mean of transportation for man-made vehicles. Small airborne vehicles usually called MAVs (Micro Air Vehicles) are defined by Spedding et al. [23] as flying vehicles with no overall dimension larger than 15cm and a weight restriction of 100g. These MAVs operate under low Reynolds number ($10^4 - 10^5$) and need a high maneuverability. They perform sensing missions and thus need the capability

of hovering. More recently, even smaller vehicles (NAVs: Nano Air Vehicles) became of interest. They have a span of 7.5cm and a weight of 10g. Thus new tools are needed to analyze the dynamic of these small flappers at low Reynolds number.

This thesis investigates aerodynamic tools for low Reynolds number flapping airfoils and wings especially in the case of a typical NAV. A particular emphasis on hovering will be presented.

I.2 Dimensional analysis

We first can perform a dimensional analysis using the Buckingham's Π theorem to extract meaningful parameters in the case of hovering flapping flight.

We have 8 variables for 3 fundamental dimensions, thus we can find 5 non-dimensional Π groups.

	ρ	B	ϖ	T	P	c	μ	ϕ
m	1	0	0	1	1	0	1	0
l	-3	1	0	1	2	1	-1	0
t	0	0	-1	-2	-3	0	-1	0

$$\begin{aligned}
\Pi_1 &= \frac{B}{c} \\
\Pi_2 &= \frac{T}{\rho B^4 \varpi^2 \left(\frac{\phi}{\pi}\right)^3} \\
\Pi_3 &= \frac{P}{\rho B^5 \varpi^3 \left(\frac{\phi}{\pi}\right)^4} \\
\Pi_4 &= \frac{\rho B^2 \varpi \left(\frac{\phi}{\pi}\right)}{\mu} \\
\Pi_5 &= \phi
\end{aligned} \tag{I.1}$$

Since each Π parameter is function of the others, we can form a new Π group that will be independent of the frequency by combining for example Π_2 and Π_4:

$$\Pi_6 = \Pi_2 \Pi_4^2 = \frac{\rho T}{\frac{\phi}{\pi}\mu^2} \tag{I.2}$$

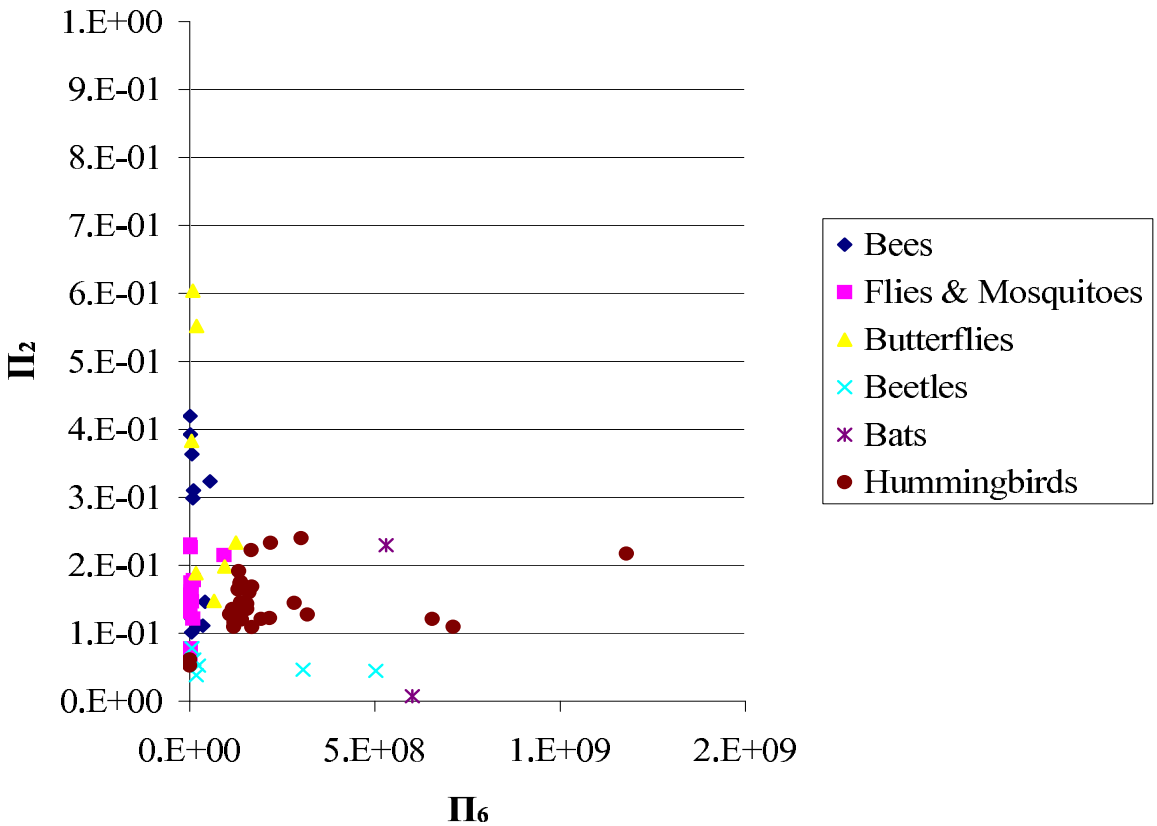

Figure I.1: Data collected on various hovering flappers plotted as $\Pi_2 = f(\Pi_6)$.

We gathered data collected by Altshuler et al. [24, 25], Dudley [26], Wells [27], Chai and Millard [28], Norberg et al. [29], Mao and Gang [30], Betts and Wootton [31] and Weis-Fogh [32] on various hovering flappers. These data are plotted in a graph ($\Pi_2 = f(\Pi_6)$). As seen on Figure I.1, most of the flappers have a non dimensional thrust (Π_2) that lies in a narrow band extending form 0.1 to 0.25.

I.3 Objectives

The goal of this thesis and the project behind it is to develop a set of computational tools that can be used in the design of small flapping vehicles. We are especially interested in the hovering flapping flight. In the present literature there is a lack of practical tools. A practical tool could be defined as a program used in the preliminary design phase. This

method needs to be computationally not too expensive (less than a day of computation). Dickinson [6, 14, 4, 22] studied hovering on his fly model using a quasi-steady analysis. Mao et al. [30] and Ramamurti et al. [13] used unsteady Navier-Stokes method to solve the hovering problem. These methods usually take days before reaching convergence. Having a less expensive unsteady method that gives good results as a preliminary tool could save a lot of time before using the full Navier-Stokes solver for a refined solution.

I.4 Outline of the thesis

The present thesis can be divided into three main parts. Each parts being an improvement of the previous part. The first part uses the theory developed by Hall et al. [33, 34]. Some modifications and features were added. This method gives really good first estimates of the inviscid and to some extend viscous power required to perform hovering flapping flight for a prescribed force. Nevertheless, it is based on simplifying assumptions that are good for lightly loaded flappers but become problematic in hovering flight because the roll-up of the wake is neglected. The wake is convected downstream with the forward flight velocity. In the case of hovering flight, an artificial convecting velocity is used based on the actuator disk theory.

Consequently, we first developed a two-dimensional potential method that uses a free wake. The flat plate is modeled using linear strength vortex elements and the wake using constant strength vortex panels. Thus, the wake is convected with the local induced velocities. The correction for the viscosity is based on the same principles as in the previous model. The limitation of this method resides in its two-dimensionality. Small flappers usually have low aspect ratio wings thus, the three-dimensional effects are important. Therefore, a three-dimensional method that uses a free wake would improve the quality of the solution.

Finally, in the last part, we present a three-dimensional vortex method. It is also a potential method but based on the vortex theory. It uses vortex rings over the wing

(equivalent to doublet panels) and vortons in the wake. Vortons can be viewed as non-singular volume of vorticity. In this case, the flow is three-dimensional and no artificial convection velocity is used since the wake is convected with the local induced velocity field. We will show that the three methods give results that agree with each other. This last method could be used as a preliminary design code.

Chapter II

Literature Review

II.1 Dimensional analysis overview

When it comes to flying, it is interesting to study the influence of different parameters (geometrical or kinematics). For example, we can notice that bigger animals usually have to fly faster. As an obvious example, a Boeing 747 flies 100 times faster than a fruit fly. Tennekes [1] studied the influence of these parameters. He gathered the correlation between the size and the flight speed of animals and airplanes into a diagram sometimes referred as *"The Great Flight Diagram"* shown in Figure II.1. Plotted is the weight versus the cruising speed. One observes that there is a high correlation for a wide range of variation in weight and flight speed. The range goes from the fruit fly weighting $7 \times 10^{-6} N$, with a wing area of $2mm^2$ and a flight velocity of $3m.s^{-1}$, to a Boeing 747 having a weight of 500 billion times the fruit fly, a wing areas of 250 million times as large and a cruising speed 100 times the flight speed of the fly.

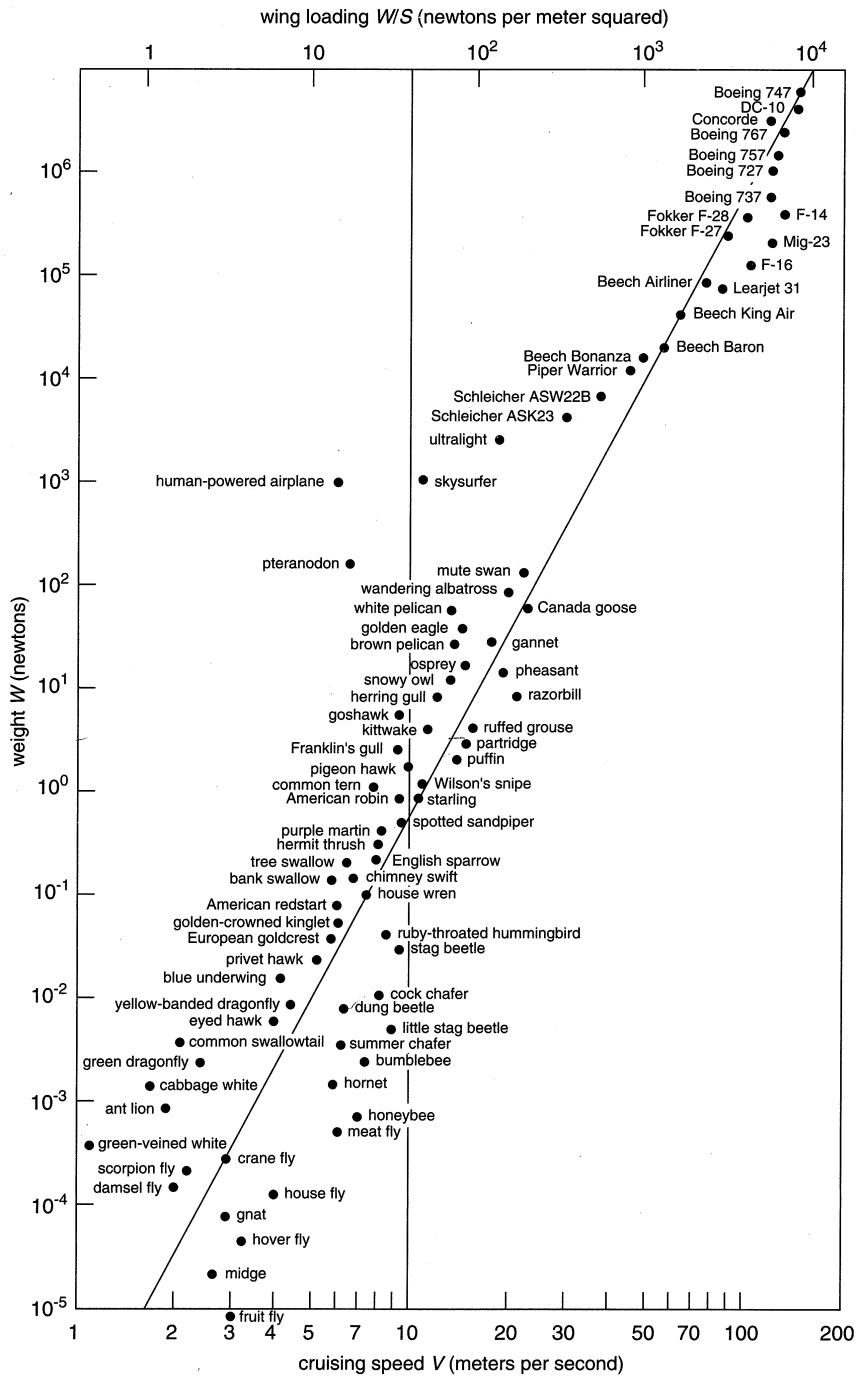

Figure II.1: The great flight diagram. Reprinted from Tennekes [1].

Tennekes also studied the relationship between the wing loading and the weight of birds with similar wing shape. We have these different scaling factors

$$\begin{aligned} W &\sim l^3 \\ S &\sim l^2 \\ \tfrac{W}{S} &\sim l \end{aligned} \tag{II.1}$$

Thus, the weight scales like the cube of the wing loading. This can be expressed as

$$\frac{W}{S} = c_1 W^{1/3} \tag{II.2}$$

Tennekes gathered experimental data to find the correlation factor. Figure II.2 shows a good correlation for birds with similar wing shape.

Other studies have also looked at the correlation between the wing area and the weight of birds [19, 35]. It has been shown that for herons, eagles, falcons, hawks and owls the following relation holds

$$S \sim W^{0.78} \tag{II.3}$$

Another interesting parameter for flappers is the wing beat frequency. The flapping frequency needs to be high enough to generate the lift and thrust needed without exceeding the maximal power that can be generated by the muscles. In addition, birds have physiological limitations to prevent bone fracture or muscle failure. Pennycuick [2] showed that the wing beat frequency depends on 5 parameters: body weight (mg), wing span (B), wing area (S), wing moment of inertia (I) and density (ρ),

$$f \sim m^\alpha g^\alpha B^\beta S^\gamma I^\delta \rho^\varepsilon \tag{II.4}$$

By using dimensional analysis, it is possible to find 3 equations

$$\begin{aligned} &\alpha + \delta + \varepsilon = 0 \\ &\alpha + \beta + 2\gamma + 2\delta - 3\varepsilon = 0 \\ &-2\alpha = -1 \end{aligned} \tag{II.5}$$

The remaining equations were found using a regression of the frequency vs. the mass, the span and the area of various birds from experimental data. Using the fact that the moment

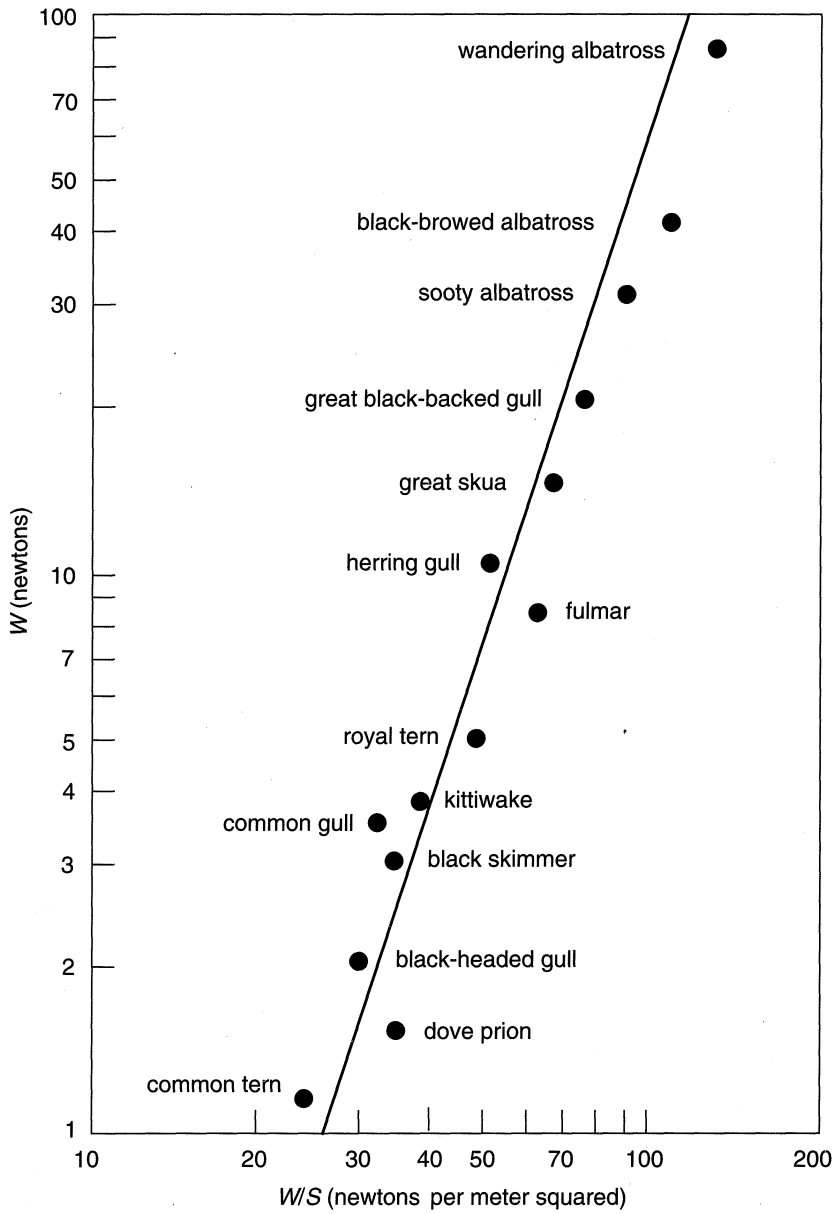

Figure II.2: The relation between weight and wing loading represented in a proportional diagram. When the weight increases by a factor of 100, the wing loading increases by a factor of 5 and the forward speed by a factor of more than 2. Reprinted from Tennekes [1].

of inertia can be linked to the other parameters ($I \sim mB^2$) Pennycuick concluded that the frequency may be estimated using the following relation

$$f \sim m^{1/3} g^{1/2} B^{-1} S^{-1/4} \rho^{-1/3} \tag{II.6}$$

To find the coefficient of proportionality in Equation II.6, he used a regression on experimental data (see Figure II.3) and concluded with a coefficient of correlation of 0.947, that

$$f = 1.08 m^{1/3} g^{1/2} B^{-1} S^{-1/4} \rho^{-1/3} \tag{II.7}$$

Pennycuick also studied the dependence of the wingbeat wavelength defined as

$$\lambda = \frac{V}{f} \tag{II.8}$$

He showed that the minimum power speed depends on the physical variables in the following way,

$$V \sim m^{1/2} g^{1/2} B^{-1} \rho^{-1/2} \tag{II.9}$$

Thus by using Equation II.6, we get

$$\lambda \sim m^{1/6} S^{1/4} \rho^{-1/6} \tag{II.10}$$

By proceeding the same way as before, he got a coefficient of proportionality of 0.817 (Figure II.4)

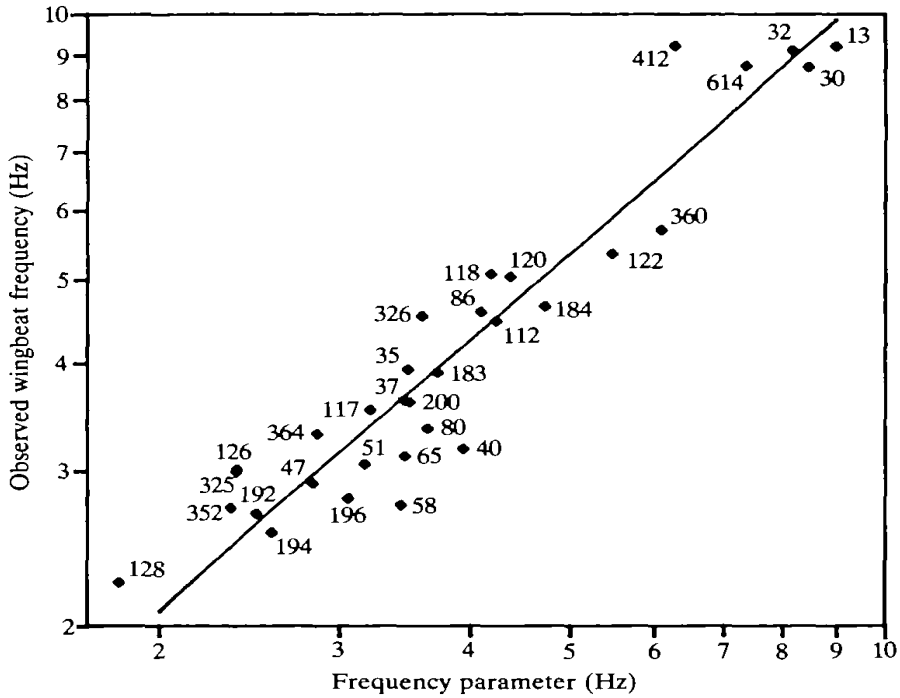

Figure II.3: Log-log plot of observed wingbeat frequency for various birds versus the frequency parameter. Reprinted from Pennycuick [2].

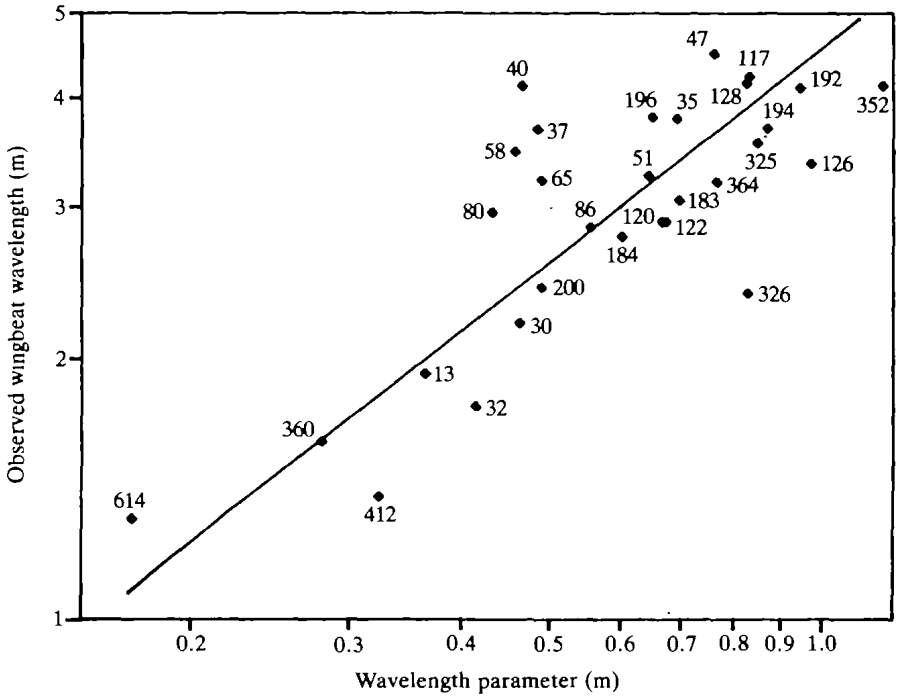

Figure II.4: Log-log plot of observed wingbeat wavelength for various birds versus the frequency parameter. Reprinted from Pennycuick [2].

The aspect ratio ($AR = \frac{B^2}{S}$) is an important parameter for airplanes and is also for flappers. Shyy et al. [17] discussed the influence of the aspect ratio for birds. Induced drag tends to increase when the aspect ratio decreases, thus large aspect ratios are found in species that spend most of their time gliding like the albatross and smaller aspect ratios are used by animals that need a high maneuverability.

II.2 Kinematics and aerodynamic forces production

Flapping flight is a complex problem and all its complexities have not been yet fully understood. In this section, an overview of the literature on lift and thrust production using flapping flight will be presented. A distinction between forward flapping flight and hovering flight will be made with an emphasis on the particularity of hovering flight. Flapping flight studies can be broadly separated into three groups: a biological literature that studies in vivo insects, birds and other flappers to better understand their mechanism of lift production; an experimental literature that builds models of flappers easier to study than in vivo animals, and finally a computational and theoretical literature that mathematically models flapping flight.

II.2.1 Biological study

a Forward flight case

In one of the earliest studies, Greenewalt [19] extensively looked at the relation between the wing span, wing area and mass among birds of various species. From experimental data he extracted a relation between the wing area and the wing loading.

Tucker [18] collected wind tunnel data (power requirements and morphological characteristics) on budgerigar and laughing gull. He compared his data to the theory developed by Pennycuick [2, 20] that predicts power requirements for avian flight. I will describe his theory in the computational section II.3. In his theory, Pennycuick expressed the total power

required to fly as functions of birds' morphology. Tucker was able to fit his measurements to the equation of power and deduce these parameters. He concluded that Pennycuick's theory gave good predictions for the power input for medium sized birds while it gave lower power values for small birds and higher values for large birds.

In addition with his theory, Pennycuick was able to get a first order estimate of the power consumption, the minimum power speed and some aerodynamic features of birds. For example, Pennycuick [20] found that pigeons have a minimum power speed of $8 - 9m.s^{-1}$, he was also able to study the influence of the flight speed on the kinematics of flapping. He observed that pigeons compensate for a decrease in the flight speed with an increase in stroke angle and frequency.

Azuma et al. [36, 37] studied extensively dragonflies. They first analyzed the flight kinematics of these insects. They used high speed cameras and painted the tip of the wings of dragonflies to visualize their wings beating. Afterward, they used the flight kinematics as input to their local circulation method coupled to a blade element theory. However, Azuma et al. failed to compare their results to known experimental results. They only noticed that the required power needed to fly fell within the usual range estimated by Weis-Fogh.

More recently with the advance of visualization and measurements techniques, Spedding et al. [21, 3] and Dickinson et al. [22, 4] have been able to study the dynamics of force generation during flapping flight by looking at the kinematics of the flight, the shape of the wake and its circulation. Spedding et al [21] and Rosen et al. [3], thanks to the advance of the digital particle image velocimetry, have intensively studied the force generation and wake pattern in thrush nightingale. Rosen observed that over the range of flight speed tested ($5 - 10m.s^{-1}$), the kinematics of the flight was similar. The wingbeat frequency and amplitude did not change. During the downstroke, the thrush nightingale has its wing fully extended. During the upstroke, however, the wing is sharply flexed. When the flight speed is increased, the thrush nightingale decreases the time spent in the downstroke. The downstroke ratio goes from values close to 0.5 at low speeds to 0.45 at high speeds. Rosen explained this by looking at the vorticity field in the wake. As seen in Figure II.5, for

low speed, the downstroke is characterized by a strong positive starting vortex while the vorticity released in the wake during the upstroke is weaker. The downstroke is the main contributor to the weight support. It also can be seen that the vorticity mainly lies on an horizontal plane, showing that the thrust generated is small; because at low speeds the viscous and induced drag are small. When the speed is increased, the bird needs to generate more thrust. The downstroke provides this increasing thrust component while the upstroke seems to have a more significant role in weight support. The wake vorticity strenght has a more continuous pattern and can be compared to an aerodynamically loaded wing that generates lift throughout its flight.

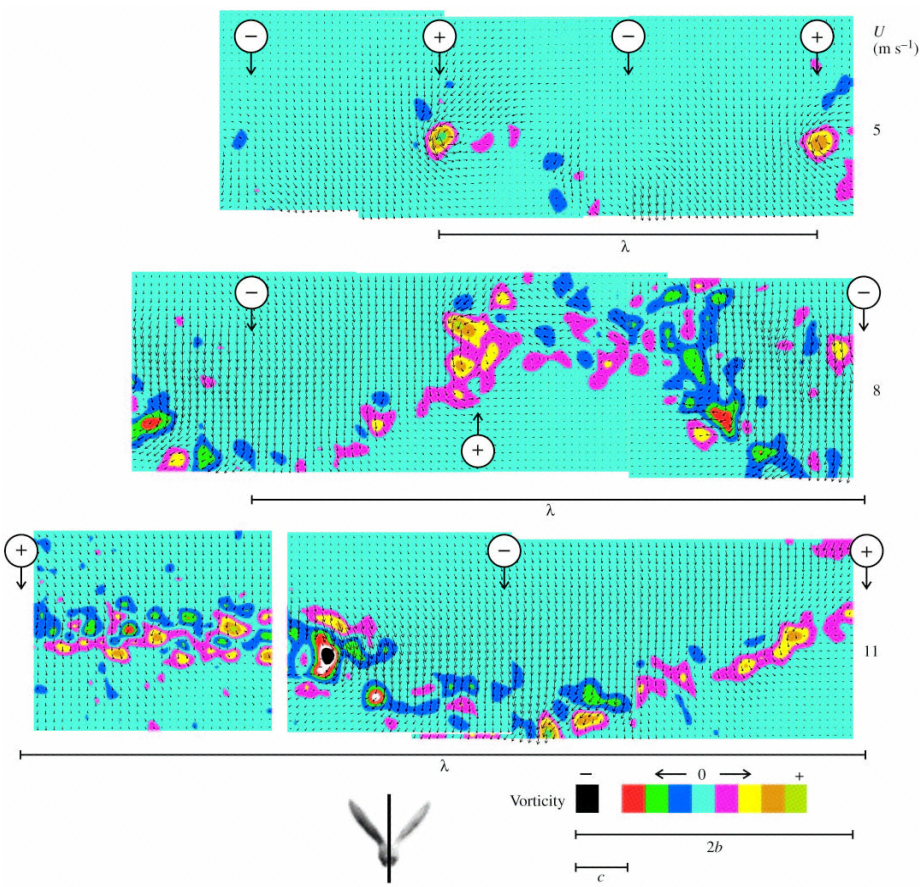

Figure II.5: Spanwise vorticity contour with superimposed velocity field for three flight speeds $(5, 8, 11 m.s^{-1})$. Reprinted from Rosen [3].

Dickinson et al. [4] described the wake pattern of the fruit fly and confirmed what Rosen described. They showed that during each stroke the fly sheds a vortex ring. This confirms the theory of Rayner (see Figure II.13). As predicted by Rayner, Dickinson observed an asymmetry in the force measurement. The aerodynamic forces are mainly produced during the downstroke and the upstroke has almost no vorticity. Dickinson explained the absence of vorticity during the upstroke by the Wagner effect and the "clap fling mechanism" presented by Weis-Fogh [32]. This mechanism is usually found in hovering birds. At the beginning of the downstroke, the two wings are very close to each other (Figure II.6 d1), thus the bound vorticity of one wing is the starting vortex of the other. This phenomenon decreases the lag due to shed vorticity in impulsively started wings (known as the Wagner effect). On the contrary, at the beginning of the upstroke (Figure II.6 vf) the wings are too far apart to exchange their vorticity. In addition, the wing reversal that happens at the end of the downstroke generates a starting vortex of the same sign as the one created during the upstroke, increasing even more the Wagner effect.

Wakeling et al. [38] also observed on dragonflies the lift enhancement due to the clap and fling by using high speed cameras.

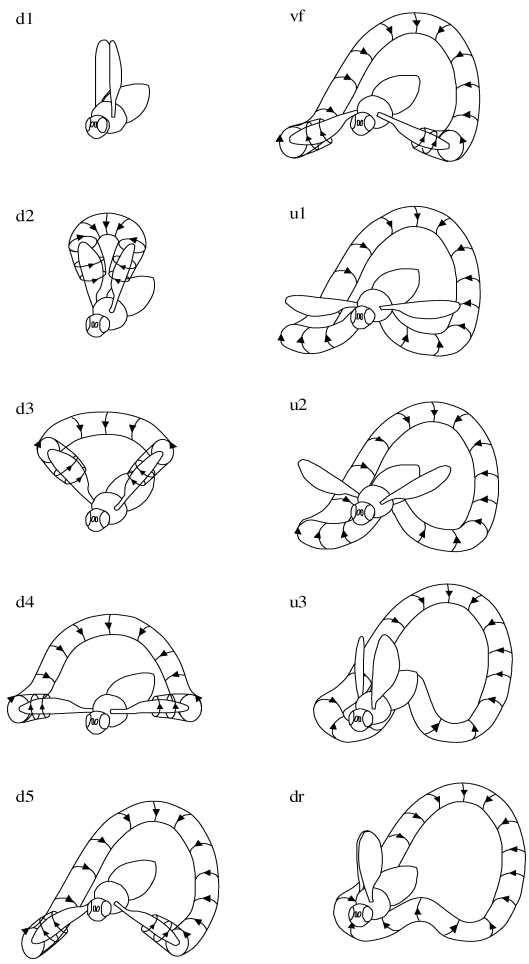

Figure II.6: Vortex loop formation by Drosophilia. Reprinted from Dickinson [4].

b Hovering case

Hovering is a flight regime where the freestream velocity is zero and the body is fixed in space. In hovering the main effect is the production of thrust to balance the weight of the flapper. Hovering is usually observed in small birds or insects.

In an early study, Pennycuick [20] noticed that the inclination of the flapping plane decreases (going from vertical to horizontal) as the forward velocity decreases. Especially in hover, the stroke plane is fully horizontal so that the thrust is aligned with the weight. In this configuration, birds generate a mean positive thrust to overcome their weight.

Later, Weis-Fogh [32] examined the kinematics of hover. He was the first one to observe three unusual phases: the clap, the fling and the flip. The clap happens when the wings

are brought together at the end of the upstroke. The wings closing in Figure II.7 C give an addition thrust by pushing out the fluid in the gap. At the beginning of the downstroke, the wings are rotated about their axis like an opened book (the fling). The flip happens at the beginning of the upstroke, the wings are rapidly rotated by almost 180°. These mechanisms seem to enhance the lift generation. When the wings start the downstroke right after the fling, two vortices of equal strength but opposite sign are created to satisfy the Helmholtz theorem (Figure II.7 E). Because the sign of these two vortices are opposite, the sum of their induced velocities on the wing is small and thus the Wagner effect is absent (see Figure II.8).

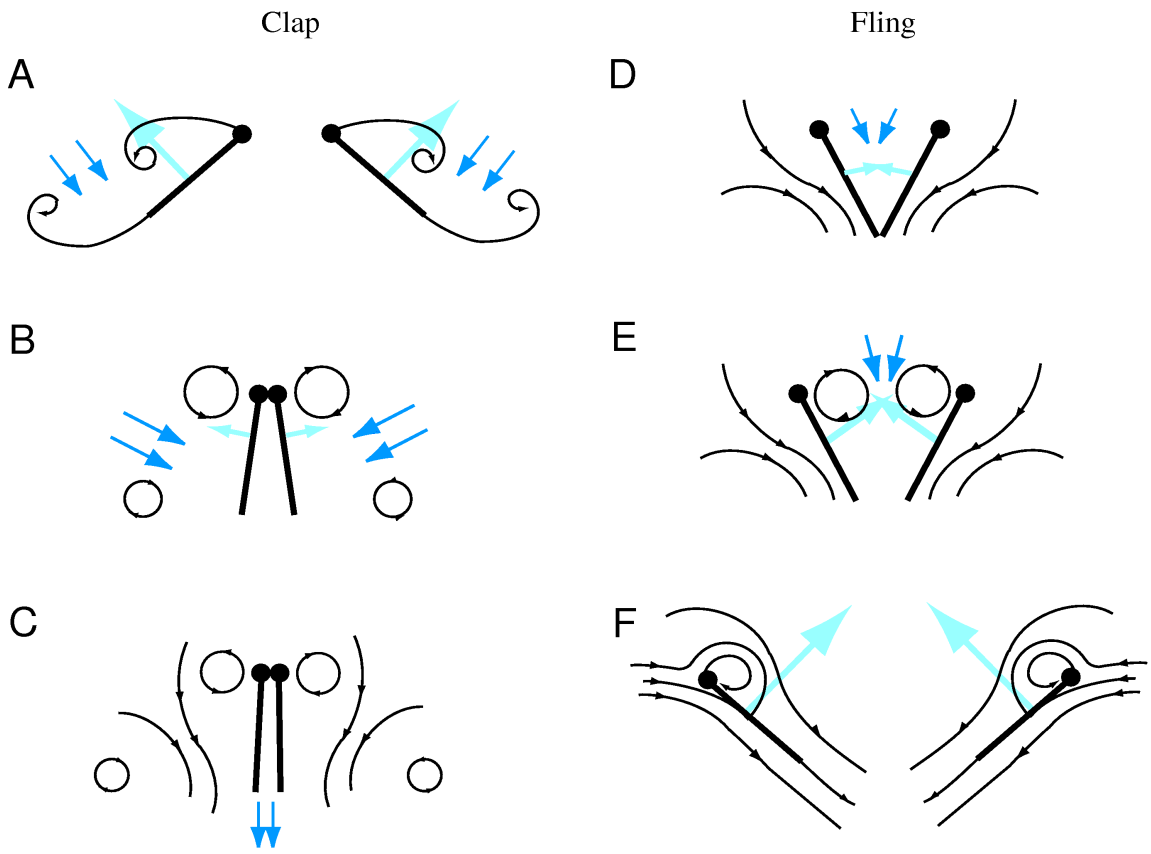

Figure II.7: Clap and Fling mechanism. Dark arrows show the induced velocities, the light arrows the net force and the dark lines are the flow lines. Reprinted from Sane [5].

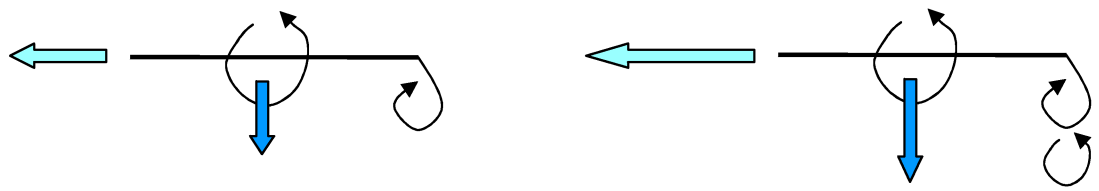

Figure II.8: Schema of thrust enhancement through the fling mechanism. The left drawing is an airfoil in upward plunging motion, the right drawing is an airfoil in upward plunging motion with the presence of the two vortices due to the fling. Dark arrows show the induced velocities, the light arrows the net force and the dark lines are the flow lines.

Wells [27] in 1993 studied the oxygen consumption of hovering hummingbirds to deduce the power required to perform hovering. He found that the mechanochemical efficiency for hummingbirds was about 9-11%. He also found that the inertial power requirements exceeded by a factor of 3 the aerodynamic power requirements which is in disagreement with the factor of 1 found by Weis-Fogh. Finally, Wells calculated that viscous power was smaller by a factor of 3.5 than the induced power. This result shows the importance of induced losses compared to viscous losses in hovering.

More recently in 2003-2005, a number of studies [25, 26, 28] have been conducted on hovering flight characteristics specifically. Altshuler and Dudley [25, 26] looked at the influence of the density on the kinematics of hummingbirds hovering. They concluded that hummingbirds compensate for a decrease in air density by increasing the flapping amplitude while the frequency remains unchanged. By augmenting the stroke angle, hummingbirds seem to take advantage of the clap and fling mechanism at the beginning of both the upstroke and downstroke. In another study, Chai [28] showed that hummingbirds were able to hover under large loading (once to twice their weight). These two results prove that hummingbirds have large power reserve enabling them to adapt to environmental modifications.

Finally, Betts [31] analyzed the influence of the wing shape on flight performance. He showed that butterflies with high aspect ratio wings were not able to hover or perform high speed maneuvers while smaller butterflies with lower aspect ratio wings under smaller wing loading were able to maneuver more easily.

II.2.2 Experimental study

Experimental studies can be categorized into two groups. The first one [6, 24, 39, 40, 41, 42, 43, 44] builds electromechanical models mimicking flappers to better measure the aerodynamic forces and power involved in flapping. The second one [9, 10, 44, 45, 46] looks at plunging and pitching airfoils or wings and studies the wake pattern as a function of the reduced frequency ($k = \frac{\varpi c}{2U}$) and the Strouhal number ($St = \frac{fh}{U}$), where h is the amplitude of the plunging motion, ϖ the angular frequency, f the frequency, U the freestream velocity and c the chord.

a Forward flight case

The second experimental group [6, 40, 41, 42] looks at plunging and pitching airfoils or wings and studies the wake pattern. Ol [46] studied the effect of the Reynolds number, Strouhal number and reduced frequency on a two degrees of freedom (pitching and plunging) wing in a water tunnel using dye. In the Reynolds number range (10,000-60,000), he showed that the Reynolds number effect on the near wake structure is small.

Jones [9] and Platzer and Jones [10] also used dye injection to visualize the vortices in the wake to compare them to the wake patterns provided by their two-dimensional potential code in plunging motion. They concluded that for a wide range of reduced frequencies, there was a good agreement between the experiment and their code. This agreement deteriorates for small plunge velocities when the viscous effects become more important. Also at high plunge velocities, flow separation occurs which is not captured in the potential code. To summarize, the wake pattern seems to mainly be governed by inviscid effects.

b Hovering case

Most of the electromechanical models are scaled models of the fruit fly [5, 40, 41, 42], the honeybee [24] or the hawkmoth [41]. They are mainly used in hovering simulations because of the difficulty of studying in vivo insects in hovering. The importance of the rotation that occurs at the transition from downstroke to upstroke (supination) and the role of the leading

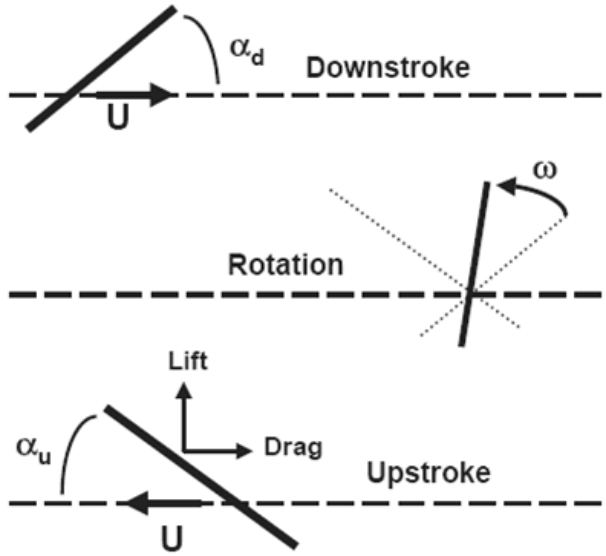

Figure II.9: Wing rotation mechanism. Reprinted from Dickinson [6].

edge vortex are studied with these models. Singh [39] and especially Dickinson [4, 36, 5, 39] and Ellington [41] have conducted these studies. The basic rotation mechanism is shown in Figure II.9. The wing translates at a constant pitch angle (α_d) and constant velocity (U) during the downstroke, at the end it rotates about an axis perpendicular to the chord at a constant angular velocity (ϖ) and then translates at a constant pitch angle (α_u) during the upstroke. With this mechanism, hovering insects always maintain a positive angle of attack.

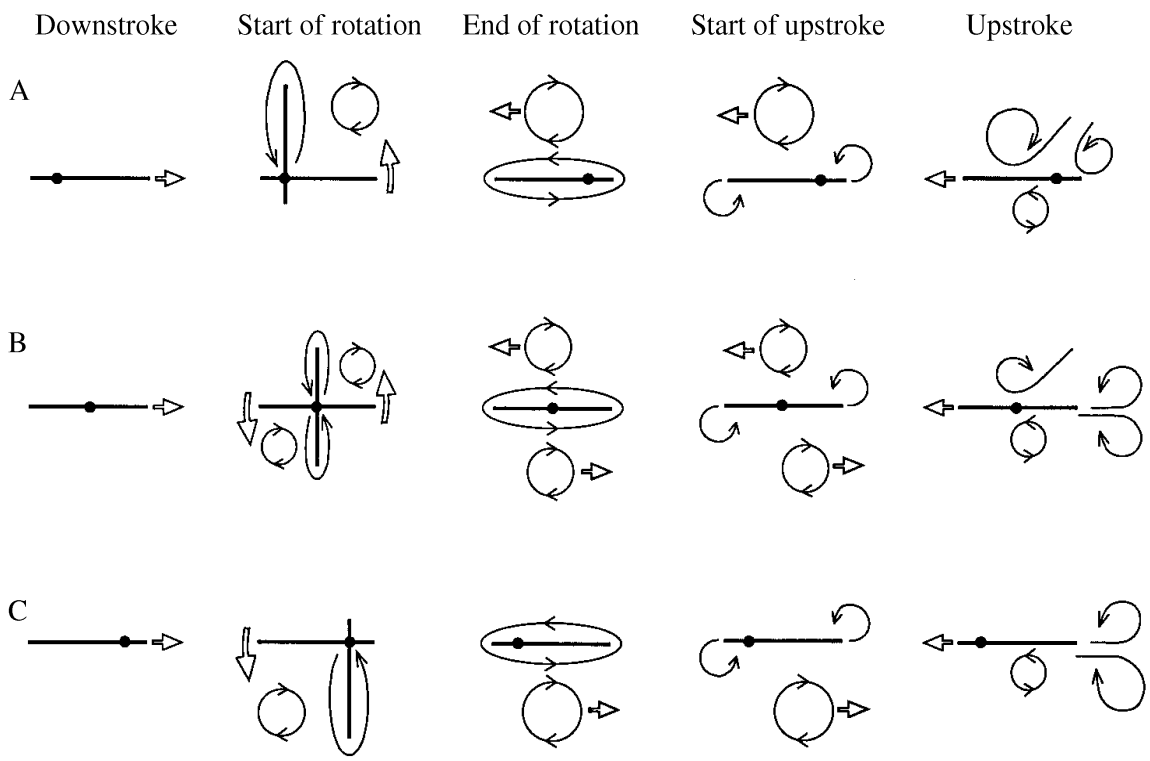

Figure II.10: Development of vorticity during a stroke reversal for an axis of rotation located respectively at 0.8, 0.5, 0.2 chord (A, B, C). Reprinted from Dickinson [6].

Dickinson showed the importance of the location of the rotation axis. For certain positions the mirror vortex shed during the supination enhanced the thrust generated during the upstroke (Figure II.10 A). As it can be seen in Figure II.10, in the case of rotation near the trailing edge, the mirror vortex created during supination is above the wing and moves in the direction of the subsequent translation. This vortex can be captured by the wing depending on the value of the rotational speed. When it is captured by the wing, it increases the thrust generated. When the rotation occurs at the center, two mirror vortices are created, one above and one below the wing. The strength of the above vortex is lower than in the previous case, thus when it is captured, the increase in thrust is smaller. In the rotation about the leading edge, the mirror vortex below the wing moves in the opposite direction as the wing and thus cannot be captured.

Lehmann [42] studied on a mechanical model of the fruit fly hovering the effect of the clap and fling. He concluded that this mechanism could enhance by a modest amount the

lift (from 1.4% to 17% depending on the heaving rate). However Lehman was not able to analyze the influence of the clap and fling on the output power. He hypothesizes that near pronation, the fling mechanism enhances the aerodynamic forces and since during this phase, the wing velocity is low, the profile power remains small (it varies in the wing velocity cube) and thus the efficiency is increased.

Ellington and his coworkers [41] discovered in 1996 the influence of the leading edge vortex (LEV) on hovering insects. In their work, they used Ellington's electromechanical scaled (10:1) model of a hawkmoth and released smoke from its leading edge. Ellington et al. observed that during the downstroke, the LEV remains attached until after the middle of the downstroke. After that, it breaks down on the tip of the wing (last 40-30% of the wing) and is shed into a big tip vortex. Finally the LEV is shed into the wake during the stroke reversal. By remaining attached during most of the half stroke, the aerodynamic forces are enhanced (dynamic stall).

II.2.3 Computational study

In this section, a review of the computational methods used for flapping airfoils or wings will be presented. We can find three main methods. First, the analytical solutions; they have a limited range of application (two-dimensional and small amplitudes) and are based on the Theodorsen function. Second, the potential method can be two or three-dimensional. Their limitation is that they do not capture the viscous effects; this is particularly important at low Reynolds number for slow motion. Finally, the full unsteady Navier-Stokes equations can be solved. Their main drawback is the extensive computing power required to generate converged solutions.

a Analytical methods

These methods are based on the work done by Theodorsen for two-dimensional flows and on the lifting line theory for three-dimensional flows. The two-dimensional methods are limited to thin airfoils undergoing small amplitude motions in a potential flow. Their

applications are limited to high Reynolds number flows, thin airfoils and forward flight. Nevertheless, these are powerful methods because they give analytical solutions for the aerodynamic forces and power.

Azuma et al. [47] developed an analytical method for deflected thin airfoils undergoing heaving, surging and feathering motions. He could thus find the unsteady aerodynamic forces and power for various reduced frequencies.

Wu [48] also used the linear potential theory to find the forces on moving two-dimensional flexible plate. He computed the forces on a waving plate with variable forward velocity.

Finally in three-dimensions, Ahmadi et al. [49] looked at the small amplitude plunging and pitching motion of a three-dimensional unswept wing. Their results are based on the unsteady lifting line theory. This theory assumes an unswept high aspect ratio wing oscillating at low reduced frequencies. Ahmadi et al. were able to find the optimum motion (amplitude of plunging, amplitude of pitching, phase shift and pitch axis) that minimizes the input power for a prescribed thrust for a high aspect ratio wing ($AR = 8, 16$) undergoing pitching and plunging motions at low reduced frequency ($k \leq 1$).

b Potential methods

Analytical methods have many limitations since they are based on small amplitudes. We are especially interested in large amplitude flapping for hovering and thus cannot use linearized equations anymore. Potential methods assume an inviscid, incompressible and irrotational (except in the wake) flow. These methods usually use a vortex-lattice type of technique.

b.1 Forward flight case

In two-dimensional flows, Basu et al. [50] and Jones et al. [9, 10, 45] used the same method. The airfoil is divided into panels of source and vorticity distribution. The vorticity in the wake is modeled using point vortices. The unknown vorticity and source distributions are solved using the flow tangency condition on the airfoil. The strength of the vorticity

shed in the wake is found using a Kutta condition. This method will be described more in details in section IV.2. Jones et al. [9] showed a good agreement between the wake structures of an experimental airfoil plunging and the results provided by their potential code for moderate Reynolds numbers. This shows that wake patterns are mainly governed by inviscid effects; this becomes false when the amplitude and frequency of motion becomes too low, then viscous effects become important. In addition, to model the viscous effects, Jones [45] improved his potential code by coupling it to a boundary layer algorithm. This boundary layer algorithm was valid for Strouhal number of 1 or less where separation does not occur. Jones compared the thrust predicted by his inviscid code to the thrust of his code coupled to the boundary layer algorithm. However, he was not able to run the viscous code at high frequency ($k \succ 1.5$) or large angle of attack. He showed that the curve of thrust versus reduced frequency was shifted by a constant value compared to the inviscid curve. Jones thought that this linear shift could be extrapolated to higher values of reduced frequency where the boundary algorithm could not converge. A limitation of the boundary layer method is its inability to model separated flows.

For three-dimensional flows, the methods presented above can be extended. These methods can be classified into two groups.

The first one assumes a frozen wake [33, 34, 51]. The wake is convected at the freestream velocity or the velocity predicted by the actuator disk theory in the case of Hall's method in hover [33, 34]. The method developed by Hall et al. will be explained in greater details in section III.2. The main limitation of these methods is that they neglect the roll-up of the wake. This is a valid approximation for lightly loaded wings, when the induced velocity of the wake can be neglected compared to the freestream velocity but it becomes especially wrong in hovering.

The second group uses a self convected wake [11, 12, 48, 49, 50, 51]. These methods agree well with the small amplitude theory. Willis et al. [11] compared the lift coefficient obtained with their code for an impulsively started wing with various aspect ratios to the results of Katz and Plotkin [12]. They found a really good agreement. In addition, they

observed the wake roll up at the tip for finite wings. These methods will be explained in greater details in section V.2.

b.2 Hovering case

In potential methods, it is possible to approximate the convection speed of the wake by the convection speed provided by the actuator disk theory. Thus, as we will present in Chapter III, the convection speed in hovering in Hall et al. [33, 34] will be replaced by the freestream predicted by the actuator disk theory. This method is limited to lightly loaded wings because the roll-up of the wake is neglected compared to the freestream velocity. Thus, in our case of interest where the flapping amplitude and frequency are large, the wing is not lightly loaded and we cannot neglect the roll-up of the wing.

c Full Navier-Stokes methods

The full Navier-Stokes methods are an improvement compared to the potential methods, since they incorporate the viscosity.

We can divide the unsteady Navier-Stokes methods in two categories: Lagrangian and Eulerian. The Lagrangian methods [7, 11, 12, 50, 51, 52, 53, 54, 55, 56, 57, 58, 59, 60, 61] are particle based; while the Eurlerian methods [8, 40, 62, 63, 64, 65, 66, 67] use moving grids. Lagrangian methods have many advantages over grid based methods when modeling flapping flight. Only the portion of the flow where vorticity exists needs to be described. Vortex methods are grid free; thus they can model complex moving geometry. In addition, they model infinite domains compared to Eulerian methods that need a grid of finite size. However to the best of my knowledge, particle methods have not been used in hovering yet, while nothing prevents them from being used in that case.

c.1 Forward flight case

The viscous vortex methods are an extension of the potential based vortex methods described in the previous section b. The vorticity field is modeled using discrete regularized vortex blobs. Winckelmans and Leonard [52] presented several different regularization func-

tions. Regularized functions are used to remove the singularity arising when the radius goes to zero. They modeled each blob by a volume of vorticity having a certain distribution. For example a typical function used is

$$\frac{1}{4\pi\sigma^3}\frac{15/2}{\left(\left(\frac{x}{\sigma}\right)^2+1\right)^{7/2}} \tag{II.11}$$

where x is the radial distance from the center of the blob and σ a cut-off radius.

In addition to the convection step already present in inviscid particle methods (convection of the particles with the velocity field and their strengths with the velocity gradient field), there is a diffusion step due to the viscosity. Different methods exist to model the convection term. The easiest but most expansive computationally is the direct integration of the vorticity to get the velocity field in the domain. This is the method used in most of the potential vortex methods [11, 12, 48, 49, 50, 51]. A second method is called the Vortex in Cell method (VIC) [53]. In this method, an intermediate grid is generated, the vorticity is extrapolated on this grid and the velocity is computed using a finite difference scheme. This method is only used in viscous particle methods because the intermediate grid is also sometimes used to compute the diffusion term using an Eulerian method.

Koumoutsakos et al. [54] were the first to present a method on how to treat viscous boundaries in two-dimensions. This method was then improved by Ploumhans et al. [55, 56] and can be described with the following steps:

- The local velocity is computed to convect the particles.
- Their strength is updated to account for the stretching (inviscid term due to the gradient of the velocity field) and the diffusion (viscous term). The diffusion is done by using the Particle strength exchange (PSE) scheme first developed by Degond and Mas-Gallic [57].
- A sheet of vorticity is created on the boundaries to ensure the no-slip. boundary condition

In the PSE method, the diffusion operator (Laplace operator) is transformed to an integral operator which is then discretized over the particles using a summation operator.

Eldredge [58] used for two-dimensional flapping wings the method described above. He was able to perform a direct numerical simulation of a typical stroke at low Reynolds number (550). Even though the particle method seems well suited for flapping flight, the three-dimensional problem has not been solved yet using these methods, nor the hovering problem. Ploumhans et al. [55, 56] and Cottet [53, 59] have used vortex methods for flows around sphere at low Reynolds number, proving that the method works in three-dimensions.

Eulerian methods seem less well suited than Lagrangian methods in the case of flapping wings. However, grid based solver have been more studied and now powerful CFD packages are available. I will first present a review of the two-dimensional methods.

Hamdani et al. [7] conducted an interesting study on the importance of the Reynolds number effect on highly accelerated flows. An horizontal airfoil is accelerated under a pitching motion to an angle of attack of 90 degres. Hamdani defined a non-dimensional pitching rate

$$\Omega^+ = \frac{\dot{\alpha} c}{U} \tag{II.12}$$

where, $\dot{\alpha}$ is the pitching rate, c the chord and U the freestream.

Figure II.11 shows that for small Reynolds number, the forces and moment coefficients are only a little lower than in the high Reynolds number flow. The agreement is especially good for small angles of attack where the leading edge vortex is small. This shows that the aerodynamic forces mainly come from the large acceleration of the airfoil and not from the viscous forces.

In low Reynolds number flows, a big leading edge vortex can be observed. Wang [60], Akhtar et al. [61] and Kurtulus et al. [68] described the vortical properties of a flapping airfoil. Kurtulus used a typical flapping motion (constant translation and quick rotation at the end of the up and downstroke). A trailing edge vortex is shed and grows during the translational movement; at the same time a leading edge vortex is observed too. At the end of the translation, the airfoil starts its rotation, the leading edge vortex is now shed and a

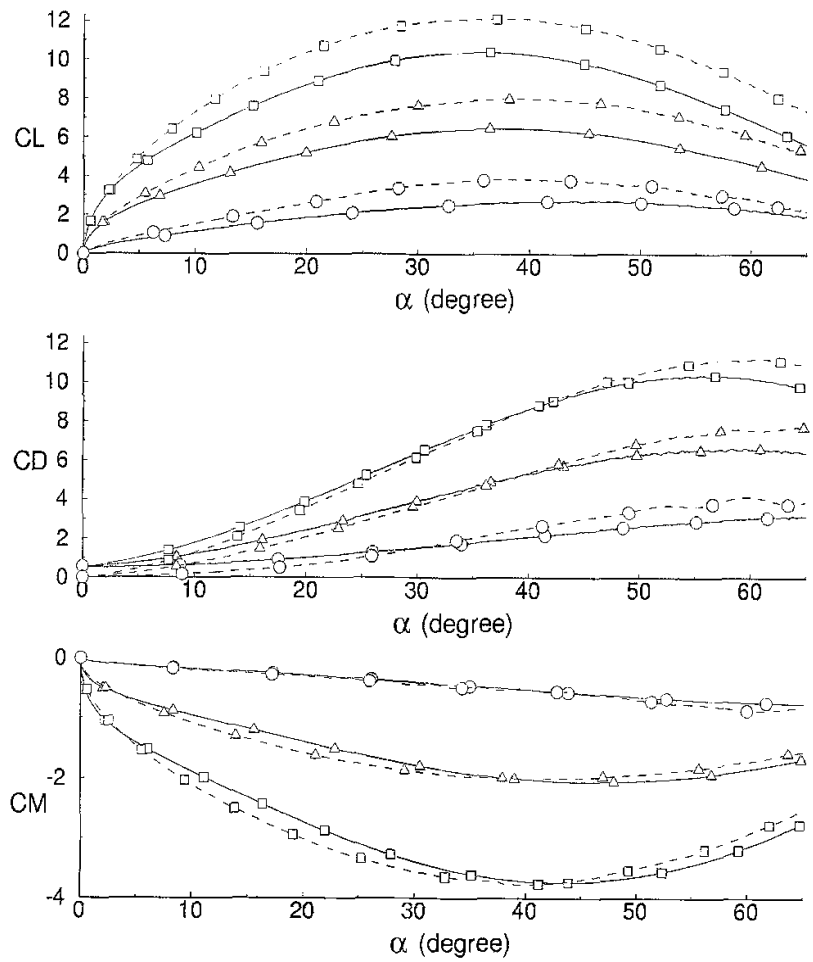

Figure II.11: Force and moment coefficients versus α. The airfoil is pitching in freestream. Pitching rates (Ω^+) of 2.4, 1.6 and 0.5 are shown as squares, triangles and circles, respectively. Results for $Re = 100$ and $Re = 100000$ are shown as solid and dashed lines, respectively. Reprinted from Hamdani [7].

trailing edge vortex is created and shed into the fluid. This process is similar to what was described in sections II.2.1 and II.2.2.

c.2 Hovering case

Three-dimensional grid based methods [13, 30, 69, 70, 71] have only been developed in the past few years because they require a lot of computing power. Mao et al. [30] used a three-dimensional unsteady laminar Navier-Stokes method to study the hovering flight of 8 insects with Reynolds numbers ranging from 75 to 3850. Their method was tested against simple flows over a flat plate. It was also tested on a fruit fly model and aerodynamic

forces computed agreed well with the predicted forces. The CFD results confirmed the mechanism of thrust generation evocated earlier. The thrust is mainly created (80%) during the translational up and downstroke. In addition the thrust coefficient is really high proving that insects take advantage of the dynamic stall. The CFD results also showed that the leading edge vortex is not shed during the translational movement but during the rotational movement. This delayed stall could be explained by a spanwise flow from wing base to wing tip preventing the leading edge vortex from detaching. This mechanism of high thrust production was observed on every insects tested.

These results were also observed in the simulations done by Liu et al. [70]. However, the thrust found in their hawkmoth study was 40% higher than the weight of the insect.

Recent simulations of Zuo et al. [69] also explained the mechanisms of thrust production and the presence of an axial flow from root to tip. This axial flow could be due to the fact that the wing velocity varies largely during the up and downstroke and also varies along the span. The flow convects vorticity toward the wing tip which is shed into the vortex tip; thus preventing the leading edge vortex of developing too much and breaking down.

II.3 Power requirements

Avian flight remains a challenging problem to master. In the previous section, we saw how the aerodynamic forces were generated. In this section, an emphasis will be put on the power needed by birds to perform their flapping flight. Birds need power to produce lift and overcome drag. A better understanding of the well known U-shape power curve (power versus flight speed) could give more insight to the decisions birds make in flight.

The total power (P_{tot}) is the sum of the induced power (P_{ind}), profile power to overcome the viscous forces of the lifting bodies (P_{pro}), the parasite power to overcome the viscous forces on the non lifting bodies (P_{par}) and the inertial power needed to move the wings (P_{iner}). The total power is also equal to the metabolic power (P_{meta}), which is the output

power of the bird,

$$P_{tot} = P_{meta} = P_{ind} + P_{pro} + P_{par} + P_{iner} \tag{II.13}$$

The total power has been measured in some experimental studies. Wells [27] studied the hovering flight of hummingbirds. He measured their oxygen consumption and deducted the energy needed to hover. He concluded that hummingbirds' muscles were operating at an efficiency of 9-11%.

The first three terms in Equation II.13 define the aerodynamic power (P_{aero}). Different models have been developed to try to compute this power. Tucker [18], Greenewalt [19] and Pennycuick [2, 20] studied similar models. They are based on the lifting line theory of Prandtl and are fitted to measurements of metabolic power obtained in wind tunnel tests. A first limitation to these methods is the underlying assumption that the wing is fixed and thus that the wake lies in a plane behind the wing. Rayner [8, 62] has extended the lifting line theory to unsteady wing movements by using free vortices in the wake. The wake is now shed from the trailing edge of the wing. Hall et al. [33, 34] also developed a vortex method based on the Minimum Induced Loss Propeller theory. This theory assumes that the forces (thrust, side force and lift) are a consequence of the change of the momentum in the wake. This method will be more developed in section III.2

More complex two and three-dimensional potential codes using vortex methods are required to better understand the wake evolution especially for large reduced frequency and Strouhal number [11, 63, 64, 65, 66].

Finally to fully capture the viscous effects and the leading edge votex, Navier Stokes solvers are needed [8, 11, 40, 62, 63, 64, 65, 66, 67]. A more complete review of the last two methods was presented in section b and c.

An overview of the lifting line theory will be presented next. The lift and drag can be defined as

$$\begin{aligned} L &= \tfrac{1}{2}\rho S V^2 C_L \\ D &= \tfrac{1}{2}\rho S V^2 C_D \end{aligned} \tag{II.14}$$

The coefficient of drag (C_D) can be divided into two parts,

$$C_D = C_{Di} + C_{D0} \tag{II.15}$$

C_{Di} represents the induced drag due to the energy deposited in the wake and C_{D0} is the friction drag coefficient and both includes the losses on the lifting and non lifting bodies. In steady state, the friction coefficient is usually constant and Prandtl showed that the induced drag was proportional to the square of the circulation. Thus, the drag can be expressed as

$$D = \frac{L^2}{2\pi\varepsilon\rho B^2 V^2} + \frac{1}{2}\rho S V^2 C_{D0} \tag{II.16}$$

ε is a coefficient of proportionality. In steady flight the lift is equal to the weight. From Equation II.16, we can derive the aerodynamic power as,

$$P = DV = \frac{(mg)^2}{2\pi\varepsilon\rho B^2 V} + \frac{1}{2}\rho S V^3 C_{D0} \tag{II.17}$$

Equation II.17 is the equation of the power curve shown in Figure II.12.

The curve in Figure II.12 has a characteristic U-shape. At low speed, the induced losses dominate, a lot of energy is deposited in the wake to provide sufficient lift to overcome the weight; while at high speed the viscous losses become more important. This explains why hovering is usually found in small birds or insects. We can see that for a speed of V_{mp}, the power is minimum and for a speed of V_{mc}, the cost of transport ($C = \frac{P}{mgV}$)is minimum.

To estimate the lift and drag, during the early 20th century, the blade elements theory has been developed. It assumes a constant C_L and C_D over a flapping cycle and uses a polar equation over sections of the wing. This method neglects the fact that flapping is a fully unsteady process, especially in hovering and also neglects the three-dimensional effects especially important for low aspect ratio wings.

Tucker [18], Greenewalt [19] and Pennycuick [2, 20] proposed models derived from the lifting line theory and fitted to experimental data obtained in wind tunnels. Weis-Fogh [32] also used quasi-steady aerodynamics to evaluate the performance of hovering animals.

The problem of the lifting line theory is that it cannot be applied to hovering. To model hovering, the actuator disk theory has been used. This theory is explained in Appendix

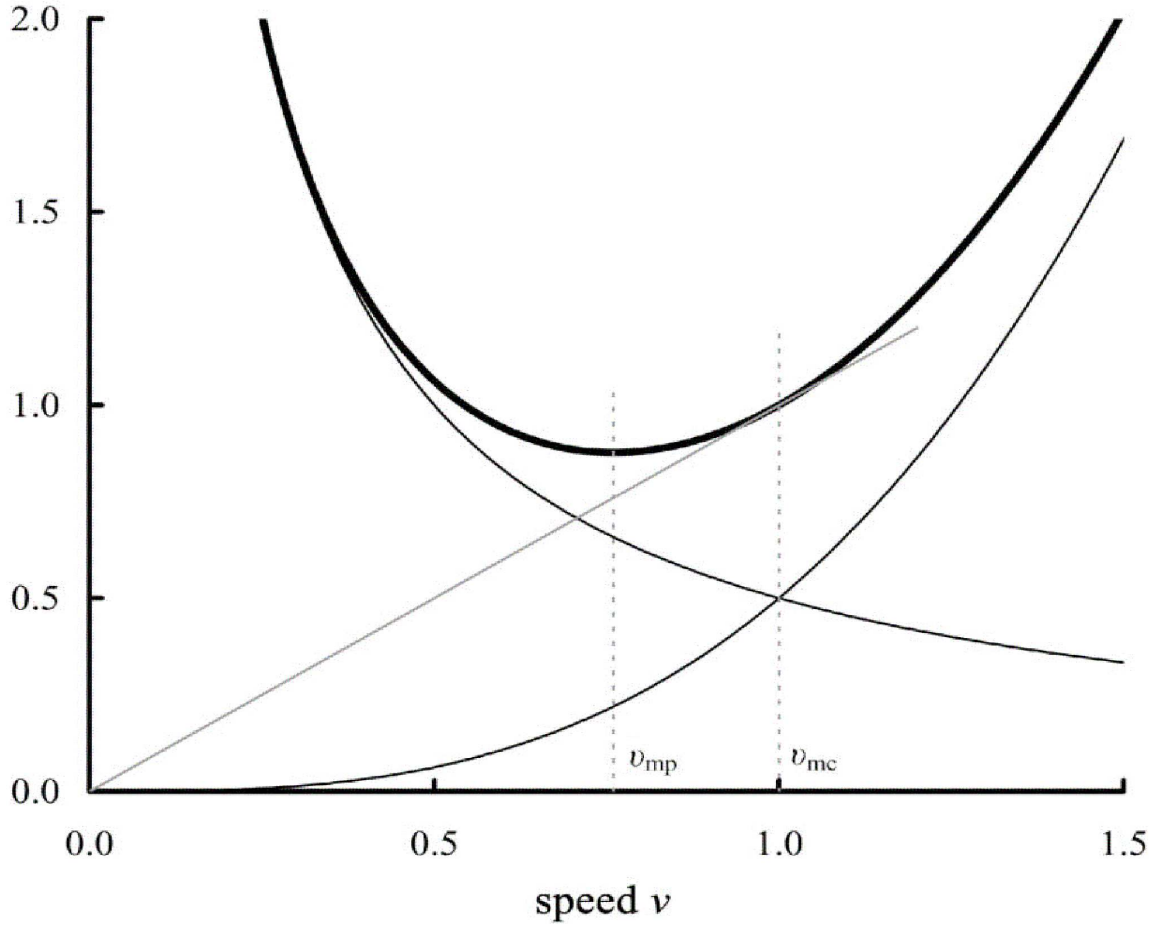

Figure II.12: The idealized lifting line power curve. Reprinted from Rayner [8].

A.2. The induced power becomes

$$P_{ind,hov} = \sqrt{\frac{(mg)^3}{\frac{1}{2}\pi\rho B^2\varepsilon}} \tag{II.18}$$

where ε is an efficiency factor to take into account tip losses.

Stepniewski [63] introduced a smooth transition between the lifting line theory and the actuator disk theory.

Wakeling et al. [64] performed a mean lift coefficient quasi-steady analysis. They gathered lift and drag data of dragonflies along with kinematics data of their flight. Using these data they were able to compute the induced power, viscous losses using a viscous drag profile and the inertial power. They concluded that the dragonfly had an efficiency of 13% by measuring heat produced by the dragonfly body.

Rayner [8, 62] developed a model based on free vortices in the wake rather than on bound vorticity on the wing. He assumed a periodicity of the wing motion. Thus to the first order (neglecting wake roll up), he models the circulation as the sum of a constant term and a sinusoidal term,

$$\Gamma = \Gamma_0 + \Gamma_1 \sin(2\pi f t + \varphi) \tag{II.19}$$

Rayner also presented a variety of wake patterns that derive from Equation II.19. These wake geometries are presented in Figure II.13. He mentioned that only wake geometries (d) and (e) have been observed in birds. (e) is characteristic of slow forward flapping flights.

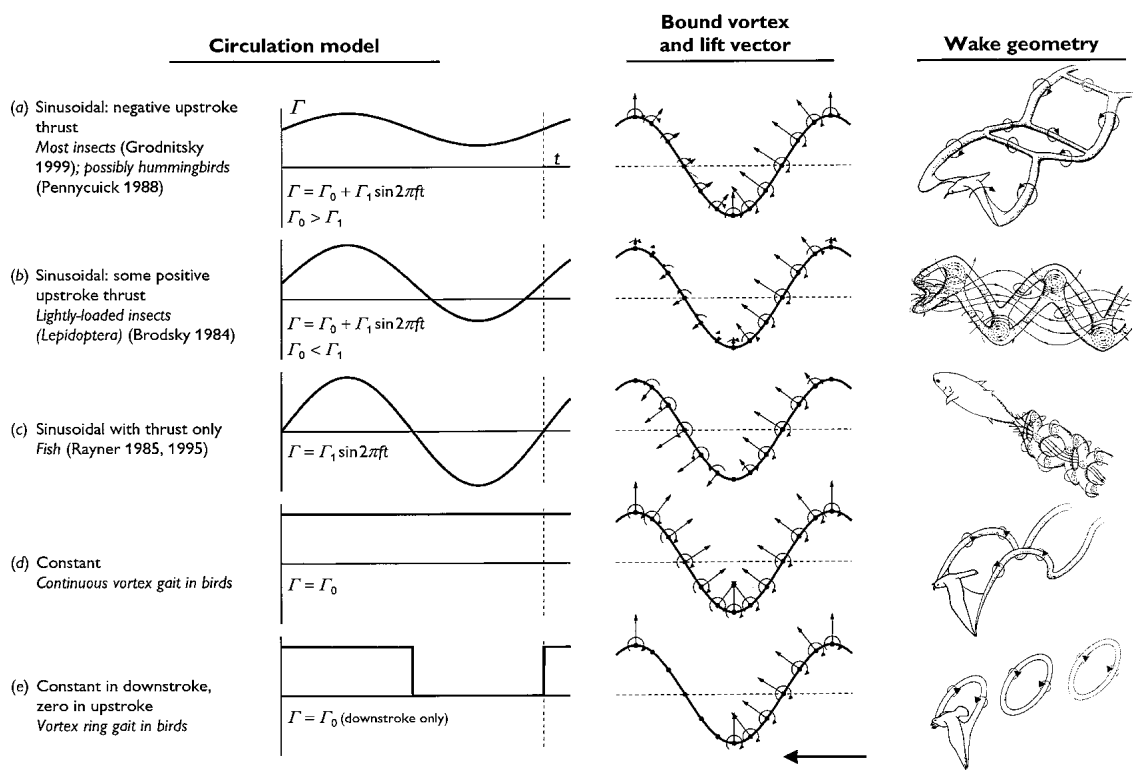

Figure II.13: Wake geometry and lift, thrust production as a function of the circulation model. Reprinted from Rayner [8].

Rayner concluded that empirical results showed that the circulation was a piecewise function (model e) and thus could be modeled by free vortex rings. The wake is prescribed by the wing motion. He derived an expression for the power as a function of the wingbeat

frequency, the wingbeat angle and some experimental parameters function of the wake shape,

$$P = \frac{(mg)^2}{2\pi\varepsilon\rho B^2 V} \frac{4\kappa}{\left[J_0(\phi) + \cos(\phi)\right]^2} + \frac{1}{2}\rho S V^3 \left[C_{Dpar} + C_{Dpro}(f, V, \phi)\right] \tag{II.20}$$

As it can be seen on Equation II.20, the form of the aerodynamic power is similar to the one derived with the lifting line theory. However it differs in two points. First, it separates the drag due to non lifting bodies and lifting bodies; second, it adds the influence of the wingbeat frequency and amplitude.

Now that methods to estimate the aerodynamic power were introduced, we need to estimate the inertial power (P_{iner}). The inertial power is linked to the moment of inertia of the bird. It can be calculated using strip theory. Van Den Berg et al. [65] computed the moment of inertia using the strip theory on 29 bird species. The wing is divided into n strips and the moment of inertia is then calculated as,

$$I = \sum_{i=1}^{n} \left(m_i d_i^2 + \frac{m_i}{12} w^2 \right) \tag{II.21}$$

where, m_i is the mass of strip i, d_i the distance between the center of the strip and the shoulder joint, w the width of the strips. It is now possible to derive the kinetic energy associated to the wing rotation,

$$E_{kin} = \frac{1}{2} I \varpi^2 \tag{II.22}$$

For purely sinusoidal flappers, we have

$$\varpi = \pi\phi f \sin(2\pi f t) \tag{II.23}$$

Thus, the inertial power for two wings is

$$P_{iner} = 4\pi^2 \phi^2 f^3 I \tag{II.24}$$

We can take a closer look at hovering flight. First, the parasite power due to the body is zero since the flight velocity is 0.

Norberg et al. [29] have applied Rayner's theory to the hovering flight of the bat. They showed that in hovering, the inertial power is 55% of the total power; while in slow forward

flight ($4.2m.s^{-1}$), it contributes to 22% of the total power. This study shows the importance of the inertial power in hovering flight. This was confirmed by Wells [27] who showed that for hovering hummingbirds, the inertial power was three times the aerodynamic power.

As a conclusion, we saw that flapping flight is a complex problem, it involves a full three-dimensional unsteady flow. In vivo experiments are hard to do because of the size of the insects studied and the fact that usually when insects are placed in wind tunnels, their stress factor adds a lot of noise to the experimental data. The computational field has made a lot of progress. Full Navier-Stokes simulations are now possible. However they take a lot of time and usually require parallel computing. It seems that the free vortex methods are the best suited to the hovering problem. Nevertheless, the majority of the methods developed to study hovering flapping flight are quasi-steady methods or Eulerian unsteady Navier-Stokes methods. It seems that there is a lack of computationnaly efficient methods to model hovering flight. Potential methods also have the advantage of being adaptable. In other words, a free vortex potential method can be developed, then it can be improved to include the effect of viscosity. Some speeding techniques exist for potential codes (p-FFT tree codes [11]) that can be added to the core program too.

Chapter III

A Wake Approach to the Constrained Optimization Problem

In this chapter, we consider the problem of optimal aerodynamic performance of a flapping mechanism in hover or in forward flight.

III.1 Problem description

The objective is to find the optimal circulation in the wake and cross-sectional chord distribution along a flapping wing that minimize the power requirement for a given lift and thrust. In addition, two flight parameters also need to be optimized; the stroke angle which represents the angle between the end of the downstroke and the end of the upstroke, ϕ and the flapping frequency, f. In section III.2, we describe a method that finds the optimal circulation in the wake.

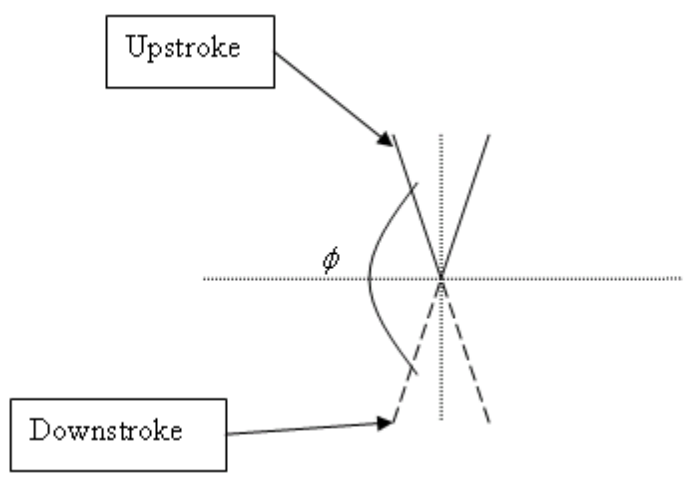

Figure III.1: Rear view of the wings. The solid lines represent the position of the wing at the end of the upstroke and the dashed line at the end of the downstroke.

III.2 Approach

Hall et al. [33] developed a method to find the circulation distribution along the span of a flapping wing that minimizes the power required to generate a given thrust and lift. Their approach is based on the Minimum Induced Loss Propeller theory. This theory assumes that the forces (thrust, side force and lift) are a consequence of the change of the momentum in the wake. Induced power loss arises from the deposition of kinetic energy in the wake. Consequently, the forces and power loss depend on the structure of the wake independently of how this one was generated. The theory also assumes that the wing is lightly loaded, in other words, the induced velocities are small compared to the forward flight speed.

However this method was developed in the context of high Reynolds numbers. In this case, the coefficient of drag C_d is nearly independent of the Reynolds number. In this study, we are interested in low Reynolds number flows. When the Reynolds number $Re_c = \rho V c/\mu$ is small, viscous effects become Reynolds number dependant and tend to scale like $1/\sqrt{Re_c}$. In other words, the drag is now a function of the chord, which is therefore a parameter we want to optimize.

The direct approach would be to derive the total required power (induced and viscous) and to optimize it as a function of the chord and the circulation distribution which is also a function of the chord. This is a non-linear constrained optimization problem. The constraints are of two types; equality constraints for the required forces (lift, thrust, and side force) and inequality constraints for the maximum chord and coefficient of lift allowed.

A first approach would be to find the optimized circulation solution to the constrained inviscid problem. Once the circulation distribution is found, we can use it as an input in the full viscous problem. The circulation is now known and we solve for the optimized chord. This will be the method used, which is of course quite not optimal. The rigorous way would be to solve for the circulation and chord the full viscous problem directly. Nevertheless, for lightly loaded wings, experiments show that the inviscid and viscous circulations are very similar [34].

III.2.1 Minimizing the induced power

First we will derive the expression of the forces and induced power loss and minimize it. This section is largely based on Hall et al. [33, 34] and the derivation closely follow their work.

The flow is assumed to be inviscid, incompressible and irrotational (except for the vorticity in the wake). Consequently, the flow is governed by the three-dimensional Laplace's equation,

$$\nabla^2 \varphi = 0 \tag{III.1}$$

We are using a Cartesian coordinates system (x, y, z) with the three cartesian coordiantes taken in the flight direction, spanwise direction, and vertical direction, respectively.

In addition, we assume that the wing is lightly loaded; the velocities induced by the wake are small compared to the wing speed. In other words, the velocities in the wake do not significantly deform the wake. We can then assume a rigid periodic wake. This assumption is of course not true, the wake rolls up; however in the lightly loaded case this roll-up can be neglected.

As mentioned earlier, the force averaged over one flapping period is equal to the opposite of the change in momentum in the wake. The linear momentum in the wake over one period $T = \frac{1}{f}$ is given by:

$$\vec{\xi} = \rho \int \int \int_V \vec{\nabla} \varphi dV \tag{III.2}$$

where V is the volume that encloses one period of the far wake (Figure III.2). By applying Gauss' theorem to Equation III.2, we can express the momentum in terms of a surface integral, i.e.,

$$\vec{\xi} = -\rho \int \int_A \varphi \vec{n} dA \tag{III.3}$$

Here, A is the surface bounding the volume V.

We can now use the periodic properties of the potential φ. The potential is periodic and continuous, thus φ on the upstream side of V is equal to φ on the downstream side. Also, the unit normal vector points on opposite directions on opposite sides of V. Thus,

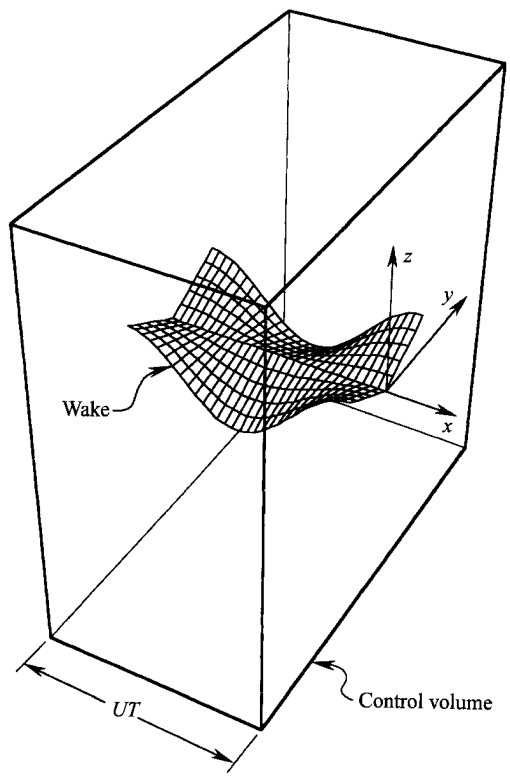

Figure III.2: Control volume enclosing one period of the far wake.

the portion of the integral on the upstream and downstream cancel out. In addition, φ goes to zero far from the wake in the vertical and spanwise direction (y, z). Thus, Equation III.3 becomes

$$\vec{\xi} = -\rho \int \int_S \varphi \vec{n} dA \tag{III.4}$$

where S is the upper and lower surface of the wake.

Finally, the jump in potential across the wing is equal to the bound circulation Γ. Thus, Equation III.4 is equivalent to

$$\vec{\xi} = -\rho \int \int_W \Gamma \vec{n} dA \tag{III.5}$$

where W is the upper surface of one period of the wake.

As mentionned at the beginning of this section, we are interested in computing the forces $\vec{F}$ acting on the wing. We know that $\vec{F}$ is equal and opposite to the time rate of change of momentum deposited in the wake, that is,

$$\vec{F} = -\frac{\xi}{T} = \frac{\rho}{T} \int \int_W \Gamma \vec{n} dA \tag{III.6}$$

We can now find the thrust, lift, and side force, respectively, i.e.,

$$\begin{aligned} T &= \frac{\rho}{T}\int\int_W \Gamma\vec{e_x}\cdot\vec{n}dA \\ L &= \frac{\rho}{T}\int\int_W \Gamma\vec{e_z}\cdot\vec{n}dA \\ S &= \frac{\rho}{T}\int\int_W \Gamma\vec{e_y}\cdot\vec{n}dA \end{aligned} \tag{III.7}$$

The second step is to find the induced power, P_i. As explained previously, the inviscid losses are due to the deposition of kinetic energy into the wake. The power is just the average rate of kinetic energy deposited in the wake per period, which is given by

$$P_i = \frac{\rho}{2T}\int\int\int_V \left|\vec{\nabla}\varphi\right|^2 dV \tag{III.8}$$

Using the first form of Green's theorem, we have,

$$P_i = \frac{\rho}{2T}\left(-\int\int_A \varphi\vec{\nabla}\varphi\cdot\vec{n}dA - \int\int\int_V \varphi\nabla^2\varphi dV\right) \tag{III.9}$$

By using Equation III.1 and the symmetry of φ, we get

$$P_i = -\frac{\rho}{2T}\int\int_S \varphi\vec{\nabla}\varphi\cdot\vec{n}dA \tag{III.10}$$

Also, $\vec{\nabla}\varphi\cdot\vec{n} = \frac{\partial\varphi}{\partial n} = \vec{w}\cdot\vec{n}$ which is the normal wash induced at the surface of the wake. By continuity, we have $\left.\frac{\partial\varphi}{\partial n}\right|_+ = \left.\frac{\partial\varphi}{\partial n}\right|_-$. Thus Equation III.10 becomes

$$P_i = -\frac{\rho}{2T}\int\int_W \Gamma\vec{w}\cdot\vec{n}dA \tag{III.11}$$

As mentioned earlier, the first step is to minimize the inviscid power required to generate a prescribed lift and thrust. In addition, for high angles of attack the wing will stall. Thus, we need to introduce a maximum coefficient of lift constraint. The coefficient of lift is given by

$$C_l = \frac{l}{\frac{1}{2}\rho V^2 c}, l = \rho\Gamma V \tag{III.12}$$

Thus, we have:

$$\Gamma \leq \Gamma_{\max} = \frac{1}{2}C_{l\,\max}Vc \tag{III.13}$$

Similarly,

$$\Gamma \geq \Gamma_{\min} = \frac{1}{2} C_{l\,\min} V c \tag{III.14}$$

To solve this constrained optimization problem, we will use Lagrange multipliers $(\vec{\lambda}, \nu)$ and form the Lagrangian power:

$$\Pi_i = P_i + \vec{\lambda} \cdot \left(\vec{F} - \vec{F_R}\right) + \frac{\rho}{T} \int \int_W \nu \left(\Gamma - \Gamma_{max}\right) dA \tag{III.15}$$

ν is zero if the circulation is smaller than the circulation max and positive otherwise. We can develop Equation III.15 by using Equation III.11 and Equation III.6:

$$\begin{aligned} \Pi_i = & -\frac{\rho}{2T} \int \int_W \Gamma \vec{w} \cdot \vec{n} dA + \vec{\lambda} \cdot \left(\frac{\rho}{T} \int \int_W \Gamma \vec{n} dA - \vec{F_R}\right) + \\ & \frac{\rho}{T} \int \int_W \nu \left(\Gamma - \Gamma_{max}\right) dA \end{aligned} \tag{III.16}$$

The goal is now to minimize Π_i. Taking the variation of Equation III.16 and setting it to zero gives

$$\begin{aligned} \delta \Pi_i = & \delta \vec{\lambda} \cdot \left(\vec{F} - \vec{F_R}\right) + \frac{\rho}{T} \int \int_W \delta \nu \left(\Gamma - \Gamma_{max}\right) dA - \frac{\rho}{2T} \int \int_W \Gamma \delta \vec{w} \cdot \vec{n} dA + \\ & \frac{\rho}{T} \int \int_W \left[\vec{\lambda} \cdot \vec{n} - \frac{1}{2} \vec{w} \cdot \vec{n} + \nu\right] \delta \Gamma dA \end{aligned} \tag{III.17}$$

By using the property of a potential flow (see Appendix A.1) we have

$$\int \int_W \vec{w} \cdot \vec{n} \delta \Gamma dA = \int \int_W \delta \vec{w} \cdot \vec{n} \Gamma dA \tag{III.18}$$

Thus, Equation III.17 becomes

$$\begin{aligned} \delta \Pi_i = & \delta \vec{\lambda} \cdot \left(\vec{F} - \vec{F_R}\right) + \frac{\rho}{T} \int \int_W \delta \nu \left(\Gamma - \Gamma_{max}\right) dA + \\ & \frac{\rho}{T} \int \int_W \left[\vec{\lambda} \cdot \vec{n} - \vec{w} \cdot \vec{n} + \nu\right] \delta \Gamma dA \end{aligned} \tag{III.19}$$

By setting Equation III.19 to zero, we get the following conditions:

$$\begin{aligned} & T = T_R \\ & L = L_R \\ & S = S_R \\ & \nu = 0 \text{ if } \Gamma \prec \Gamma_{\max} \\ & \nu \geq 0 \text{ if } \Gamma \geq \Gamma_{\max} \\ & \vec{w} \cdot \vec{n} = \vec{\lambda} \cdot \vec{n} + \nu \end{aligned} \tag{III.20}$$

The first three conditions are simply that the forces must be equal to the required forces. The last equation of Equation III.20 is the equivalent of the Betz criterion. In the case where the inequality constraint is inactive ($\nu = 0$), this criterion tells us that the induced normal wash produced by the optimum circulation distribution is the same as the normal wash induced by a rigid impermeable wake translating at the velocity $\vec{\lambda}$.

To solve this variational problem, we will discretize the domain and use a vortex-lattice method. One period of the wake is divided into N_{wake} vortex rings. Each ring has a strength of Γ_i.

Let's first rewrite the expression of the force in terms of Γ_i.

$$\vec{F} = \sum_{i=1}^{N_{\text{wake}}} \vec{b_i}\Gamma_i = B\Gamma \tag{III.21}$$

where $\vec{b_i} = \frac{\rho}{T}\vec{n_i}\Delta A_i$, $\vec{n_i}$ is the unit normal at the center of the ring i and ΔA_i is the area of the ring.

Similarly, the induced power can be approximated by

$$P_i = \frac{1}{2}\sum_{i=1}^{N_{\text{wake}}}\sum_{j=1}^{N_{\text{wake}}} K_{ij}\Gamma_i\Gamma_j = \Gamma^T K\Gamma, \text{ with } K_{ij} = -\frac{\rho}{T}\vec{V_{ij}}\cdot\vec{n_i}\Delta A_i \tag{III.22}$$

where $\vec{V_{ij}}$ is the velocity at the center of the panel induced by an infinite row of vortex ring panels of unit strength spaced by the distance UT and the first panel being located at the position on the grid. In practice, I use 20 periods of the wake to compute the induced velocities, 10 periods behind the panel of interest and 10 periods ahead of the panel of interest. We can now rewrite Equation III.16,

$$\Pi_i = \tfrac{1}{2}\sum_{i=1}^{N_{\text{wake}}}\sum_{j=1}^{N_{\text{wake}}} K_{ij}\Gamma_i\Gamma_j + \sum_{i=1}^{N_{\text{wake}}}\sum_{j=1}^{3}\lambda_j\left(B_{ji}\Gamma_i - F_{R_j}\right) + \tfrac{\rho}{T}\sum_{i=1}^{N_{\text{wake}}}\nu\Delta A_i\left(\Gamma_i - \Gamma_{\max i}\right) \tag{III.23}$$

Practically, to solve this optimization problem, we use the augmented Lagrangian method. We take the variation of Equation III.23 set it to zero and we add a quadratic penalty function of weight W to the Lagrangian power that increases the power when the constraint is violated.

We can introduce a new vector of inequality constraint Lagrange multipliers.

$$\nu_i = \frac{\rho}{T}\nu\Delta A_i \tag{III.24}$$

Thus Equation III.23 with the penalty function becomes in matrix notation

$$\Pi_i = \tfrac{1}{2}\Gamma^T K\Gamma + \lambda^T\left(B\Gamma - F_R\right) + \nu^T\left(\Gamma - \Gamma_{\max}\right) + \tfrac{1}{2}\left(\Gamma - \Gamma_{\max}\right)^T W\left(\Gamma - \Gamma_{\max}\right) \tag{III.25}$$

We now can take the variation of Equation III.25,

$$\begin{bmatrix} K + W & B^T \\ B & 0 \end{bmatrix} \begin{Bmatrix} \Gamma \\ \lambda \end{Bmatrix} = \begin{Bmatrix} W\Gamma_{\max} - \nu \\ F_R \end{Bmatrix} \tag{III.26}$$

Finally, Equation III.26 is solved iteratively. We first set W and ν to 0. If the inequality constraint is not satisfied, then we turn on W and ν. For each iteration, we update ν as followed,

$$\nu_{new} = \nu_{old} + W\left(\Gamma - \Gamma_{\max}\right) \tag{III.27}$$

Solving Equation III.26 gives the circulation distribution along the span in the inviscid case.

III.2.2 Minimizing the viscous power

Now that we have the circulation distribution that minimizes the induced power, the next step is to use Γ as an input to now solve the viscous problem by finding the chord that minimizes the total power:

$$P = P_i + P_v \tag{III.28}$$

where P_v is the viscous power defined by

$$P_v = \frac{1}{T}\int\int_W \frac{1}{2}\rho V^2 c C_d dA = \frac{1}{T}\int\int_W \frac{1}{2}\rho\left(U\frac{ds}{dx}\right)^2 c C_d dA \tag{III.29}$$

where $\frac{ds}{dx}$ is the distance traveled by the wing per unit distance traveled by the wing in the x direction.

We can notice that P_v is a function of the chord and the coefficient of drag, which is for low Reynolds number a function of the chord. We now need to find an expression for C_d

as a function of the chord. However C_d is different for each airfoil. Consequently, we could try to find an airfoil that would minimize the viscous losses compare to other airfoils. The coefficient of drag for low Reynolds number scales like the inverse of the square root of the Reynolds number. Thus, we can re-write the viscous power as followed,

$$P_v = \frac{1}{T}\int\int_W \frac{1}{2}\rho V^2 c \frac{C_{d0}}{\sqrt{Re_c}} dA$$
$$P_v = \frac{1}{T}\int\int_W \frac{1}{2}\rho V^2 c \frac{\sqrt{C_l}}{\sqrt{Re_c}} \frac{C_{d0}}{\sqrt{C_l}} dA \tag{III.30}$$

By using $C_l = \frac{\rho V \Gamma}{\frac{1}{2}\rho V^2 c}$, $Re_c = \frac{\rho V c}{\mu}$ we get

$$P_v = \frac{1}{T}\int\int_W \sqrt{\frac{\rho\mu\Gamma}{2}} V \frac{C_{d0}}{\sqrt{C_l}} dA \tag{III.31}$$

As we can see, for a given circulation distribution, the viscous power scales like $C_{d0}/\sqrt{C_l}$. Consequently, we desire an airfoil with the lowest possible parameter $C_{d0}/\sqrt{C_l}$ or the highest $C_l/{C_{d0}}^2$.

A quick way to find the drag polar for various airfoils is to use XFOIL developped by Mark Drela. XFOIL is a two-dimensionnal steady panel code coupled to a two-equations lagged dissipation integral boundary layer formulation. The coupling of the potential code to a boundary layer formulation allows calculation of flows with limited separation region. Consequently by plotting the ratio $C_l/{C_{d0}}^2$ as a function of the angle of attack, we can isolate the best airfoil profile. I will separately look at symmetrical and non-symmetrical airfoils.

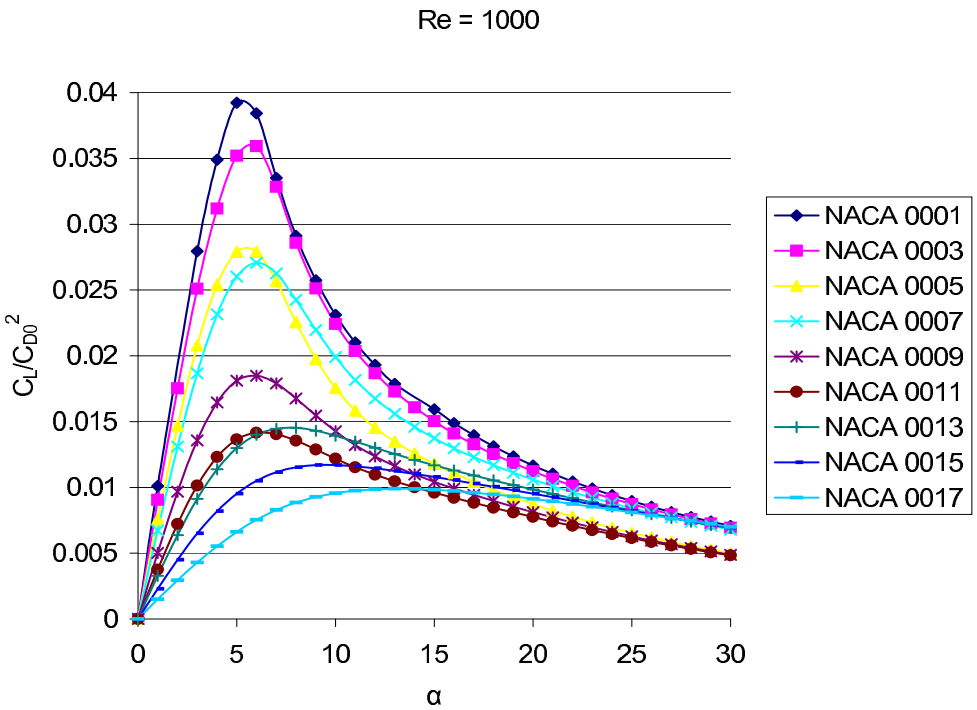

Figure III.3: $C_l/C_{d0}{}^2$ function of the angle of attack for different symmetrical airfoils at $Re = 1000$.

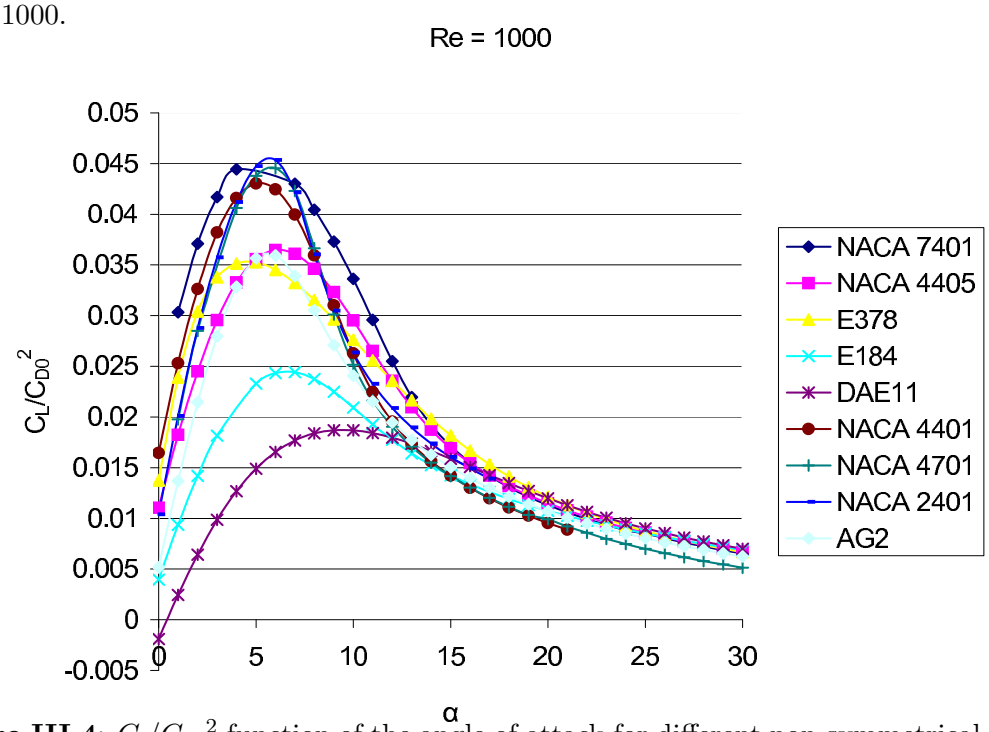

Figure III.4: $C_l/C_{d0}{}^2$ function of the angle of attack for different non-symmetrical airfoils at $Re = 1000$.

As it can be seen in Figure III.3, the best airfoil is the NACA 0001, similarly in Figure III.4 it is the NACA 2401. It can also be observed that the best performing airfoils are the one with the smallest thickness and should be the one used. To use non-symmetrical airfoils, a flexible wing needs to be designed. This results from the fact that the camber of a flapping airfoil is oriented one way during the downstroke and the other way during the upstroke. The use of flexible wings complicate the analysis, consequently I will limit the choice of the airfoil to symmetrical airfoils. Thus, the best performing airfoil is the NACA 0001 and should be the one used. Nevertheless, because the NACA 0001 has a thickness of only 1% of the chord it is extremly hard to manufacture in the case of a MAV. Thus, I limited my choices to a regular symmetric NACA airfoil that could be easily manufactured. I chose the NACA 0009 which performs better than thicker symmetrical airfoils.

Now that the airfoil is chosen, we can find C_d. C_d is a function of both the Reynolds number and the coefficient of lift and thus the chord. The goal is still to model C_d as a function of the chord. As can be seen in Figure III.5, for a $C_l \leq 0.3$, all the scaled curves are on top of each other and almost constant. While for a $C_l \succ 0.3$, all the unscaled curves are on top of each other. From this observation, we can deduce a model for the coefficient of drag,

$$C_d = \begin{cases} f\left(C_l\right) \text{ if } f\left(C_l\right) \succ \frac{3.45}{\sqrt{Re_c}} \\ \frac{3.45}{\sqrt{Re_c}} \text{ otherwise} \end{cases} \tag{III.32}$$

The function f in Equation III.32 is found using a 6th order polynomial interpolation:

$$f\left(x\right) = -0.4236x^6 + 3.2787x^5 - 9.1871x^4 + 12.525x^3 - 8.9124x^2 + 3.5218x^1 - 0.4635 \tag{III.33}$$

The R-squared for the fit is 0.9999.

XFOIL uses a boundary layer formulation to model the viscosity. This formulation usually breaks down for low Reynolds number when the boundary layer becomes really thick. This could be the reason why we do not observe a clear stall. However, the polynomial function used rapidly increases when the coefficient of lift increases as seen in Figure III.6 which compensates for the poor modeling in the stall region. In addition, a constraint on the coefficient of lift is introduced which limits the operation of the wing in its attached

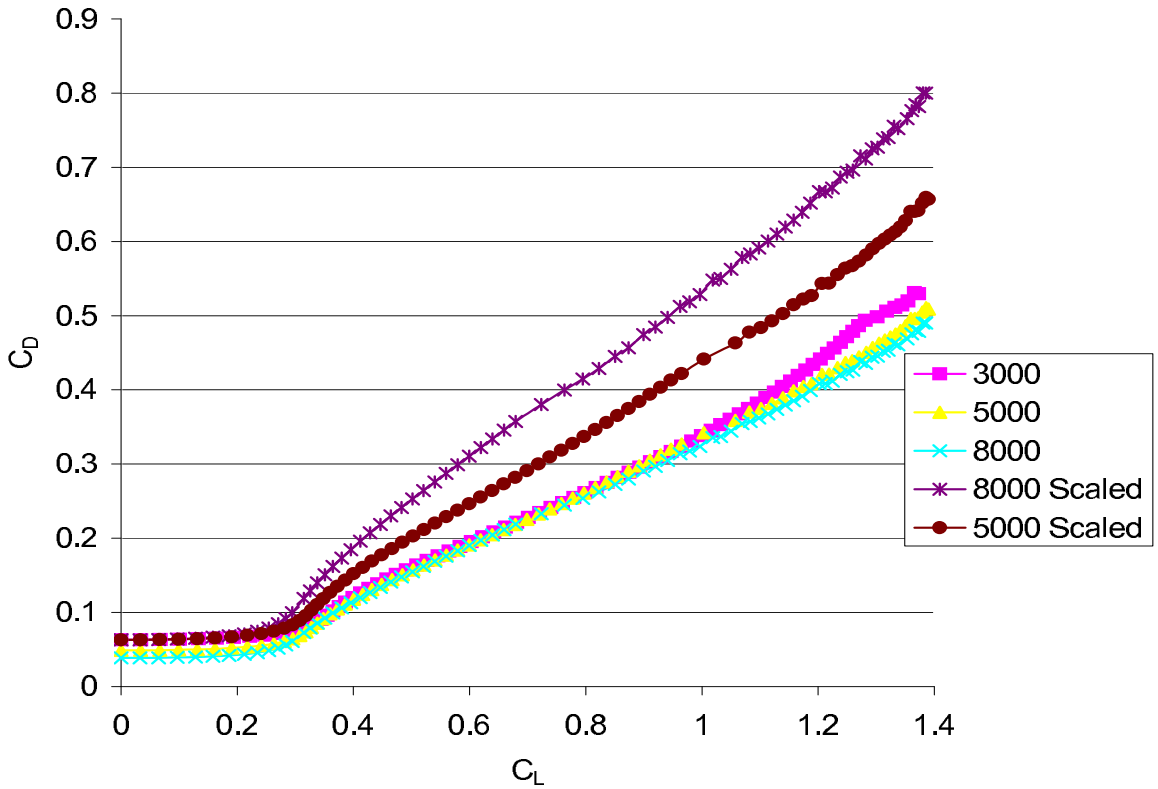

Figure III.5: Drag Polar for NACA 0009 for $Re_c = 3000, 5000, 8000$, the scaled C_d are scaled by $\sqrt{3000/Re_c}$.

region.

We can now discretize the viscous power in Equation III.29,

$$P_v = \frac{\rho}{2T} U^2 \sum_{i=1}^{N_{\text{wake}}} \left(\frac{ds}{dx}\right)_i^2 c_i C_{di}\left(C_{li}, Re_{ci}\right) \Delta A_i \tag{III.34}$$

with, $C_{li} = \frac{2\Gamma_i}{\left(\frac{ds}{dx}\right)_i c_i}$, $Re_{ci} = \frac{\rho U c_i}{\mu}$

Equation III.34 has for only unknown the chord c_i, we can then find a minimum for P_v with the following constraints on the chord,

$$\begin{aligned} c_i &\geq \frac{2\Gamma_i}{\left(\frac{ds}{dx}\right)_i C_{lmax}} \\ c_i &\leq c_{imax} \end{aligned} \tag{III.35}$$

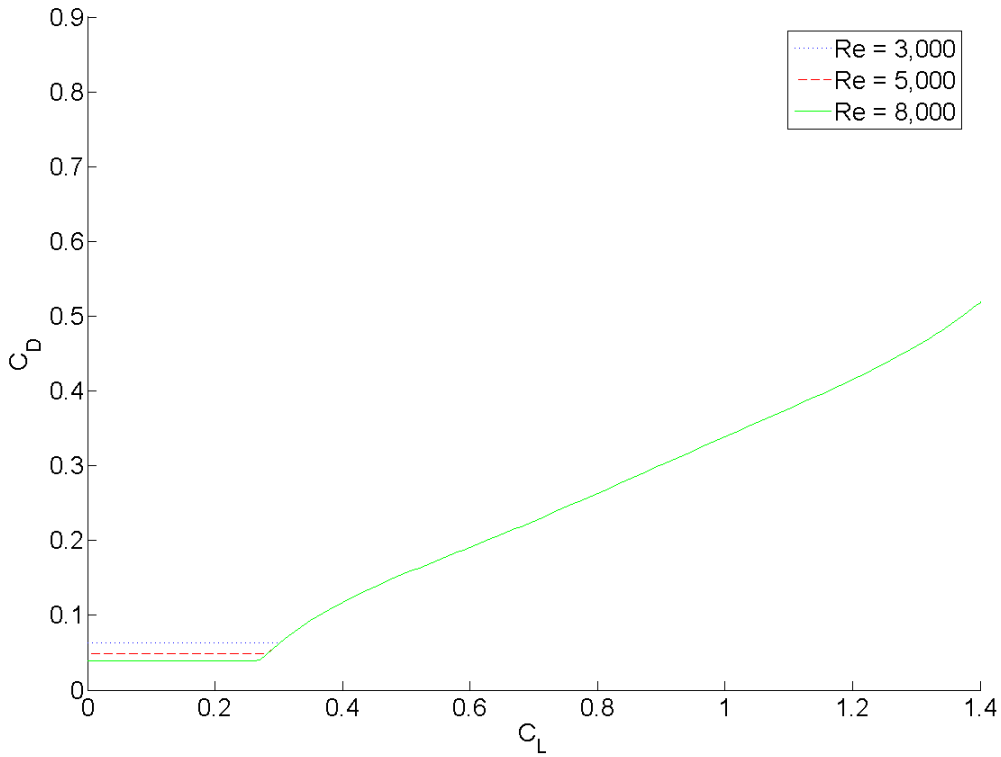

Figure III.6: Drag polar of Equation III.32 for three Reynolds numbers (3,000, 5,000, 8,000).

III.2.3 The hovering case

To summarize, in the previous section we found the optimum circulation distribution in the wake that minimizes the induced power. We then, used this optimum circulation to compute the viscous power as a function of the chord. The chord distribution was then optimized to minimize the viscous losses. However, the calculations were performed on a wake that was convected at the forward flight speed. The problem is now to extend this optimization to flappers in hovering flight.

All the previous equations assumed a forward flight speed U in the x direction. However, when the vehicle is hovering, this velocity goes to zero. Consequently we need to find the speed at which the wake is convected. The actuator disk theory developed in Appendix A.2 links the thrust to the velocity seen behind the disk. Since we prescribe the thrust, we

can extract the velocity behind the flapping wing and use it to convect the wake.

The actuator disk theory (see Appendix A.2) gives an expression for the thrust generated on a rotating disk as a function of the velocity U at this "rotor",

$$T = 2\rho U^2 A \tag{III.36}$$

with A being the area covered by the rotating disk or flapping wings. Thus, we can deduce U:

$$U = \sqrt{\frac{T}{2\rho A}} \tag{III.37}$$

Consequently, for the hover case, we convect the wake at the velocity U provided by Equation III.37.

III.3 Results

We are now able to optimize the circulation distribution in the wake and the chord distribution for flappers in both forward and hovering flight. As mentioned in the introduction, the optimization also depends on two other parameters (flapping frequency and stroke angle). We will see in the two following sections the influence of these two parameters on the optimization for hovering flapping flight.

III.3.1 Stroke angle

It is intuitive to think that the minimum power required is inversely proportional to the stroke angle. In addition, observations made by Weis-Fogh [32] and Altshuler et al. [24, 25] show that stroke angles in flappers are usually high in hovering and range from 120° to 180°. In addition, Altshuler et al. [24, 25] showed that when hummingbirds needed more thrust, they increased their stroke angle.

We can first look at the influence of the stroke angle on the induced power. The

coefficient of induced power is written as

$$C_{P_i} = \frac{P_i}{\frac{1}{2}\rho\left(\frac{T}{\frac{1}{2}\rho\pi B^2\phi/\pi}\right)^{3/2} B^2} \tag{III.38}$$

By using Equation III.38, the induced power scales inversely in $\phi^{3/2}$. It also scales in the flapping frequency cube. By reducing the swept area, the frequency will increase to cover the same swept area in the same time. Consequently, by decreasing the stroke angle, the power decreases in the power of 3/2 while it increases in the power of 3, thus it increases.

In the inviscid case, we proved that it is more efficient for flappers to have high stroke angles. Nevertheless, we also have to take into account the viscous losses. Consequently, I ran the same wing configuration in hover for different stroke angles (the other parameters being held constant). For example, in the following runs, where the only difference is the stroke angle, we can see that the optimal power is lower when the stroke angle is higher:

Runs	Run 1	Run 2	Run3
Stroke angle (°)	175	150	100
Optimal coefficient of power	5.91	6.20	7.93

Table III.1: Optimal coefficient of power as a function of the stroke angle.

III.3.2 Flapping frequency

The power is function of the flapping frequency and for a set configuration, an optimum flapping frequency exists. We can define a non-dimensional flapping frequency as $\tilde{f} = f\frac{2\pi}{\sqrt{\frac{T}{2\rho c_{max}^3 B}}}$. In this example, the following parameters were used:

C_T	2.618
C_{lmax}	1.2
ϕ	150°
AR	6
$\tilde{c_{max}}$	1.0
Airfoil profile	NACA 0009
Drag polar	Polynomial fit

We can plot the coefficients of power (induced, viscous and total) defined in Equation III.38 as a function of the frequency to find the optimum flapping frequency.

As shown in Figure III.7, the minimum power is reached for a non-dimensional flapping frequency of 3.33. We can see that for higher frequencies, the viscous power is predominant compared to the induced power. The U-shape of the power curve is typical and reflects the discussion in section II.3. For lower frequencies, the viscous power is still high because the viscous effects are modeled using a drag polar and for low frequencies, the coefficient of lift will be high, consequently the viscous losses will be high too. We can also notice that the induced power is increasing for decreasing frequencies.

In addition, the optimized wing shape is also given as an output (see Figure III.8). As expected, the chord is always smaller than the chord maximum constraint. The chord also goes to zero at the tip of the wing, which makes sense since the circulation goes to zero at this location.

We can also take a look at the optimum circulation distribution in the wake. Figure III.9 and III.10 show the non-dimensional circulation ($\frac{\Gamma}{B^2\varpi}$) for the optimum case as a

function of the non-dimensional location. We can first notice the symmetry between the upstroke and downstroke. In addition, the circulation is mainly shed at the beginning of the downstroke and upstroke where the gradient of the circulation is the highest.

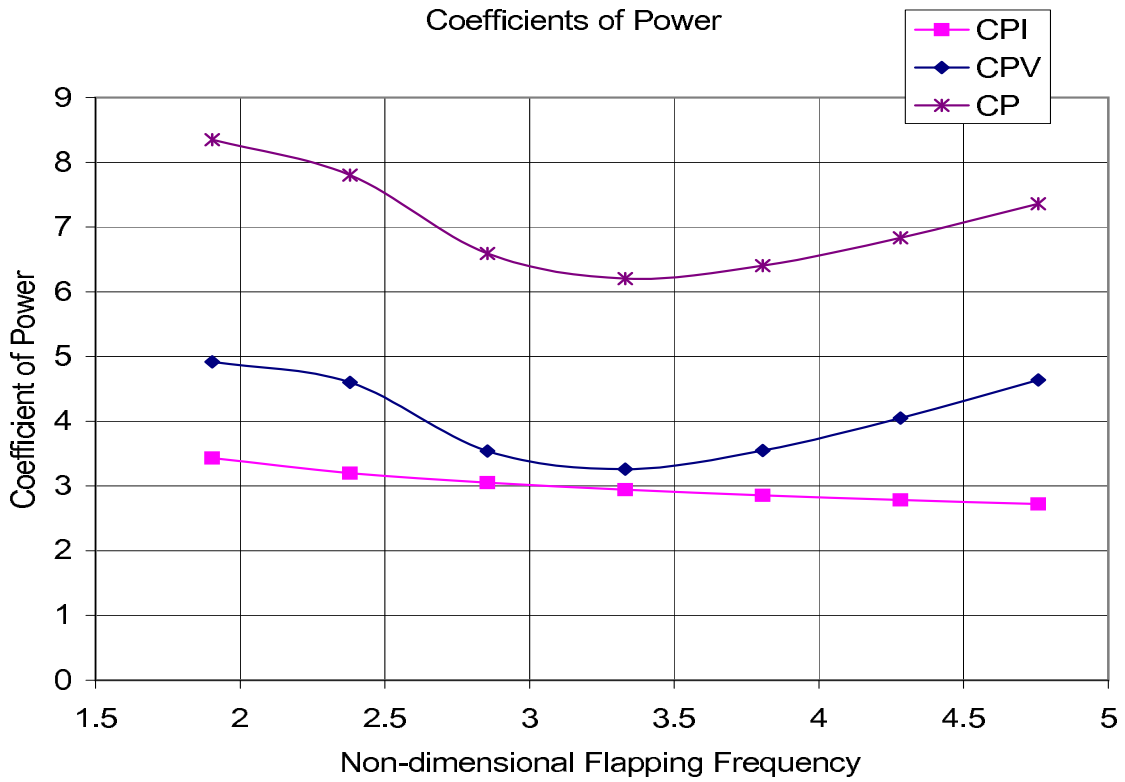

Figure III.7: Coefficients of Power function of the flapping frequency.

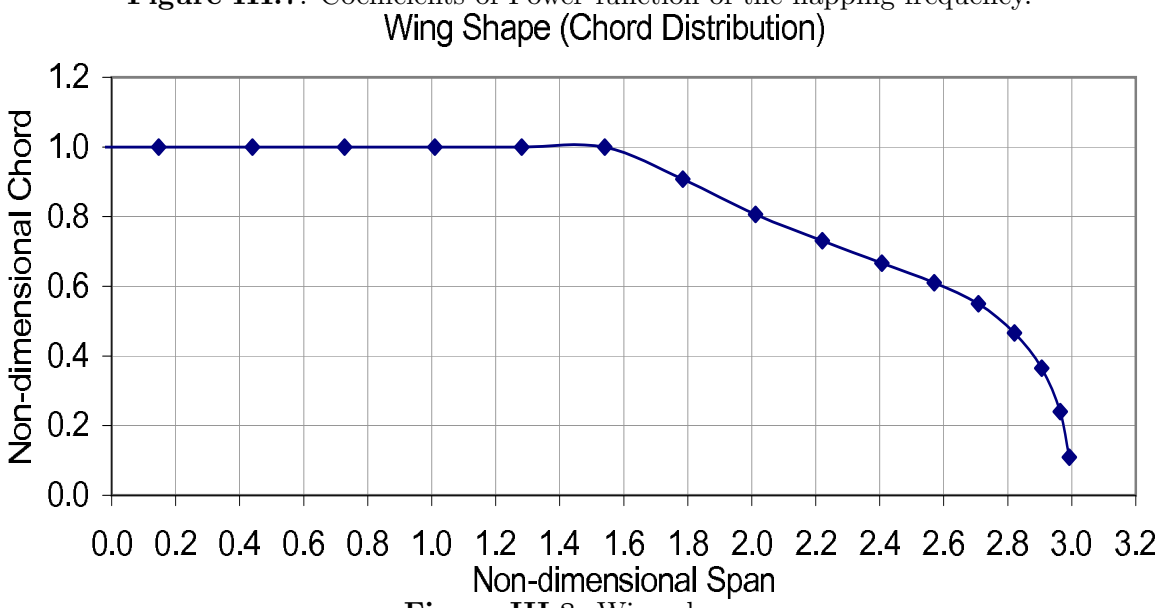

Figure III.8: Wing shape.

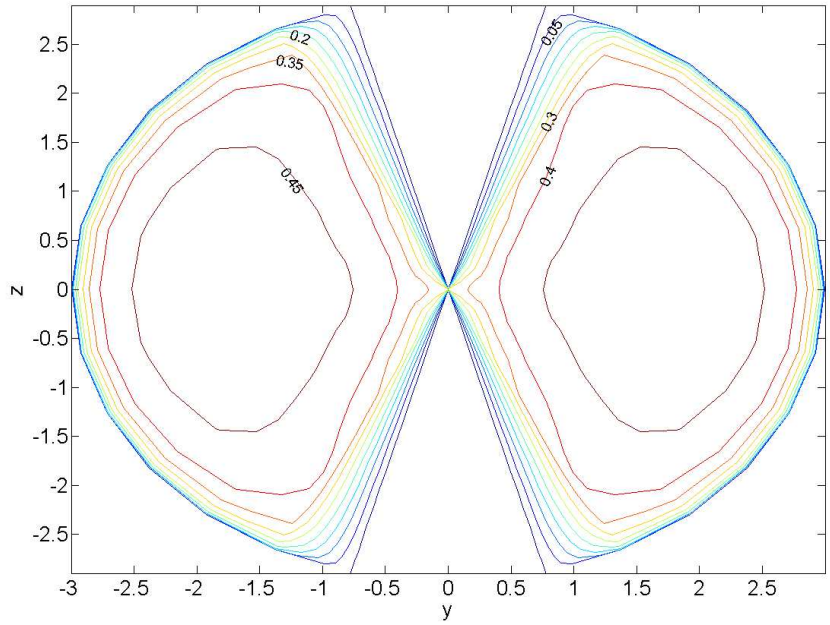

Figure III.9: Rear view of optimal circulation distribution in the wake.

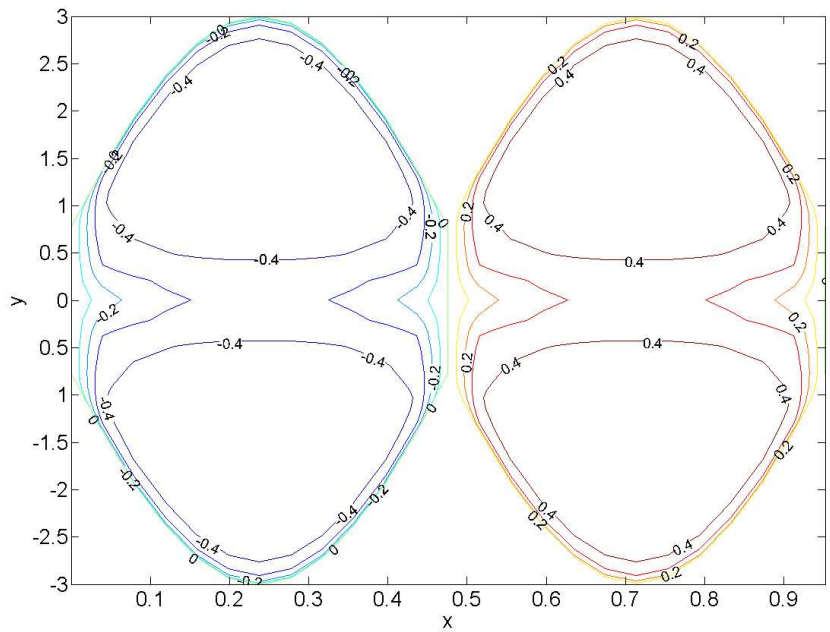

Figure III.10: Top view of optimal circulation distribution in the wake.

Chapter IV

Two-Dimensional Potential Method

IV.1 Problem description

In the previous chapter, we developed an optimization tool for flapping wings in forward and hovering flight. This model was based on the assumption of lightly loaded wings. In other words, it was assumed that the velocity induced by the wake on itself was small compared to the inflow and consequently the roll-up of the wake was neglected. In addition, in the hovering case, the convection speed was deduced from the actuator disk theory.

In our study, we are interested in the hovering case ($k = \infty$) with a flapping amplitude of several times the chord. Thus, the model previously described that uses the actuator disk theory is limited and introduces errors due to its simplifying assumptions. Instead of modeling the wake as rigid, we should freely convect it. By freely convecting the wake, we do not neglect the influence of the induced velocities and remove the assumption of lightly loaded wings. In this chapter, I will present an unsteady two-dimensional potential method that uses a freely convected wake.

IV.2 Literature review

Basu et al. [50] and Jones et al. [9, 10, 45] developed a two-dimensional vortex lattice method. In their method, the airfoil was discretized into panels and the wake was freely convected. I will first give a brief review of the method of Jones et al. Jones used a code first developed by Teng [66]. It is a two-dimensional incompressible unsteady potential code based on a vortex lattice method. He divided the airfoil into N panels. At each time step k, each panel has an unknown constant source strength $(q_j)_k$, $j = 1, \ldots, N$ and the circulation around the airfoil is modeled using a constant vorticity distribution γ_k over the

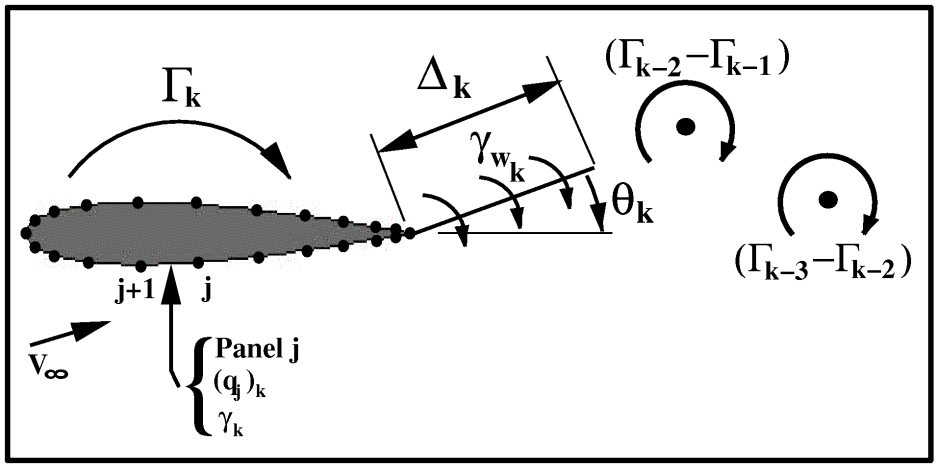

Figure IV.1: Schematic of the Jones et al. panel code. Reprinted from Jones [9].

entire airfoil. Thus, the system has $N+1$ unknowns. In addition, since it is an unsteady method, the vortex shedding process introduces three new unknowns as shown in Figure IV.1, (γ_{w_k}, θ_k, Δ_k). γ_{w_k} represents the constant vorticity strength of the first wake panel, θ_k is the angle of the first wake panel and Δ_k is the length of the first wake panel.

At each time step k, the no through flow condition is applied at the center of the N panels,

$$[(V^n)_i]_k = 0,\ i = 1, \ldots, N \tag{IV.1}$$

where $[(V^n)_i]_k$ is the total normal velocity at the center of panel i at time k. The Kutta condition stipulates that the flow leaves smoothly the trailing edge. In other words, the jump in pressure at the trailing edge is zero. In practice, the Kutta condition is applied at the center of the last plate panel. By using Bernoulli's equation on the upper and lower last panel, we get

$$[P_1]_k + \rho\left[\frac{\partial \Phi_1}{\partial t}\right]_k + \frac{1}{2}\rho\,[(V)_1]_k^2 = [P_N]_k + \rho\left[\frac{\partial \Phi_N}{\partial t}\right]_k + \frac{1}{2}\rho\,[(V)_N]_k^2 \tag{IV.2}$$

By imposing the jump in pressure, $[P_1]_k - [P_N]_k = 0$. In addition, the jump in potential is equal to the circulation, $\left[\frac{\partial \Phi_1}{\partial t}\right]_k - \left[\frac{\partial \Phi_N}{\partial t}\right]_k = \left(\frac{\partial \Gamma}{\partial t}\right)_k$. Finally since the normal velocity is zero at the center of the last panel, $[(V)]_k^2 = \left[(V^t)\right]_k^2$. Thus, the unsteady Kutta condition

becomes

$$\left[\left(V^t\right)_1\right]_k^2 - \left[\left(V^t\right)_N\right]_k^2 = 2\left(\frac{\partial \Gamma}{\partial t}\right)_k = 2\frac{\Gamma_k - \Gamma_{k-1}}{t_k - t_{k-1}} \tag{IV.3}$$

So far we have $N+1$ equations for $N+4$ unknowns. The Helmholtz theorem stipulates that the circulation shed into the wake is equal and opposite to the change of circulation around the airfoil. This provides another condition

$$\Gamma_k + \Delta_k \gamma_{w_k} = \Gamma_{k-1} \tag{IV.4}$$

The two additional relations can be obtained using the assumptions presented by Basu and Hancock [50], that is,

- The wake panel is oriented in the direction of the local resultant velocity at the panel midpoint.
- The length of the wake panel is equal to the local velocity strength at the panel midpoint times the size of the time step.

These two conditions can be expressed as,

$$\begin{aligned} \tan\theta_k &= \tfrac{(v_w)_k}{(u_w)_k} \\ \Delta_k &= (t_k - t_{k-1})\sqrt{(v_w)_k^2 + (u_w)_k^2} \end{aligned} \tag{IV.5}$$

Finally, at the end of each time step, the point vortices in the wake are convected with the local velocity field.

The method developed is similar to the one presented above. A flat plate is modeled using a method inspired by Jones et al. but instead of a constant strength source distribution, the vorticity has a linear distribution. This approach is more accurate than Jones' method since the order of the distribution is higher. In addition, instead of point vortices, the vorticity in the wake is modeled using a constant vorticity distribution. The use of a higher-order distribution in the wake is motivated by the fact that we are especially interested in hovering. In the case of hovering, the roll-up of the wake is particularly important and having a higher-order distribution smooths the behavior of the wake. Jones also explains that he uses an iterative scheme because the Kutta condition is non-linear. However

his iterative scheme was a simple shooting method and had a weak convergence. Here, we use a Newton method which has a strong convergence. Finally, Jones et al. did not study the hovering case; here we are concerned primarily with hover. The method developed will be detailed in the following section.

IV.3 Approach

In this section, details of the two-dimensional unsteady potential method developed are be presented. First, we define the kinematics of the plate we want to study. In a second part, the theory itself is presented. Finally in the last sub-section, various convergence tests are performed to validate the method presented.

IV.3.1 Kinematics

We want to model the motion of flapping wings. Consequently, in two-dimensions, the motion we are interested in has two degrees of freedom. The kinematics is presented in Figure IV.2. The plate motion is a combination of plunging and pitching with the following kinematics,

$$\begin{aligned} h &= \sum_{i=1}^{N_m} h_n \sin(\varpi_n t) \\ \theta &= \sum_{i=1}^{N_m} \theta_n \sin(\varpi_n t + \phi_n) \\ y &= h + \xi \sin(-\theta) \\ x &= \xi \cos(-\theta) + e \end{aligned} \tag{IV.6}$$

where N_m is the number of Fourier modes used to describe the plate motion, h is the amplitude of the plunge, θ the pitch angle, ϖ_n the angular velocity of mode n, ϕ_n the phase shift of the pitch angle compared to the plunge, (x, y) are the coordinates of the plate in a fixed Cartesian coordinate system initially centered at the center of the plate, e is the location of the pitch axis and (ξ, η) is the coordinate system associated with the plate centered at the pitch axis. The black dot represents the pitch axis, while the white dot represents the center of the plate.

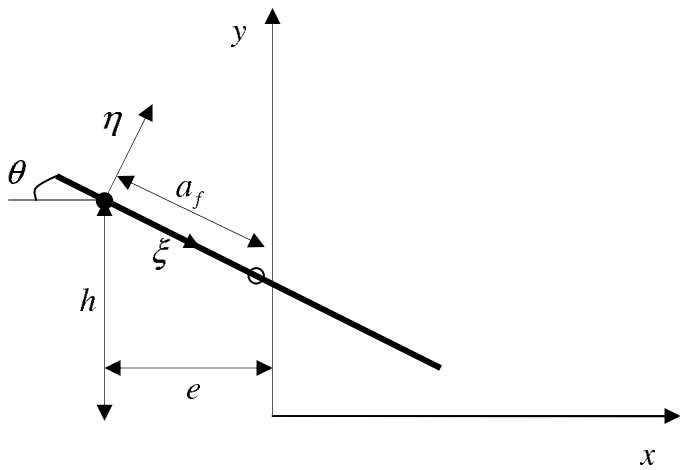

Figure IV.2: Kinematics of the flat plate used in the present method

Having now defined the kinematics of the plate, we now look at the formulation used to develop the present method.

IV.3.2 Potential method

The method used is based mainly on the work of Jones et al. [9, 10, 45]. It is a potential panel code that uses a freely convected wake. I will first present the equations behind the theory. Since it is a potential method, the viscosity is neglected. Consequently, in a second part, I will explain the correction used to take into account the influence of the viscosity.

a Inviscid formulation

The surface of the plate is modeled using panels each containing a linear distribution of vorticity. The wake is also modeled using panels but with constant vorticity. First, we can express the velocities induced by these panels.

The velocity induced by a constant strength vortex distribution (γ) panel extending from $(x_1, 0)$ to $(x_2, 0)$ at a point (x, y) was calculated by Katz and Plotkin [12]. The corresponding velocities in the x and y direction are given by respectively,

$$\begin{aligned} u &= \frac{\gamma}{2\pi}\left[\arctan\left(\frac{y}{x-x_2}\right) - \arctan\left(\frac{y}{x-x_1}\right)\right] \\ v &= \frac{\gamma}{4\pi}\ln\left[\frac{(x-x_2)^2+y^2}{(x-x_1)^2+y^2}\right] \end{aligned} \tag{IV.7}$$

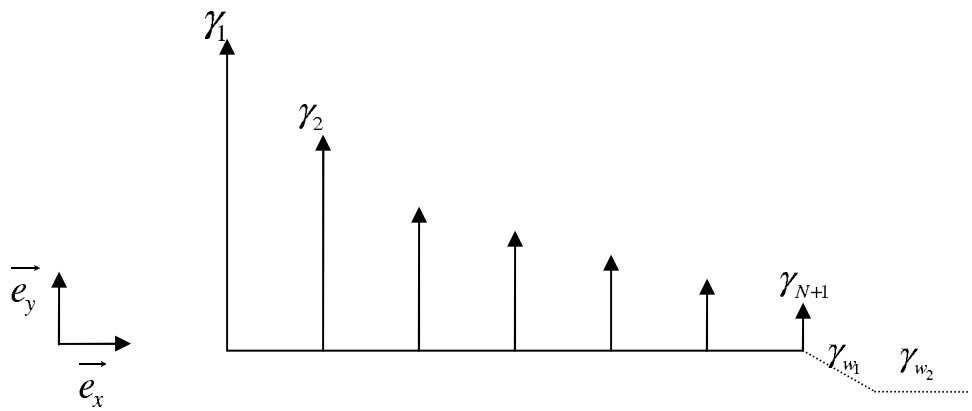

Figure IV.3: Flat plate with linear vorticity distribution and its wake.

Similarly, for a linear vortex distribution ($\gamma = \gamma_1 x$), the induced velocites are

$$\begin{aligned} u &= -\frac{\gamma_1}{4\pi}\left[y \ln\left[\frac{(x-x_1)^2+y^2}{(x-x_2)^2+y^2}\right] - 2x\left(\arctan\left(\frac{y}{x-x_2}\right) - \arctan\left(\frac{y}{x-x_1}\right)\right)\right] \\ v &= -\frac{\gamma_1}{2\pi}\left[\frac{x}{2} \ln\left[\frac{(x-x_1)^2+y^2}{(x-x_2)^2+y^2}\right] + (x-x_1) + y\left(\arctan\left(\frac{y}{x-x_2}\right) - \arctan\left(\frac{y}{x-x_1}\right)\right)\right] \end{aligned} \tag{IV.8}$$

We can now form the system of equations to solve for the unknown vortex strengths. The plate is composed of N panels with $N+1$ vorticity unknowns at the end points of each panel (see Figure IV.3), since we are using linear panels. In addition, the vortex strength of the first panel of the wake is also an unknown. By applying N no through flow conditions at the center of each panels, a Kutta condition and the Helmholtz theorem, we get a closed system. For the Kutta condition, we specify that the jump in pressure at the center of the last panel is zero. I will now detail each of the equations that form the system we need to solve.

First, the N no through flow conditions at time step k can be written as a linear system,

$$[A]^k (\gamma)^k = (b)^k \tag{IV.9}$$

where the $(N) \times (N+2)$ matrix $[A]$ is the influence coefficient matrix. (b) is the right hand side vector which is the sum of the induced velocities due to the wake (except the first panel), the freestream and the velocity of the plate. (γ) are the unknown vortex strengths on the plate plus the first wake panel vortex strength.

Second, the Helmholtz theorem is also a linear condition in (γ), and is given by

$$\left[\int_{\text{plate}} \gamma ds\right]^k + \left[\int_{\text{wake 1st panel}} \gamma_{w_1} ds\right]^k = \left[\int_{\text{plate}} \gamma ds\right]^{k-1} \tag{IV.10}$$

We can rewrite Equation IV.10 in term of the circulation,

$$\Gamma^k + \Gamma^k_{w_1} = \Gamma^{k-1} \tag{IV.11}$$

where $\Gamma^k = \left[\int_{\text{plate}} \gamma ds\right]^k = \frac{1}{2}\sum_{i=1}^{N}\left(\gamma_i^k + \gamma_{i+1}^k\right)\Delta_i^k$

$\Gamma^{k-1} = \left[\int_{\text{plate}} \gamma ds\right]^{k-1} = \frac{1}{2}\sum_{i=1}^{N}\left(\gamma_i^{k-1} + \gamma_{i+1}^{k-1}\right)\Delta_i^{k-1}$

$\Gamma^k_{w_1} = \left[\int_{\text{wake 1st panel}} \gamma_{w_1} ds\right]^k = \gamma^k_{w_1}\Delta^k_{w_1}$

Δ_i^k is the length of panel i at time step k and $\Delta^k_{w_1}$ is the length of the first wake panel at time step k.

Last, the Kutta condition is non-linear in (γ) and can be expressed similarly as in section IV.2 by using the Bernoulli's equation,

$$\left[\left(V^t\right)^k_{N^-}\right]^2 - \left[\left(V^t\right)^k_{N^+}\right]^2 = 2\frac{\Gamma^k - \Gamma^{k-1}}{\Delta t} \tag{IV.12}$$

where $\left[\left(V^t\right)^k_{N^-}\right]$ and $\left[\left(V^t\right)^k_{N^+}\right]$ are respectively the lower and upper tangential velocity at the collocation point of the last panel of the plate.

We can express the tangential velocities of Equation IV.12 as functions of the unknown vortex strengths,

$$\begin{aligned}\left[\left(V^t\right)^k_{N^-}\right] &= \left[-0.25\left(\gamma^k_{N+1} + \gamma^k_N\right) + C^k\gamma^k_{w_1}\Delta^k_{w_1} + W^k\right]\\ \left[\left(V^t\right)^k_{N^+}\right] &= \left[0.25\left(\gamma^k_{N+1} + \gamma^k_N\right) + C^k\gamma^k_{w_1}\Delta^k_{w_1} + W^k\right]\end{aligned} \tag{IV.13}$$

where C^k is the influence coefficient of the first wake panel on the center of the last panel of the plate. W^k is the sum of the induced velocities due to the rest of the wake, the freestream and the velocity of the plate at the center of the last panel. By expanding Equation IV.12 using Equation IV.13, we get

$$-\gamma^k_N C^k\gamma^k_{w_1}\Delta^k_{w_1} - \gamma^k_N W^k - \gamma^k_{N+1}C^k\gamma^k_{w_1}\Delta^k_{w_1} - \gamma^k_{N+1}W^k = 2\frac{\Gamma^k - \Gamma^{k-1}}{\Delta t} \tag{IV.14}$$

In addition, by using Helmholtz theorem from Equation IV.11, Equation IV.14 becomes

$$-\gamma_N^k C^k \gamma_{w_1}^k \Delta_{w_1}^k - \gamma_N^k W^k - \gamma_{N+1}^k C^k \gamma_{w_1}^k \Delta_{w_1}^k - \gamma_{N+1}^k W^k + 2\frac{\gamma_{w_1}^k \Delta_{w_1}^k}{\Delta t} = 0 \tag{IV.15}$$

Finally, by gathering the no through flow conditions, the Kutta condition and Helmholtz theorem, we have the following system:

$$F^k\left(\gamma_1, \ldots, \gamma_{N+1}, \gamma_{w_1}\right) = 0 \tag{IV.16}$$

where $F^k\left(\gamma_1, ;\gamma_{N+1}, \gamma_{w_1}\right)$ is a $N+2$ vector, the first $N+1$ equations being linear in the unknown vortex strengths.

We can solve Equation IV.16 using the Newton's method (see Appendix B.1). We first need to compute the Jacobian $[J]^k$ of the system in Equation IV.16. The upper left sub-matrix of $[J]^k$ is simply the $(N) \times (N+2)$ matrix $[A]^k$ since Equation IV.9 is a linear system.

The row $N+1$ comes from the conservation of the circulation developed in Equation IV.11,

$$\begin{aligned}
[J]_{N+1,1}^k &= \frac{\partial F_{N+1}^k}{\partial \gamma_1^k} = \tfrac{1}{2}\Delta_1^k \\
[J]_{N+1,j}^k &= \frac{\partial F_{N+1}^k}{\partial \gamma_j^k} = \Delta_j^k,\ j = 2, \ldots, N \\
[J]_{N+1,N+1}^k &= \frac{\partial F_{N+1}^k}{\partial \gamma_{N+1}^k} = \tfrac{1}{2}\Delta_{N+1}^k \\
[J]_{N+1,N+2}^k &= \frac{\partial F_{N+1}^k}{\partial \gamma_{w_1}^k} = \Delta_{w_1}^k
\end{aligned} \tag{IV.17}$$

The row $N+2$ comes from the Kutta condition expressed in Equation IV.15,

$$\begin{aligned}
[J]_{N+2,j}^k &= \frac{\partial F_{N+2}^k}{\partial \gamma_j^k} = 0,\ j = 1, \ldots, N-1 \\
[J]_{N+2,N}^k &= \frac{\partial F_{N+2}^k}{\partial \gamma_N^k} = -C^k \gamma_{w_1}^k \Delta_{w_1}^k - W^k \\
[J]_{N+2,N+1}^k &= \frac{\partial F_{N+2}^k}{\partial \gamma_{N+1}^k} = -C^k \gamma_{w_1}^k \Delta_{w_1}^k - W^k \\
[J]_{N+2,N+2}^k &= \frac{\partial F_{N+2}^k}{\partial \gamma_{w_1}^k} = -C^k \left(\gamma_N^k + \gamma_{N+1}^k\right) \Delta_{w_1}^k + \frac{2\Delta_{w_1}^k}{\Delta t}
\end{aligned} \tag{IV.18}$$

We can summarize the algorithm with the following steps:

1. Compute the location of the plate at time step k.

2. Form the $[A]^k$ matrix and $(b)^k$ vector.

3. Form the Jacobian matrix $[J]^k$.

4. Solve iteratively on i until convergence is reached the following system: $\left(\gamma^{i+1}\right)^k = \left(\gamma^i\right)^k - \left(\left[J\left(\left(\gamma^i\right)^k\right)\right]^k\right)^{-1} F^k\left(\left(\gamma^i\right)^k\right)$.

5. Compute the aerodynamic forces and power acting on the plate.

6. Update the location of the wake and go back to step 1.

We have described the first four steps. We will now explain the last two steps. The wake panels are simply updated with the local velocity field as material lines. The induced velocities are computed at the end points of each wake panels and a backward Euler scheme is used to get the new position of the panels,

$$x_{w_i}^{k+1} = x_{w_i}^k + U\left(x_{w_i}^k\right)\Delta t,\ i = 1, \ldots, k+1 \tag{IV.19}$$

where x^k is the position vector of the ith point of the wake at time step k and $U\left(x_{w_i}^k\right)$ is the velocity vector at that point.

Special care due to stretching must be taken to conserve the circulation of each wake panel. The new vorticity strength becomes

$$\gamma_{w_i}^{k+1} = \gamma_{w_i}^k \frac{\Delta_{w_i}^k}{\Delta_{w_i}^{k+1}},\ i = 1, \ldots, k \tag{IV.20}$$

The aerodynamic forces per unit depth are computed using the unsteady Kutta-Joukowsky formula,

$$\vec{F}_{aero} = \rho \int_{-b}^{b} \left[\vec{U} \times \vec{\gamma} + \frac{d}{dt}\int_{-b}^{x} \gamma \vec{n} ds\right] ds \tag{IV.21}$$

The first term of Equation IV.21, $\int_{-b}^{b}\left[\vec{U} \times \vec{\gamma}\right] ds$, is given by

$$\int_{-b}^{b}\left[\vec{U} \times \vec{\gamma}\right] ds = \int_{-b}^{b} [u\gamma\vec{e_y} - v\gamma\vec{e_x}] ds \tag{IV.22}$$

On each panel of the airfoil, we can approximate the velocity $\vec{U}$ by being constant over a panel and having the value of the velocity at the center of the panel. Thus, Equation IV.22

becomes

$$\int_{-b}^{b} [u\gamma\vec{e_y} - v\gamma\vec{e_x}]ds = \sum_{i=1}^{N} (u_i\vec{e_y} - v_i\vec{e_x}) \int_{x_i}^{x_{i+1}} [\gamma_i]\, ds \tag{IV.23}$$

Since γ_i is a linear function, Equation IV.23 can be expanded as,

$$\sum_{i=1}^{N} (u_i\vec{e_y} - v_i\vec{e_x}) \left(\frac{\Delta_i}{2}\right) (\gamma_i + \gamma_{i+1}) \tag{IV.24}$$

In the same way, the second term of Equation IV.21 becomes

$$\int_{-b}^{b} \left[\frac{d}{dt}\int_{-b}^{x} \gamma\vec{n}ds\right] ds = \sum_{i=1}^{N} \int_{x_i}^{x_{i+1}} \left[\frac{d}{dt}\int_{x_1}^{x} \gamma\vec{n}ds\right] ds \tag{IV.25}$$

The first term in the sum of Equation IV.25 can be expanded as

$$\begin{aligned}\int_{x_1}^{x_2} \left[\frac{d}{dt}\int_{x_1}^{x} \gamma\vec{n}ds\right] ds &= \frac{d}{dt}\int_{x_1}^{x_2} \left[\left(\frac{a_1}{2}x^2 + b_1x\right) - \left(\frac{a_1}{2}x_1^2 + b_1x_1\right)\right] ds\vec{n} \\ &= \frac{d}{dt}\left[\left(\frac{a_1}{6}x_2^3 + \frac{b_1}{2}x_2^2\right) - \left(\frac{a_1}{6}x_1^3 + \frac{b_1}{2}x_1^2\right) - \left(\frac{a_1}{2}x_1^2 + b_1x_1\right)\Delta_1\right]\vec{n}\end{aligned} \tag{IV.26}$$

with, $a_1 = \frac{\gamma_2 - \gamma_1}{\Delta_1}, b_1 = \frac{x_2\gamma_1 - x_1\gamma_2}{\Delta_1}$

We can also expand the other terms,

$$\begin{aligned}&\int_{x_i}^{x_{i+1}} \left[\frac{d}{dt}\int_{x_1}^{x} \gamma\vec{n}ds\right] ds = \frac{d}{dt}\int_{x_2}^{x_3} \left[\sum_{j=1}^{i-1}\left(\frac{\Delta_j}{2}\right)(\gamma_j + \gamma_{j+1}) + \left(\frac{a_i}{2}x^2 + b_ix\right) - \left(\frac{a_i}{2}x_i^2 + b_ix_i\right)\right] ds\vec{n} \\ &= \frac{d}{dt}\left[\Delta_i\sum_{j=1}^{i-1}\left(\frac{\Delta_j}{2}\right)(\gamma_j + \gamma_{j+1}) + \left(\frac{a_i}{6}\left(x_{i+1}^3 - x_i^3\right) + \frac{b_i}{2}\left(x_{i+1}^2 - x_i^2\right)\right) - \left(\frac{a_i}{2}x_i^2 + b_ix_i\right)\Delta_i\right]\vec{n}\end{aligned} \tag{IV.27}$$

with, $a_i = \frac{\gamma_{i+1} - \gamma_i}{\Delta_i}, b_i = \frac{x_{i+1}\gamma_i - x_i\gamma_{i+1}}{\Delta_i}$

Finally, the force becomes

$$\begin{aligned}&\vec{F_{aero}} = \rho\sum_{i=1}^{N} (u_i\vec{e_y} - v_i\vec{e_x}) \left(\tfrac{\Delta_i}{2}\right)(\gamma_i + \gamma_{i+1}) + \\ &\rho\tfrac{d}{dt}\sum_{i=1}^{N}\left[\Delta_i\sum_{j=1}^{i-1}\left(\tfrac{\Delta_j}{2}\right)(\gamma_j + \gamma_{j+1}) + \left(\tfrac{a_i}{6}x_{i+1}^3 + \tfrac{b_i}{2}x_{i+1}^2\right) - \left(\tfrac{a_i}{6}x_i^3 + \tfrac{b_i}{2}x_i^2\right) - \left(\tfrac{a_i}{2}x_i^2 + b_ix_i\right)\Delta_i\right]\vec{n}\end{aligned} \tag{IV.28}$$

The time derivative in Equation IV.28 is computed by using a backward Euler scheme. The aerodynamic power is computed the same way,

$$P_{aero} = \rho \int_{-b}^{b} \left[\left(\vec{U} \times \vec{\gamma} + \frac{d}{dt} \int_{-b}^{x} \gamma \vec{n} ds \right) \cdot \vec{U}_{\text{airfoil}} \right] ds \tag{IV.29}$$

$\vec{U}_{\text{airfoil}}$ is the velocity of the airfoil computed at the center of each panel and is taken constant over a panel.

To summarize, in this section, I presented the system we solve to obtain the unknown vortex strengths for a two-dimensional flapping airfoil. Once the strenghts are known, I showed how to update the location of the wake, and finally, how to compute the aerodynamic forces and power. In the following section, I will introduce a corrective term to take into account the presence of viscous effects.

b Viscous formulation

To accurately model the effect of viscosity, one should solve the full Navier-Stokes equations. Nevertheless, it is possible to include the effect of viscosity in a potential code. Jones et al. [45] used the Keller-Cebeci box method [67]. However this method cannot model low Reynolds number flows, and is limited to small reduced frequencies. Thus, in our particular case of interest (hover at low Reynolds number), this method is not helpful. Instead of modifying the flow characteristics, we choose to add a correction factor in the computation of the aerodynamic forces. In the method presented, the viscous forces are modeled as

$$\begin{aligned} \vec{F}_{viscous} &= \tfrac{1}{2}\rho U^2 c C_D \frac{\vec{U}}{\|\vec{U}\|} \\ P_{viscous} &= \vec{F}_{viscous} \cdot \vec{U}_{\text{airfoil}} \\ \vec{U} &= \text{Induced velocity - plate velocity} \end{aligned} \tag{IV.30}$$

where $\vec{U}$ is computed at a point taken on the plate. In practice, $\vec{U}$ is taken as being the velocity given by the actuator disk theory for a given thrust minus the plate velocity. Consequently the viscous force can be fully computed during the post-processing of the inviscid results. Adding the viscous corrective term during the post-processing step allows

us to test various drag models without having to re-run the full inviscid code. We use two different models for the drag.

The first model is the drag polar model used in Equation III.32. The coefficient of drag is inversely proportional to the square root of the Reynolds number (computed based on the chord and the velocity $\vec{U}$) for small lift coefficient and is modeled as a polynomial function for higher lift coefficients. We already saw in section III.2.2 that this drag polar model introduces errors in the stall region because this region is poorly modeled in XFOIL for low Reynolds numbers.

The second model uses a constant drag coefficient. It is based on experimental measurements done by Weis-Fogh [32]. He was able to measure the average drag coefficient for different insects.

Both these models are steady state models. They obviously do not reflect the dynamic stall process that is often encountered in flapping flight. Nevertheless, experimental studies (Wells [27] and Ramamurti et al. [13]) showed that in hover, the aerodynamic was mainly governed by inviscid effects.

Now that we have developed a computational model to anaylze the flow, forces and power of a two-dimensional flapping plate, we need to test the model to see if it agrees with well known answers to various limit cases.

IV.3.3 Convergence study

In this section, I will compare the results of the present method for various configurations. First the small amplitude motion is computed. Then the wake patterns given by the model developed are compared to experimental results. Finally, the accuracy of the model for large amplitude motion in hover is studied.

a Small amplitudes

In this section, I compare the aerodynamic results obtained using the present method to the results of Azuma et al. [47]. Azuma's results are based on the thin airfoil theory

and the work done by Theodorsen. Let us consider a flat plate (no deflection) in pitching and plunging motion (see Figure IV.2) with the following kinematics,

$$\begin{aligned} h &= h_1 \sin(\varpi t) \\ \theta &= \theta_1 \sin(\varpi t + \phi) \end{aligned} \tag{IV.31}$$

Azuma et al. derived the expressions for the mean lift, thrust and power per unit depth. For pure plunging motion, we have

$$\begin{aligned} L &= 0 \\ T &= \pi\rho b U^2 \left[\left\{ \left(F^2 + G^2\right) \left(\left(\frac{h_1}{b}\right)^2 k^2 \right) \right\} \right] \\ P &= \pi\rho b U^3 \left[F \left(\frac{h_1}{b}\right)^2 k^2 \right] \end{aligned} \tag{IV.32}$$

For pure pitching motion, we have

$$\begin{aligned} L &= 0 \\ T &= \pi\rho b U^2 \left[\begin{array}{l} \left\{ \left(F^2 + G^2\right) \left(\theta_1^2\right) \right\} \\ +0.25 \left\{ \left(1 - F + 2a_f F\right)^2 - 2a_f + \left(1 - 2a_f\right)^2 G^2 \right\} \theta_1^2 k^2 \\ - \left\{ \left(0.5 + a_f\right) G k + F \right\} \theta_1^2 \end{array} \right] \\ P &= \pi\rho b U^3 \left[\left\{ \left(0.25 - a_f\right) - 0.5 \left(0.5 - a_f\right) F - \left(0.5 + a_f\right) G k^2 \right\} \theta_1^2 \right] \end{aligned} \tag{IV.33}$$

With,

$$\begin{aligned} C(k) &= \frac{H_1^{(2)}(k)}{H_1^{(2)}(k) + j H_0^{(2)}(k)} \\ F &= \mathrm{Re}\left(C(k)\right) \\ G &= \mathrm{Im}\left(C(k)\right) \end{aligned} \tag{IV.34}$$

Since the mean lift is zero in both cases, I will compare the results of the present model to Azuma's results by comparing the computed maximum of the lift. Theodorsen [15] and Garrick [16] get for the maximum of the lift in plunging motion

$$|L| = 2\pi\rho U^2 b \sqrt{\left[\left(2kh_1\right)^2 \left(F^2 + G^2 + kG + \frac{k^2}{4} \right) \right]} \tag{IV.35}$$

In pure pitching motion, Theodorsen [15] and Garrick [16] also get

$$|L| = 2\pi\rho U^2 b \sqrt{\left[\theta_1^2 \left\{ \begin{array}{l} \left(1 + \left(a_f - 0.5\right)^2 k^2\right) \left(F^2 + G^2\right) + 0.5 k^2 F \\ + \left(k + a_f \left(a_f - 0.5\right) k^3\right) G + 0.25 \left(1 + a_f^2 k^2\right) k^2 \end{array} \right\} \right]} \tag{IV.36}$$

These analytical results will be used in the following sections to compare the results of the present model. First, the lift obtained using the present model will be compared to an approximation of the Wagner function for a sudden change in picth. Then, we will focus on sinusoidal plunging motion, by comparing results of the present method to the analytical formulas presented above. Finally, we will also look at sinusoidal pitching motion about the elastic axis.

a.1 Sudden change in pitch

For a sudden change in pitch, we can compare the lift to the Wagner function ϕ. For the lift we have

$$L(s) = 2\pi\rho U^2 b\theta\phi(s)\,,\; s = \frac{Ut}{b} \tag{IV.37}$$

The function $\phi(s)$ can be approximated by the following function

$$\phi(s) \approx 1 - 0.165e^{-0.0455s} - 0.335e^{-0.3s} \tag{IV.38}$$

This first order approximation can be improved. Coller and Chamara [72] developed a higher order approximation,

$$\phi(s) \approx 1 - \sum_{j=1}^{N_\phi} K_j e^{-\sigma_j s} \tag{IV.39}$$

with $N_\phi = 4$, $K_1 = 0.2552078488$, $\sigma_1 = 0.1708445093$, $K_2 = 0.1290432917$, $\sigma_2 = 0.5610424665$, $K_3 = 0.09654817188$, $\sigma_3 = 0.04680475392$, $K_4 = 0.01920068755$, $\sigma_4 = 0.006478169099$. As we can see in Figure IV.4, there is a good agreement. Nevertheless for higher non-dimensional time, we can see some discrepancies. This could be explained by the fact that we are using an approximation of the Wagner function and not the Wagner function itself. This is confirmed by using Coller's approximation, we can see that the computed lift is closer to this approximation.

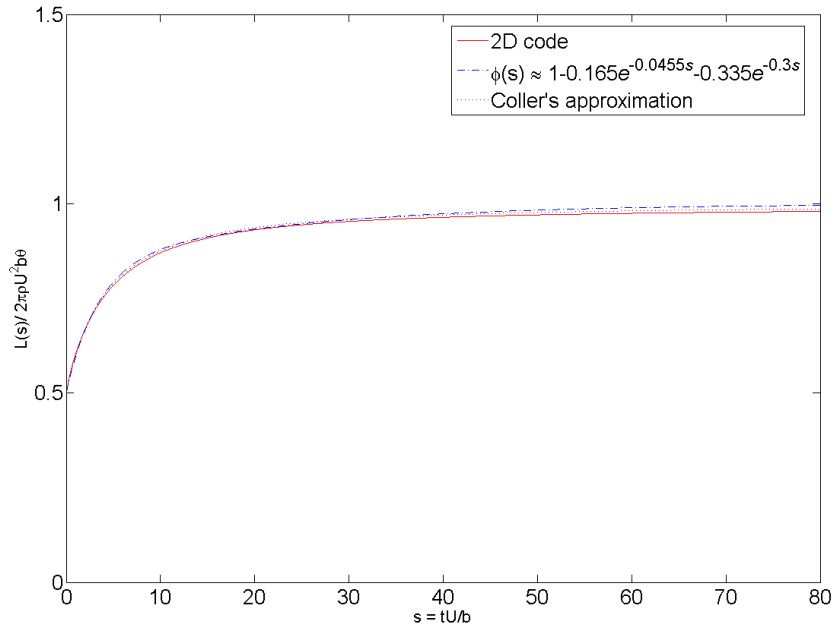

Figure IV.4: Non dimensional lift for a sudden change in pitch.

a.2 Plunging motion

In this section, analytical results of Azuma et al. [47] for the mean coefficient of thrust and power and results of Theodorsen [15] and Garrick [16] for the maximum coefficient of lift for a flat plate in pure plunge will be compare to the results provided by the model presented. Results will be presented in non-dimensional terms:

$$\begin{aligned} C_L &= \frac{L}{\pi\rho b U^2} \\ C_T &= \frac{T}{\pi\rho b U^2} \\ C_P &= \frac{P}{\pi\rho b U^3} \end{aligned} \tag{IV.40}$$

In Table IV.1, I compare the results obtained by the method developed for a pure plunging motion to the analytical results presented earlier for various reduced frequencies (k). NTS represents the number of time steps per flapping cycle. The percentage in the table represents the relative error of the present method compare to the analytical results. The calculation is run for six cycles, the aerodynamic coefficients are computed over the last cycle. After five cycles convergence is reached.

k	N	NTS	$\langle C_P \rangle$	$\langle C_T \rangle$	$C_{L_{peak}}$
0.39	25	50	0.34%	-2.04%	0.03%
0.39	25	100	-1.01%	-2.22%	-1.10%
0.39	25	200	-1.62%	-2.16%	-1.67%
0.39	50	50	1.60%	-0.91%	1.31%
0.39	50	100	0.22%	-1.10%	0.16%
0.39	50	200	-0.42%	-1.05%	-0.48%
0.39	100	50	2.22%	-0.37%	1.94%
0.39	100	100	0.83%	-0.57%	0.78%
0.39	100	200	0.17%	-0.52%	0.13%
0.79	25	50	2.01%	-3.49%	0.06%
0.79	25	100	-0.25%	-3.47%	-1.60%
0.79	25	200	-1.39%	-3.48%	-2.49%
0.79	50	50	3.67%	-1.72%	1.79%
0.79	50	100	1.30%	-1.63%	0.13%
0.79	50	200	0.13%	-1.63%	-0.77%
0.79	100	50	4.46%	-0.89%	2.66%
0.79	100	100	2.07%	-0.76%	1.00%
0.79	100	200	0.86%	-0.77%	0.09%
1.57	25	50	5.20%	-6.11%	-1.83%
1.57	25	100	1.37%	-6.35%	-3.13%
1.57	25	200	-0.91%	-6.44%	-3.72%
1.57	50	50	7.52%	-2.61%	0.17%
1.57	50	100	3.62%	-2.91%	-1.07%
1.57	50	200	1.26%	-2.95%	-1.64%
1.57	100	50	8.64%	-0.98%	1.21%
1.57	100	100	4.67%	-1.32%	-0.01%
1.57	100	200	1.86%	-1.34%	-0.56%
3.14	25	50	12.81%	-11.51%	-3.13%
3.14	25	100	3.29%	-12.21%	-3.55%
3.14	25	200	-0.49%	-12.37%	-3.83%
3.14	50	50	16.59%	-5.41%	-1.35%
3.14	50	100	7.04%	-5.60%	-1.76%
3.14	50	200	3.07%	-5.68%	-1.99%
3.14	100	50	18.36%	-2.55%	-0.36%
3.14	100	100	9.27%	-2.53%	-0.72%
3.14	100	200	4.66%	-2.56%	-0.94%

Table IV.1: Error for the mean coefficient of thrust, power and peak lift coefficient obtained by the present two-dimensional method compared to the results of Theodorsen [15] and Garrick [16] for a pure plunging motion.

k	N	NTS	$\langle C_P \rangle$	$C_{P_{peak}}$
3.14	50	100	7.04%	-1.76%
3.14	50	200	3.07%	-2.27%
3.14	100	50	18.36%	-0.38%
3.14	100	100	9.27%	-0.92%
3.14	100	200	4.66%	-1.29%

Table IV.2: Error for the mean coefficient of power and its peak obtained by the present two-dimensional method compared to the results of Theodorsen [15] and Garrick [16] for a pure plunging motion.

We can see in Table IV.1 that increasing the number of panels or the number of point per flapping cycle does not necessarily mean decreasing the error. However if we both decrease the time step and increase the number of points on the airfoil, then the error decreases.

It should also be noted that for higher reduced frequencies the error in the mean thrust and especially in the mean power increase. This can be explained by an issue arising when a time varying quantity $f(t) = f_{mean} + f_{ampl} \sin(\varpi t)$ has a mean value small compared to its amplitude. A small error in the approximation of f can translate into a bigger error in the approximation of its mean. To verify this statement, I compared the value of the peak power given by the present method to the value of the peak power found by Theodorsen [15] and Garrick [16].

We can see on Table IV.2 that the error for the peak value of the coefficient of power is effectively small.

a.3 Pitching motion

The same convergence study is performed for a pure pitching motion about the elastic axis of the flat plate (at the quarter chord). These results are shown in Table IV.3. This time, the error on the mean coefficient of thrust is large. The same test to see if it is a problem with the averaging can be conducted.

k	N	NTS	$\langle C_P \rangle$	$\langle C_T \rangle$	$C_{L_{peak}}$
1.57	25	50	-7.59%	-38.95%	-4.31%
1.57	25	100	-9.23%	-31.54%	-5.20%
1.57	25	200	-9.27%	-27.32%	-5.71%
1.57	50	50	-2.27%	-28.41%	-1.32%
1.57	50	100	-1.14%	-20.77%	-2.17%
1.57	50	200	-3.78%	-16.16%	-2.68%
1.57	100	50	0.45%	-23.35%	0.21%
1.57	100	100	-1.14%	-15.49%	-0.64%
1.57	100	200	-1.03%	-10.66%	-1.20%
3.14	25	50	-6.33%	-26.68%	-5.45%
3.14	25	100	-9.29%	-24.21%	-6.16%
3.14	25	200	-10.37%	-22.89%	-3.24%
3.14	50	50	0.41%	-17.23%	-2.24%
3.14	50	100	-2.77%	-13.74%	-2.89%
3.14	50	200	-4.02%	-12.18%	-3.24%
3.14	100	50	3.80%	-12.50%	-0.51%
3.14	100	100	0.49%	-8.53%	-1.11%
3.14	100	200	-0.85%	-6.84%	-1.45%

Table IV.3: Error for the mean coefficient of thrust, power and peak lift coefficient obtained by the present two-dimensional method compared to the results of Theodorsen [15] and Garrick [16] for a pure pitching motion about the elastic axis.

k	N	NTS	$\langle C_T \rangle$	$C_{T_{peak}}$
1.57	25	50	-38.95%	-5.94%
1.57	25	100	-31.54%	-6.26%
1.57	25	200	-27.32%	-6.40%
1.57	50	50	-28.41%	-2.94%
1.57	50	100	-20.77%	-3.02%
1.57	50	200	-16.16%	-3.20%
1.57	100	50	-23.35%	-1.34%
1.57	100	100	-15.49%	-1.33%
1.57	100	200	-10.66%	-1.53%

Table IV.4: Error for the mean coefficient of thrust and its peak obtained by the present two-dimensional method compared to the results of Theodorsen [15] and Garrick [16] for a pure pitching motion about the elastic axis.

We can see in Table IV.4 that the error for the peak coefficient of thrust is smaller. The same phenomenon explained above is happening for the coefficient of thrust.

To conclude, we saw that the present theory gave good agreements with the Theodorsen's theory and the results of Azuma et al. Fifty panels on the airfoil and fifty points per flapping cycle seem to give good results within a reasonable computing time. Further convergence studies will be presented in hovering.

In the next section, I will compare the shape of the wake provided by the present method to experimental results.

b Wake patterns

The study performed in the previous section was based on the linear theory. Consequently, the wake was supposed to be flat or frozen. To test the present theory when the wake is freely convected, I will compare patterns of the wake for various reduced frequencies and Strouhal numbers to the wake computed by Jones et al [9].

In Figure IV.5, Jones et al. plot the wake computed by their panel code on a NACA 0012 airfoil, and below it, the wake they obtained during a water tunel experiment. The water tunel is a closed circuit, continuous flow facility. The flow visualization is obtained by injecting food coloring upstream of the test section.

As we can see by comparing Figure IV.5 and Figure IV.6, the present model agrees well with both the method of Jones and the water tunnel experiment. Even though the method presented uses a flat plate while Jones et al. use a NACA 0012, the results are similar because the NACA 0012 is a symmetrical airfoil with a thickness relatively small (12 % of the chord). This is also confirmed by Figure IV.7. In Figure IV.7, results computed by Jones et al. are presented on the left and results obtained by the present theory are plotted on the right in the same exact conditions as in Jones et al.

We saw that for small amplitudes the present model agreed with Theodorsen's results. We also saw that the shape of the wake was in good agreement with previous experiments and computational results. We now need to take a closer look at convergence in hovering since the hover condition is of primary interest.

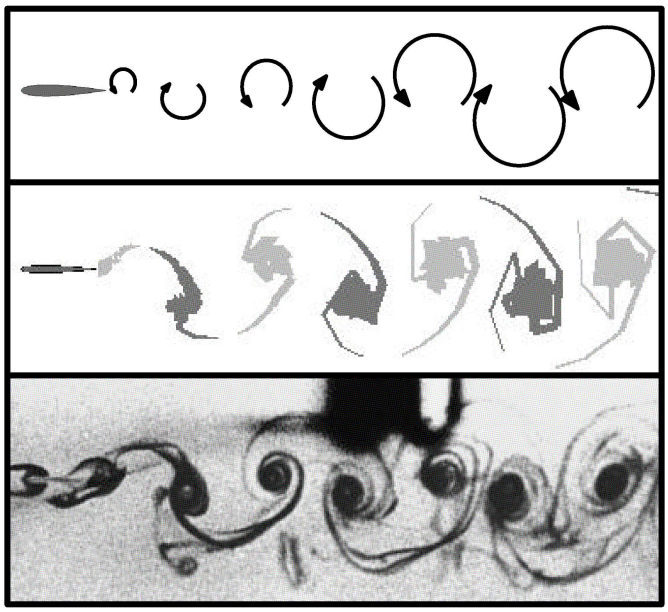

Figure IV.5: Wake pattern for a reduced frequency $k = \frac{\varpi c}{U} = 3.0$ and a plunging amplitude $h = 0.2$ obtained by Jones et al. [9].

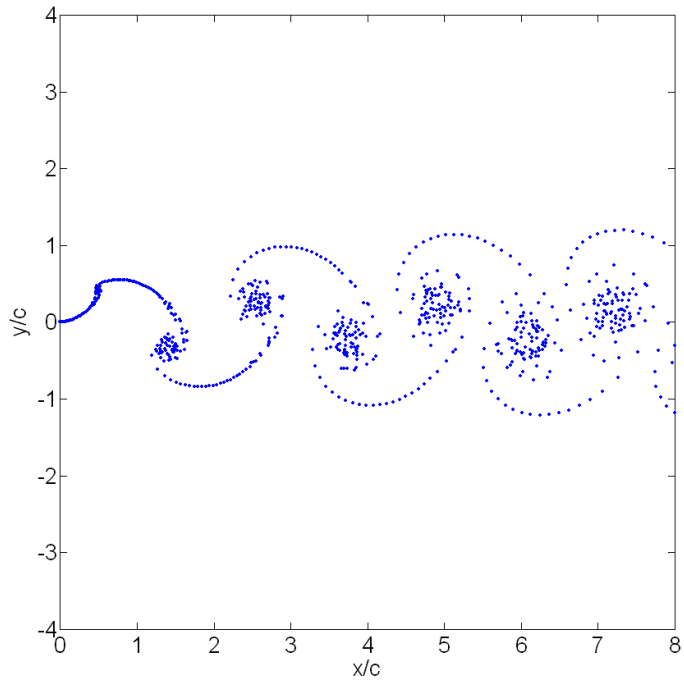

Figure IV.6: Wake pattern for a reduced frequency $k = \frac{\varpi c}{U} = 3.0$ and a plunging amplitude $h = 0.2$ obtained with the present method.

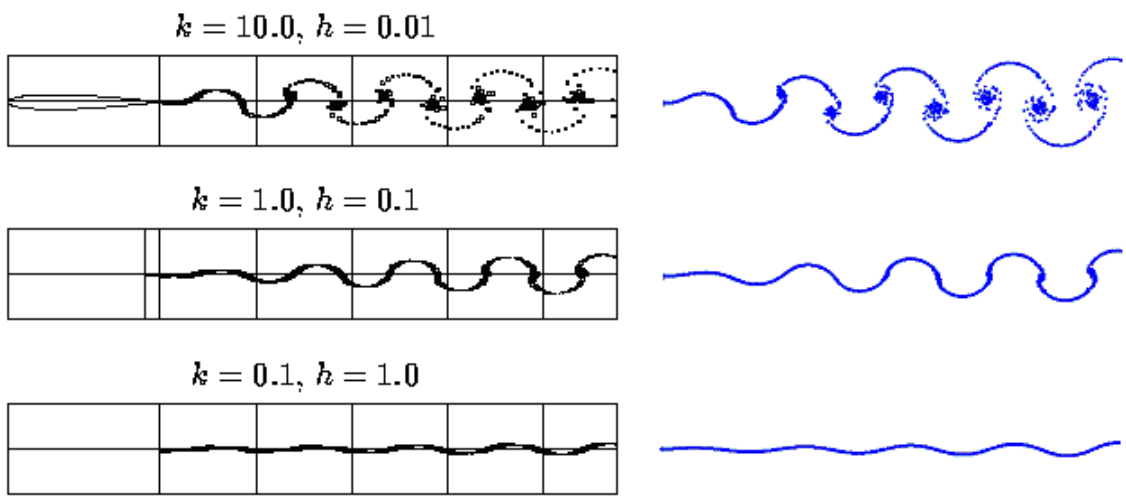

Figure IV.7: Wake patterns obtained by Platzer et al. [10] on the left side for various reduced frequencies $k = \frac{\varpi c}{U}$; wake patterns for the same conditions obtained with the present method on the right side.

c Large amplitude in hover

In hover, the freestream velocity becomes zero. Practically, the present method starts with some small inflow (U_{start}) and after a few iterations ($IT_{U_{start}}$), this freestream is turned off. During the first iterations, the reduced frequency k_{start} has a finite value. With this method, the wake is initially convected downstream which removes any singularity that could arise if we started directly without any freestream. I will study the influence of the number of panels on the airfoil, the starting inflow, the number of iterations with the freestream on and the number of cycles needed to reach convergence in the mean aerodynamics forces and power. This study is conducted on a flat plate with a chord c in pure plunging motion at $50Hz$ with an amplitude of plunge of $1.08c$. The choice of the flapping frequency is arbitrary since everything scales like the frequency squared or cubed.

c.1 Number of cycles

To find the number of cycles needed to reach convergence, I run different configurations and plot the mean coefficients of thrust and power. In hover, these coefficients are defined

as

$$C_T = \frac{T}{\rho c^3 \varpi^2}$$
$$C_P = \frac{P}{\rho c^4 \varpi^3} \tag{IV.41}$$

In Table IV.5, $\langle C \rangle$ represents the mean of the aerodynamic coefficients taken over 10 cycles (cycles 10 to 19, or cycles 20 to 29). In addition, to study the convergence in time of the solution, a ten entry vector composed of the means over one cycle for cycles 10 to 19 or cycles 20 to 29 is computed. $\sigma \langle C \rangle$ represents the standard deviation of this vector. First, by looking at Table IV.5, we can notice that the standard deviation of the averaged coefficients is low if we either average over 10 cycles starting at cycle 10 or starting at cycle 20. This shows that the mean coefficients converge. One interesting behavior that is also confirmed by looking at Figure IV.8 is the fact that the standard deviation for the mean power coefficient is almost always lower than the one for the mean thrust coefficient. In pure plunge, the aerodynamic power comes almost entirely from the lift since the thrust is perpendicular to the motion of the plate. We saw earlier that the present method gave better predictions for the lift than for the averaged thrust (because of averaging issues discussed above). Consequently, this could explain the difference between the two standard deviations. Finally by looking at Figure IV.8 and Figure IV.9, the convergence is confirmed. We can see that the averaged coefficients over one cycle are almost constant. Discrepancies are observed for the curves $N = 100$, $NTS = 100$ for the mean thrust coefficient. It seems that more cycles are needed to reach convergence. However, the curves seem to converge to the same value as the other curves.

Another interesting behavior observed from Figure IV.8 and Figure IV.9 is the fact that the coefficeints are not exactly constant. This can be explained by the non-linearity of the problem which does not guarantee a perfectly periodic solution. In addition, by looking at the shape of the wake, we notice that it is also not purely periodic which confirms why the coefficients are not constant.

We looked at the influence of the number of cycles computed, we will now study the influence of the number of iterations with nonzero freestream. As mentionned earlier, to avoid singular solutions, during the first few iterations the freestream velocity is nonzero.

N	NTS	Nb cycles	Averaging	k_{start}	$IT_{U_{start}}$	$\langle C_T \rangle$	$\langle C_P \rangle$	$\sigma \langle C_T \rangle$	$\sigma \langle C_P \rangle$
50	50	30	10 - 19	3.93	10	0.9147	0.8693	0.64%	0.14%
50	50	30	20 - 29	3.93	10	0.9286	0.8745	0.59%	0.30%
50	50	30	10 - 19	3.93	5	0.9304	0.8711	0.63%	0.16%
50	50	30	20 - 29	3.93	5	0.9346	0.8742	0.69%	0.11%
50	100	30	10 - 19	3.93	20	0.9279	0.8554	0.27%	0.27%
50	100	30	20 - 29	3.93	20	0.9180	0.8635	1.63%	0.21%
50	100	30	10 - 19	3.93	10	0.9173	0.8556	1.27%	0.34%
50	100	30	20 - 29	3.93	10	0.9328	0.8635	1.73%	0.53%
100	50	30	10 - 19	3.93	10	0.9312	0.8823	0.75%	0.18%
100	50	30	20 - 29	3.93	10	0.9260	0.8839	0.57%	0.18%
100	50	30	10 - 19	3.93	5	0.9158	0.8829	0.60%	0.23%
100	50	30	20 - 29	3.93	5	0.9269	0.8853	0.32%	0.14%
100	100	30	10 - 19	3.93	20	0.9557	0.8641	1.36%	1.47%
100	100	30	20 - 29	3.93	20	0.9467	0.8766	0.68%	0.33%
100	100	30	10 - 19	3.93	10	1.0204	0.8798	1.19%	0.29%
100	100	30	20 - 29	3.93	10	0.9701	0.8786	1.53%	0.15%

Table IV.5: Averaged mean coefficients of thrust and power taken over cycles 10 to 19 or 20 to 29 and their standard deviations.

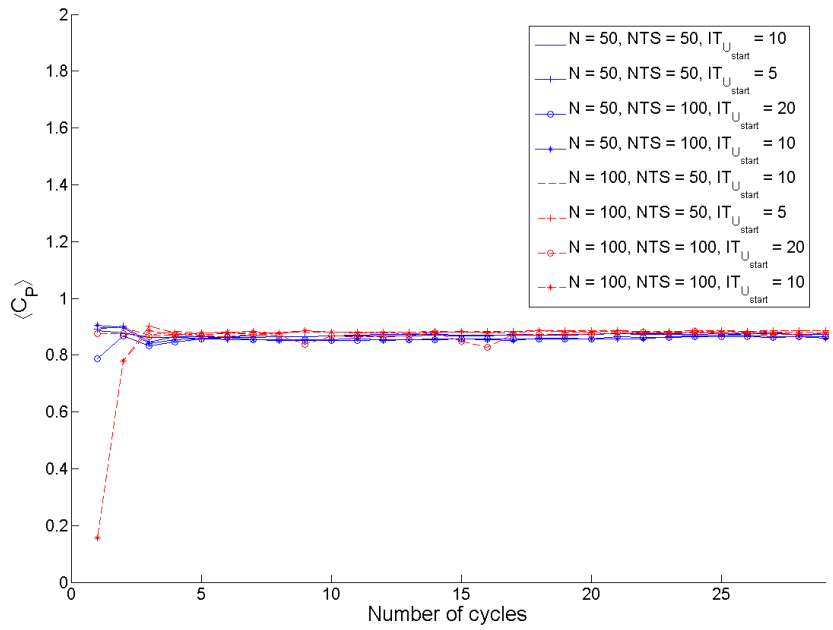

Figure IV.8: Mean coefficient of power taken over one cycle as a function of the number of cycles elapsed.

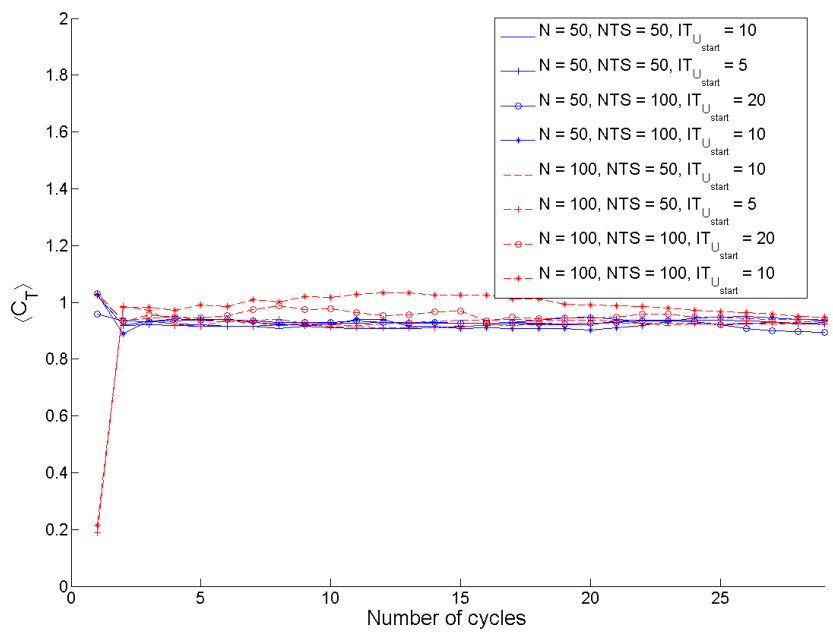

Figure IV.9: Mean coefficient of thrust taken over one cycle as a function of the number of cycles elapsed.

c.2 Number of iterations with the freestream on

In this section, we look at the influence of the number of iterations with nonzero freestream. To study the impact on the converged solution, the freestream is nonzero during five or ten iterations when $NTS = 50$ or for ten or twenty iterations when $NTS = 100$. We can see on Table IV.5 that the number of iterations during which the freestream is on does not influence by a significant amount the value of the converged coefficients. Nevertheless, it seems that when this number of iterations is smaller, the standard deviation on the mean coefficients is smaller. In addition, having a smaller number of iterations with an inflow makes more physical sense. The influence of this inflow will be less than if it is left on for a longer period of time.

c.3 Number of panels

To check the convergence with the number of panels, I look at the relative change of averaged mean coefficients for an increase in number of panels. As noted above, we need to wait for more than 25 flapping cycles in the case of $N = 100$, $NTS = 100$. Thus, in this case I will use an averaging over 25 - 29 flapping cycles. As seen on Table IV.6, the relative change is small and fifty panels over the airfoil seems a reasonable number.

N	NTS	$IT_{U_{start}}$	$\langle C_T \rangle$	$\langle C_P \rangle$	$\sigma \langle C_T \rangle$	$\sigma \langle C_P \rangle$	Relative change $\langle C_T \rangle$	Relative change $\langle C_P \rangle$
25	50	5	0.9136	0.8507	0.26%	0.06%		
50	50	5	0.9301	0.8745	0.57%	0.16%	-1.81%	-2.80%
100	50	5	0.9277	0.8852	0.45%	0.19%	0.26%	-1.22%
25	100	10	0.9409	0.8654	0.87%	0.43%		
50	100	10	0.9446	0.8661	0.52%	0.37%	-0.39%	-0.08%
100	100	10	0.9573	0.8795	0.84%	0.15%	-1.34%	-1.55%

Table IV.6: Averaged mean coefficients of thrust and power taken over cycles 25 to 29, their standard deviations and their relative change due to an increase in number of panels.

c.4 Number of points per cycle

Another important parameter that needs to be studied is the number of points per flapping cycle. I use fifty panels on the airfoil. The relative change is taken as being the change in mean values for a decrease in time step. Table IV.7 shows that the relative change is small for an increase in number of points per cycle. In addition, the computing time scales like NTS^2, consequently fifty points per cycle seems to be a good choice.

NTS	Averaging	$IT_{U_{start}}$	$\langle C_T \rangle$	$\langle C_P \rangle$	$\sigma \langle C_T \rangle$	$\sigma \langle C_P \rangle$	Relative change $\langle C_T \rangle$	Relative change $\langle C_P \rangle$
50	10 - 19	5	0.9304	0.8711	0.63%	0.16%		
50	20 - 29	5	0.9346	0.8742	0.69%	0.11%		
100	10 - 19	10	0.9173	0.8556	1.27%	0.34%	-1.41%	-1.78%
100	20 - 29	10	0.9328	0.8635	1.73%	0.53%	-0.19%	-1.22%

Table IV.7: Averaged mean coefficients of thrust and power taken over cycles 10 to 19 or 20 to 29 with $N = 50$, their standard deviations and their relative change due to a decrease in time step.

c.5 Freestream velocity

To avoid singularity at the beginning of the computation, the present method uses a nonzero freestream over the first few iterations. In this section, we study the influence of the value of the freestream velocity. Having a nonzero velocity is equivalent to having a finite reduced frequency (k_{start}). As seen on Table IV.8, the value of the finite reduced frequency used does not influence a lot the converged values of the mean coefficients of thrust and power. In the present method, a value of $k_{start} = 3.93$ will be used.

k_{start}	$IT_{U_{start}}$	$\langle C_T \rangle$	$\langle C_P \rangle$	$\sigma \langle C_T \rangle$	$\sigma \langle C_P \rangle$	Relative change $\langle C_T \rangle$	Relative change $\langle C_P \rangle$
3.93	5	0.9304	0.8711	0.63%	0.16%		
7.85	5	0.9413	0.8571	1.30%	0.69%	-1.17%	1.61%

Table IV.8: Averaged mean coefficients of thrust and power taken over cycles 10 to 19 with $N = 50$, $NTS = 50$, their standard deviations and their relative change due to an increase in k_{start}.

c.6 Conclusion

To conclude, in the simulations, the following parameters will be used, $N = 50$, $NTS = 50$, $k_{start} = 3.93$, $IT_{U_{start}} = 5$ and averaging over flapping cycles 10 -19.

IV.4 Results

The goal is to find the optimal motion of the flat plate. In other words, for a required thrust, a fixed plunging amplitude, what the phase shift and the pitch angle need to be to minimize the required power.

We also wanted to be able to compare the results of the present method to the results of the previous chapter using Hall's method. Thus we choose to use a flat plate of chord c pitching about the axis $0.2c$ from the leading edge. In addition, the plunge amplitude was taken as the plunge amplitude of the three-quarter span cross section of a rectangular

wing of aspect ratio $AR = 3$ flapping with a stroke angle of 150°. The choice of using the three-quarter span location is motivated by the fact that more thrust is generated at the tip of the wing because the velocity is higher than at the root. Consequently, the plunge amplitude is

$$\frac{h}{c} = \frac{3}{8} AR \sin\left(\frac{75\pi}{180}\right) \tag{IV.42}$$

The total thrust is simply the thrust produced by the flat plate times the total span. Since the goal is the find the optimum power for a prescribed thrust, we would have to search for each motion through the frequency domain to get the frequency that gives the thrust required. This process would be time consuming. Instead, we can use the non-dimensional analysis of section I.2. In the inviscid case, for a given kinematics at a flapping frequency f, the present method provides the inviscid power P and the thrust generated T. One can deduce the frequency f_{req} at which the plate should flap to get the required thrust T_{req} by the expression

$$f_{req} = f\sqrt{\frac{T_{req}}{T}} \tag{IV.43}$$

Consequently, the inviscid power becomes

$$P_{req} = P\left(\frac{f_{req}}{f}\right)^3 \tag{IV.44}$$

For the viscous cases, the process is similar but requires an iterative method. By adding the corrective term $\vec{F}_{viscous} = \frac{1}{2}\rho U^2 c C_D \frac{\vec{U}}{\|\vec{U}\|}$, the thrust is modified and since the viscous force depends on the flapping frequency, a simple scaling does not work. I wrote a Matlab routine that post processes the results of my simulations. This routine follows these steps:

1. Pick an initial falpping frequency.
2. Compute the viscous force.
3. Scale the induced thrust and power using Equation IV.43 and IV.44.
4. Compute the new total thrust and total power.
5. Go back to step 1 and change the initial picked frequency until the thrust of step 4 is equal to T_{req}.

We can also introduce a figure of merit (FOM) to compare the efficiency to the efficiency provided by the actuator disk theory. The FOM is defined as

$$\begin{aligned} FOM &= \left(\frac{P}{T^{3/2}}\right)_{Actuator} \Big/ \left(\frac{P}{T^{3/2}}\right) \\ FOM &= \frac{1}{\frac{P}{T^{3/2}}\sqrt{2\rho A}} \end{aligned} \tag{IV.45}$$

where A is the area covered by the flapping wing. In our case, $\frac{A}{c^2} = \pi \frac{AR^2}{4} \frac{150}{180}$

IV.4.1 Inviscid case

In this section, I will present the results provided by the present method for the inviscid case. The goal is to find the optimum motion for a required thrust by modifying the pitch angle and the phase shift. We will use surface plots of the figure of merit to identify the optimum motion. In addition, a corresponding surface plot of the non-dimensional frequency $\tilde{f} = f \frac{2\pi}{\sqrt{\frac{T}{\rho c^3}}}$ will also be presented. We can see in Figure IV.10 that the maximum FOM has a value of 0.74 and is obtained for a phase shift of $\frac{\pi}{2}$ and a pitch angle of 35°. By looking at Figure IV.11, we get the corresponding non-dimensional frequency of 1.10. For this motion, the coefficient of thrust is $C_T = \frac{T}{\rho c^3 \varpi^2} = 0.835$ and the coefficient of aerodynamic power is $C_P = \frac{P}{\rho c^4 \varpi^3} = 0.523$.

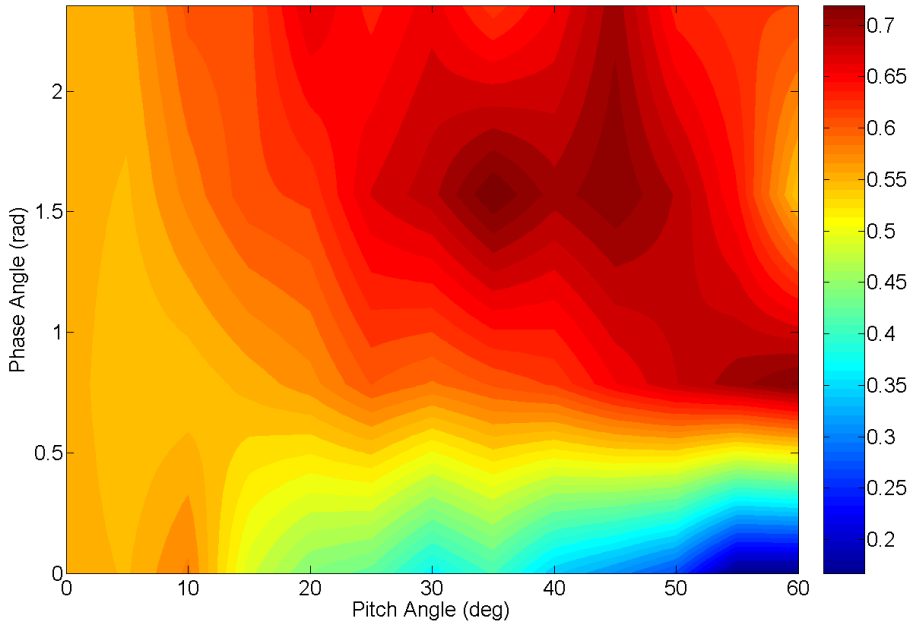

Figure IV.10: *FOM* for a required coefficient of thrust function of the pitch angle and the pitch phase advance in the inviscid case.

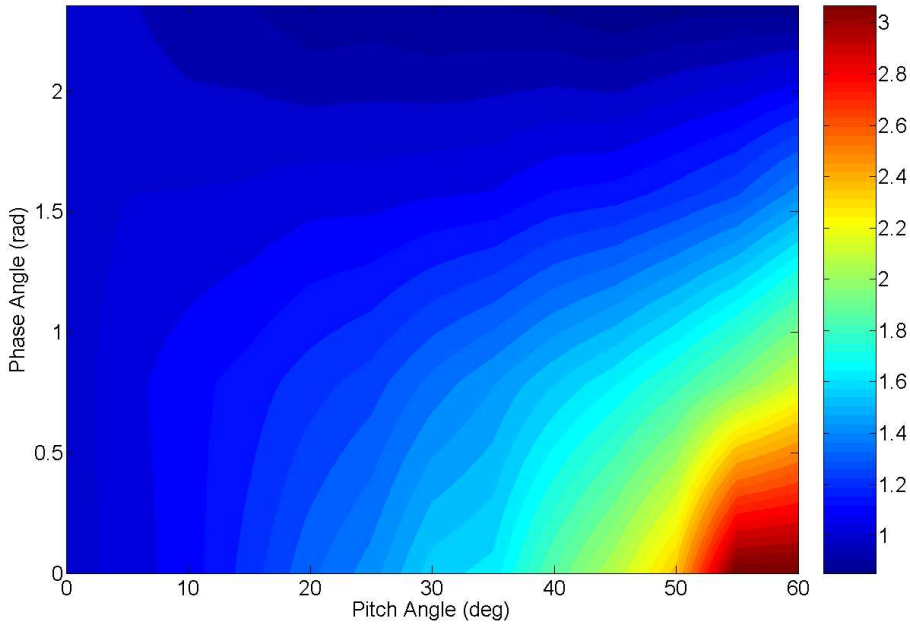

Figure IV.11: Non-dimensional flapping frequency ($\tilde{f}$) for a required coefficient of thrust function of the pitch angle and the pitch phase advance in the inviscid case.

We also wanted to compare these results to the results obtained with the optimizer of Chapter III. Initially, Hall's method was implemented for flapping wings and not plunging wings. To compare his results to a two-dimensional plunging and pitching plate, we modified the method to incorporate a plunging and pitching motion. A wing of aspect ratio $AR = 3$ undergoing plunging and pitching motions was used in Hall's method. The exact same non-dimensional frequency, amplitude of plunge, pitch and phase angle as the optimum provided by the present method were used. We also removed the constraint on the maximum coefficient of lift in Hall's method since this one does not exist in the present method. For that configuration, we obtained with Hall's method a coefficient of power of 0.573 and a FOM of 0.67. The fact that the figure of merit provided by Hall's method is lower than in the present method might be explained by the three-dimensional effects that are not captured in the two-dimensional method (tip losses). Thus, the aspect ratio was increased by a factor of 10 in Hall's method. The figure of merit as expected increased to a value of 0.79 which is closer to the value of 0.74 found using the present theory. This result shows the importance of the three-dimensional effects and the good agreement between the two methods.

To conclude, we saw the existence of an optimum motion in the inviscid case in two-dimensions. In addition, there is a surprisingly good agreement for the value of the figure of merit between the present method and Hall's theory. In the following section, we will look at the impact of the viscous corrective term.

IV.4.2 Viscous model 1

In this section, the viscous corrective term is now added. The viscous formulation was introduced in section IV.3.2 b. The viscous force and power are computed by using Equation IV.30. Consequently, we need to introduce a drag polar model. The first viscous

model uses the drag polar model of Equation III.32 and plotted in Figure IV.12,

$$C_d = \begin{cases} f\left(C_l\right) \text{ if } f\left(C_l\right) \succ \frac{3.45}{\sqrt{Re_c}} \\ \frac{3.45}{\sqrt{Re_c}} \text{ otherwise} \end{cases} \tag{IV.46}$$

$$f\left(x\right) = -0.4236x^6 + 3.2787x^5 - 9.1871x^4 + 12.525x^3 - 8.9124x^2 + 3.5218x^1 - 0.4635$$

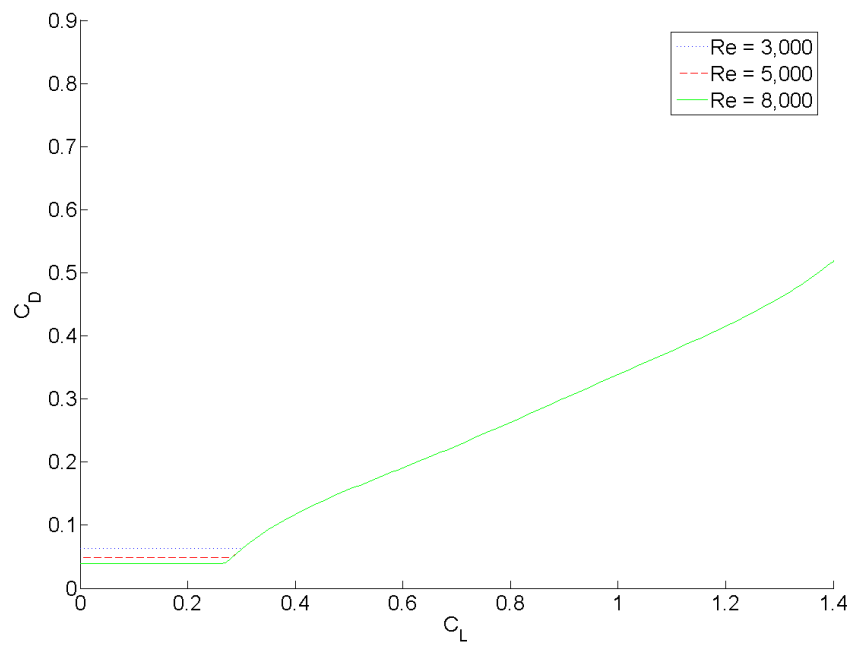

Figure IV.12: Drag polar of Equation IV.46 for three Reynolds numbers (3,000, 5,000, 8,000).

The kinematics and geometrical conditions are the same as in the inviscid case. The point where the velocity of Equation IV.30 is computed is located at a distance of a half chord behind the axis of rotation of the plate. The choice of this location is somewhat arbitrary but reflects an averaged velocity seen by the plate. As noticed in Figure IV.13, the FOM has decreased compared to the FOM in the inviscid case. The optimal figure of merit is now 0.61 which is a 17% decrease compared to the optimal figure of merit in the inviscid case. This order of magnitude is in agreement with the findings of Wells [27]. He showed that the viscous power was lower than the induced power by a factor of 3.5. Even though the power required increased, the optimal motion stays almost the same. The pitch

phase advance remains $\frac{\pi}{2}$ and the pitch angle is now 45°. The non-dimensional flapping frequency required to generate the thrust is a little increased to 1.21.

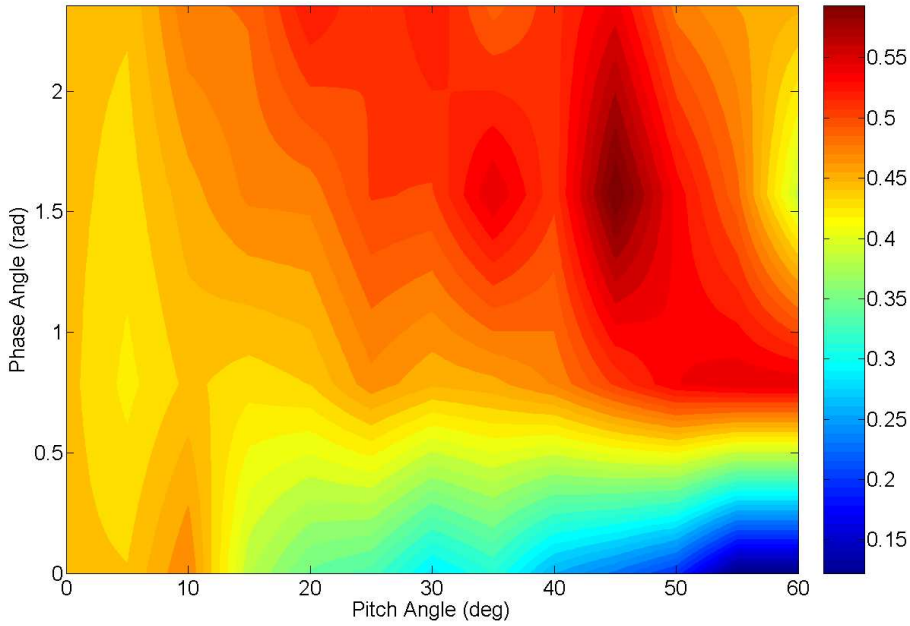

Figure IV.13: *FOM* for a required coefficient of thrust function of the pitch angle and the pitch phase advance in the viscous 1 case.

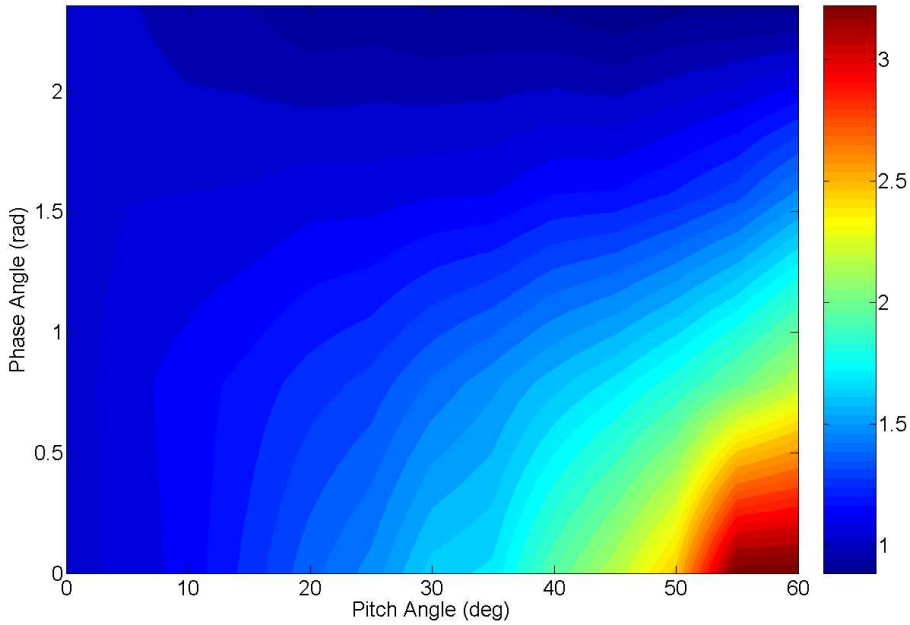

Figure IV.14: Non-dimensional flapping frequency ($\tilde{f}$) for a required coefficient of thrust function of the pitch angle and the pitch phase advance in the viscous 1 case.

IV.4.3 Viscous model 2

This model is based on the results found by Weis-Fogh [32]. He studied 30 different flappers in hovering flight (bats, butterflies, birds, beetles, bees, flies and mosquitoes). Part of his study was to compute their mean drag coefficients. Among those flappers, we look for one that has similar characteristics as the wing we are modeling. For example on a beetle (*H.* sp.) with an elliptical wing of span of $7.7cm$, chord of $2.7cm$, a stroke angle of $180°$, a flapping frequency of $41Hz$ and a thrust generated of $12.8g$; Weis-Fogh found a drag coefficient of 0.07. However, we can notice that for animals with a shorter wing span, this drag coefficient increases. For example for lighter butterflies that have a smaller wingspan, the drag coefficient is 0.17-0.18. Consequently, we choose an average between the two coefficients, 0.12.

The surface plots for the figure of merit and non-dimensional frequency function of the pitch angle and phase shift are presented in Figure IV.15 and Figure IV.16. We can notice from Figure IV.15, that the figure of merit is lower than in the inviscid case. The optimum ($FOM = 0.66$) is obtained for a phase angle of $\frac{\pi}{2}$ and a pitch angle of $35°$, which is exactly the same motion as the optimum motion for the inviscid case. The non-dimensional flapping frequency is slightly increased to 1.12 from 1.10 in the inviscid case.

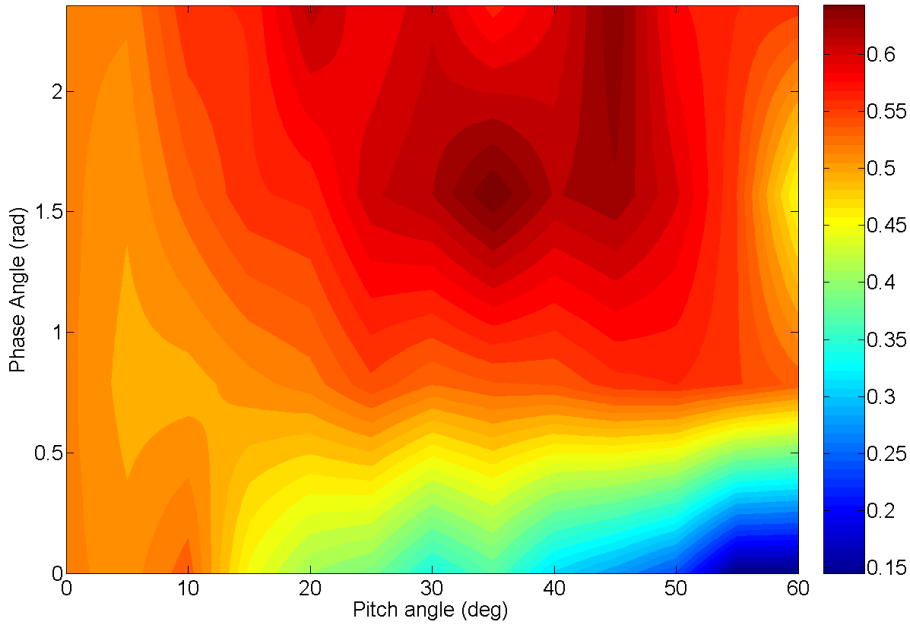

Figure IV.15: *FOM* for a required coefficient of thrust function of the pitch angle and the pitch phase advance in the viscous 2 case.

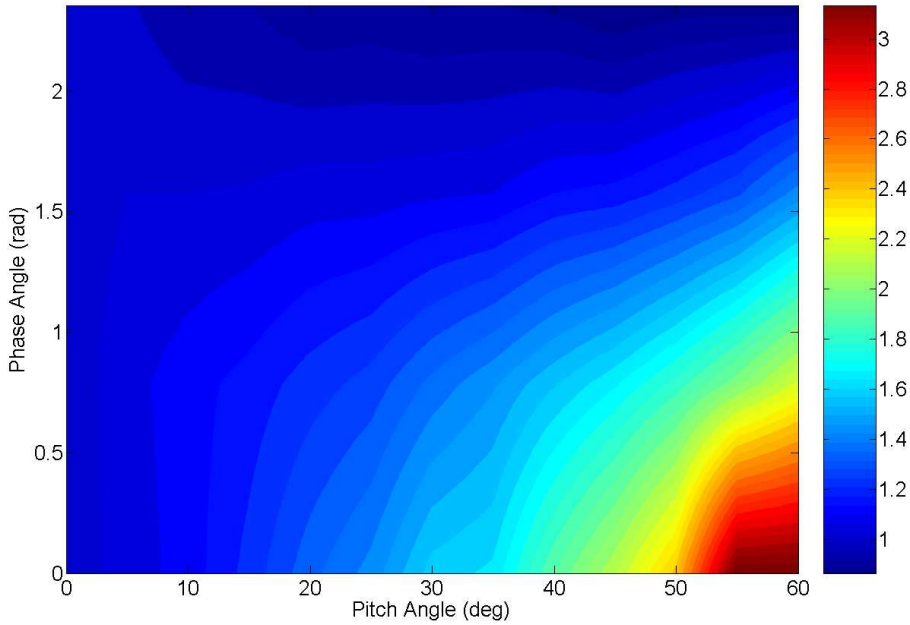

Figure IV.16: Non-dimensional flapping frequency ($\tilde{f}$) for a required coefficient of thrust function of the pitch angle and the pitch phase advance in the viscous 2 case.

In conclusion, we saw that adding viscous forces lowers the figure of merit as expected. Nevertheless, the optimum motion is little changed to unchanged compared to the optimum motion in the inviscid case. This behavior reflects what Hamdani et al. [7] observed. They found that for large accelerated flows, the viscous effects had a limited influence on the aerodynamic coefficients. In a large accelerated flow, which is the case in our simulation, inviscid effects dominate.

However, these viscous models do not take into account the unsteadiness of the flow. They are empirical models and cannot capture the importance of the leading edge vortex and the dynamic stall observed in many flappers during hovering flight.

In addition, the three-dimensional effect is not captured in these simulations. Three-dimensional effects become especially important for low aspect ratio wings, which is the case for many small scale flappers. Thus, the use of a three-dimensional unsteady model would improve the quality of the solution. The development of such a model will be presented in the next chapter.

Chapter V

Three-Dimensional Potential Method

V.1 Problem description

In our study, we are interested in modeling flapping flight, especially in hovering mode. In the previous chapter we presented a two-dimensional model of flapping. Although the two-dimensional model gives qualitative estimate of the optimum motion, we cannot neglect the three-dimensional effects, particularly for low aspect ratio wings. In this chapter I will present a three-dimensional method for computing the aerodynamics of flapping.

V.2 Literature review

Three-dimensional methods for computing unsteady potential flows have been widely used in the literature. They are mainly based on the panel methods developed for example by Hess and Smith [73]. Nevertheless, modeling hovering using these methods remain challenging. More recently, Willis et al. [11] used a panel method consisting of constant strength sources and doublets distributed over lifting surfaces with vortex particles in the wake. They used their method to model the forward flapping flight of bats. However, their assumptions were based on a quasi-steady Kutta condition that are not valid in hovering flight. In the following section, I present a model of hover based on the approach of Willis et al. with modifications required for hover.

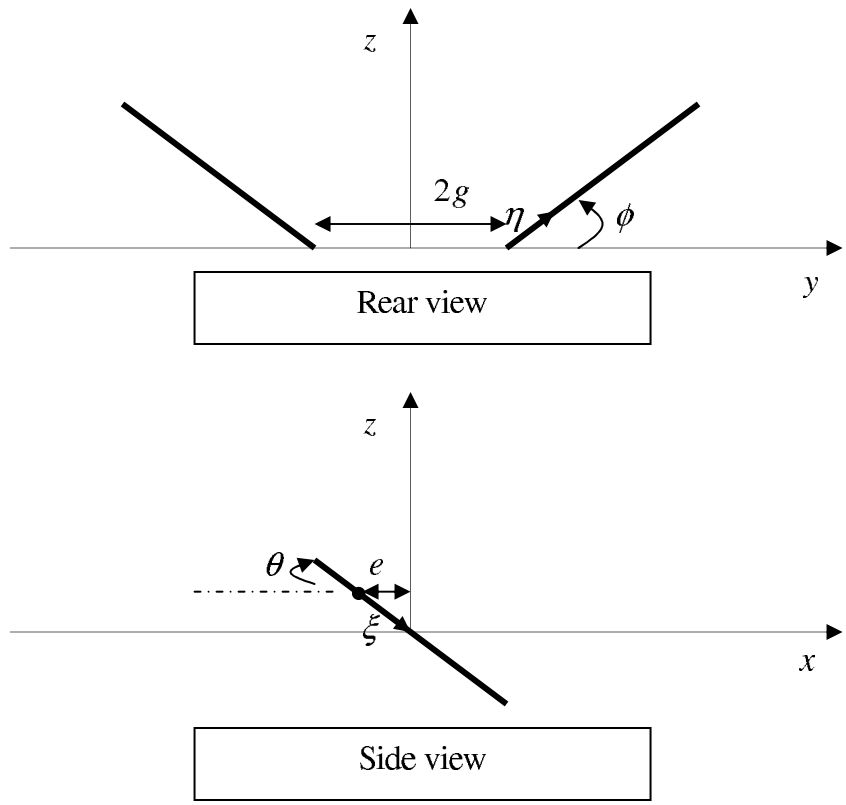

Figure V.1: Schema of the wing.

V.3 Approach

V.3.1 Kinematics

The wing model used comprised of two rigid rectangular flapping wings (with zero thickness). We assume that the two wings are flapping symmetrically about their respective root chords (separated by a gap of $2g$). Consequently, we only need to compute the vorticity on half of the domain and obtain the other half by symmetry.

For the kinematics, we use two degrees of freedom: stroke angle (ϕ) and pitch angle (θ) about an axis perpendicular to the chord root and aligned with the leading edge at the

location e along the x axis (see Figure V.1). The motion can be summarized as followed,

$$\begin{aligned}
&\phi = \sum_{i=1}^{N_m} \phi_n \sin(\varpi_n t) \\
&\theta = \sum_{i=1}^{N_m} \theta_n \sin(\varpi_n t + \phi_n) \\
&\begin{Bmatrix} x-e \\ y-g \\ z \end{Bmatrix} = \begin{bmatrix} 1 & 0 & 0 \\ 0 & \cos(\phi) & \sin(\phi) \\ 0 & \sin(\phi) & -\cos(\phi) \end{bmatrix} \begin{bmatrix} \cos(\theta) & 0 & -\sin(\theta) \\ 0 & 1 & 0 \\ \sin(\theta) & 0 & \cos(\theta) \end{bmatrix} \begin{Bmatrix} \xi \\ \eta \\ 0 \end{Bmatrix}
\end{aligned} \tag{V.1}$$

where N_m is the number of Fourier modes used to describe the wing motion. (ξ, η) is the coordinate system associated with the wing. The origin of the system is located on the root chord on the axis of rotation, the axis ξ is aligned with the chord and the axis η is perpendicular to the root chord and in the wing plane. The motion of the wing is a combinaison of flapping and pitching with a phase difference of ϕ_n.

V.3.2 Potential method

Having presented the type of wing kinematics we want to model, I will explain the development of the presented theory. The method chosen is based on a three-dimensional panel method with free vortons in the wake [11]. I will first review the derivation of the fundamental equations. I will then show how the governing equations are discretized.

a Inviscid formulation

The wing is divided into vortex rings (equivalent to constant strength doublet panels) and a vorton method is used to model the vorticity in the wake. I will first present the governing equations.

a.1 Governing equations

The flow is assumed to be inviscid, incompressible and has a constant density. It is also assumed to be irrotational except for any vorticity localized in the wake trailing lifting surfaces.

By using Helmholtz decomposition, the fluid velocity ($\vec{U}$) is the superposition of a potential vector ($\nabla\Phi$), a vector potential ($\nabla \times \vec{\Psi}$) and a freestream $\vec{U}_\infty$,

$$\vec{U} = \nabla\Phi + \nabla \times \vec{\Psi} + \vec{U}_\infty \tag{V.2}$$

The potential vector is irrotational and any vorticity comes from the vector potential.

We can now use the conservation equations. First the conservation of mass for a fluid with constant density is simply

$$\nabla \cdot \vec{U} = 0 \tag{V.3}$$

By using Equation V.2 in Equation V.3, we get

$$\nabla \cdot \left(\nabla\Phi + \nabla \times \vec{\Psi}\right) = \nabla \cdot \nabla\Phi = \nabla^2\Phi = 0 \tag{V.4}$$

Equation V.4 is Laplace's equation for the velocity potential scalar Ψ. We can introduce the vorticity field defined as the curl of the velocity field,

$$\vec{\omega} = \nabla \times \vec{U} \tag{V.5}$$

Thus, by using Equation V.2 in EquationV.5, we get

$$\nabla \times \left(\nabla\Phi + \nabla \times \vec{\Psi} + \vec{U}_\infty\right) = \vec{\omega} \tag{V.6}$$

The curl of a gradient of a scalar being zero, Equation V.6 becomes

$$\nabla \times \left(\nabla \times \vec{\Psi}\right) = \vec{\omega} \tag{V.7}$$

By using the vector Laplacian relation, Equation V.7 becomes

$$\nabla \times \left(\nabla \times \vec{\Psi}\right) = \nabla\left(\nabla \cdot \vec{\Psi}\right) - \nabla^2\vec{\Psi} = \vec{\omega} \tag{V.8}$$

Finally, by requiring that the vector potential be solenoidal, we get

$$\nabla^2\vec{\Psi} = -\vec{\omega} \tag{V.9}$$

Equation V.9 is Poisson's equation.

Having used the conservation of mass, we can now derive the conservation of momentum for an inviscid constant density flow,

$$\frac{D\vec{U}}{Dt} = -\nabla\left(\frac{P}{\rho}\right) \tag{V.10}$$

The total derivative of the velocity field can also be expressed as

$$\frac{D\vec{U}}{Dt} = \frac{\partial\vec{U}}{\partial t} + \frac{1}{2}\nabla\left(\vec{U}\cdot\vec{U}\right) + \left(\nabla\times\vec{U}\right)\times\vec{U} \tag{V.11}$$

Thus, Equation V.10 becomes

$$\frac{\partial\vec{U}}{\partial t} + \vec{\omega}\times\vec{U} = -\nabla\left(\frac{P}{\rho} + \frac{1}{2}\vec{U}\cdot\vec{U}\right) \tag{V.12}$$

By taking the curl of Equation V.12, we get

$$\frac{\partial\vec{\omega}}{\partial t} + \nabla\times\left(\vec{\omega}\times\vec{U}\right) = 0 \tag{V.13}$$

Or equivalently,

$$\frac{D\vec{\omega}}{Dt} - \left(\vec{\omega}\cdot\nabla\right)\vec{U} = 0 \tag{V.14}$$

To summarize, we have two equations to solve: Laplace's equation, Equation V.4, and Poisson's equation, Equation V.9. Laplace's equation is solved by using a superposition of elementary solutions (vortex rings) and Poisson's equation is solved using the Biot-Savart Law. To ensure the uniqueness of the solution, we will need boundary conditions. In the following sections, I discuss the solution of Laplace's equation and Poisson's equation.

a.2 Laplace's equation

Laplace's equation ($\nabla^2\Phi = 0$) is solved using integral equations. The general form of the solution in three-dimensions at any point $\vec{r}$ in the domain is

$$\begin{aligned}\Phi\left(\vec{r}\right) = \frac{1}{4\pi}\int\int_{S_b}\Phi\left(\vec{r}'\right)\frac{\partial}{\partial n\left(\vec{r}'\right)}\frac{1}{\|\vec{r}-\vec{r}'\|}dS_b + \\ \frac{1}{4\pi}\int\int_{S_w}\Delta\Phi_{wake}\left(\vec{r}'\right)\frac{\partial}{\partial n\left(\vec{r}'\right)}\frac{1}{\|\vec{r}-\vec{r}'\|}dS_w - \\ \frac{1}{4\pi}\int\int_{S_b}\frac{\partial\Phi}{\partial n\left(\vec{r}'\right)}\left(\vec{r}'\right)\frac{1}{\|\vec{r}-\vec{r}'\|}dS_b\end{aligned} \tag{V.15}$$

where S_b is the surface of the body and S_w the surface of the wake defined using rings (near wake described below). The first two terms represent the doublet or ring terms, while the last term is the source term. In our case, where the wing is modeled as a flat plate, the last term is zero.

The boundary condition applied on the surface of the wing is simply the no-flux boundary condition and can be expressed as,

$$\frac{\partial \Phi}{\partial n\left(\vec{r}'\right)}\left(\vec{r}'\right) = \vec{n}\left(\vec{r}'\right) \cdot \left(\vec{U}_b\left(\vec{r}'\right) - \nabla \times \vec{\Psi} - \vec{U}_\infty\right) \tag{V.16}$$

where $\vec{U}_b\left(\vec{r}'\right)$ is the velocity of the body at the location $\vec{r}'$.

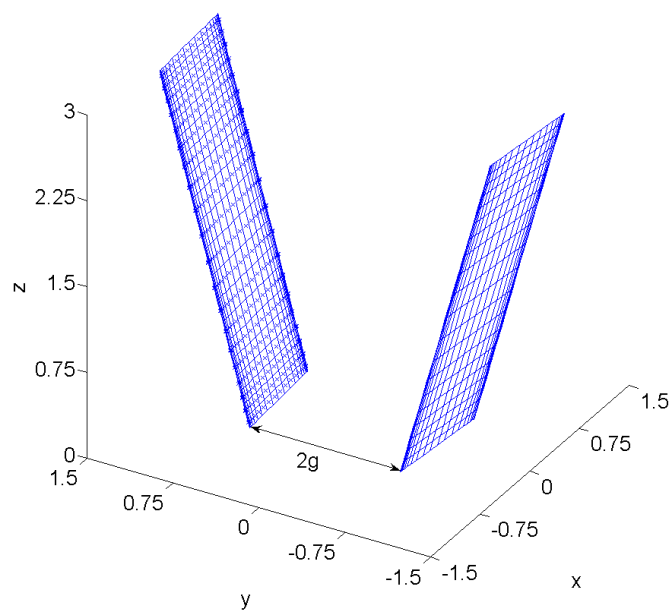

Figure V.2: Discretization of the wings using quadrilateral panels. The crosses are the collocation points.

To solve Laplace's equation, we use a linear superposition of elementary solutions. The wing is discretized using quadrilateral vortex rings (see Figure V.2). The geometric distribution is not uniform. We use more panels near the leading and trailing edge and more panels at the tip and root of the wing than at its center. This discretization is justified by the existence of tip vortices at the root and tip of the wing thus, the gradient of the

circulation is higher at the ends than at the center of the wing. In addition, the gradient of the pressure is also higher at the leading and trailing edges than at the center of the chord. The generic equation we use for the discretization is as followed

$$\begin{cases} dx_i = dx_{i-1}\left(a - b\frac{(i-2)}{0.5N_i-2}\right),\ i = 2,\ldots,0.5N_i \\ dx_i = dx_{N_i-i+1},\ i = 0.5N_i+1,\ldots,N_i \\ a \succ b \end{cases} \\ \begin{cases} dy_j = cdy_{j-1},\ j = 2,\ldots,0.5N_j \\ dy_j = dy_{N_j-j+1},\ j = 0.5N_j+1,\ldots,N_j \end{cases} \tag{V.17}$$

where N_i is the number of panels in the chordwise direction and N_j in the spanwise direction on the half-wing. Thus, $2N_j$ is actually the total number of panels in the spanwise direction over the entire wing. dx_i is the chordwise spacing and dy_j the spanwise spacing. Finally, a, b and c are some constants governing the refinement of the grid we want near the edges.

Now that the wing is discretized into N vortex rings of strength Γ_i, we can evaluate the boundary condition, Equation V.16, at N collocation points, located at the center of each ring. Thus, Equation V.16 can be represented at each time step k as a matrix system,

$$[A]^k (\Gamma)^k = (b)^k \tag{V.18}$$

where, $[A]$ is the matrix of the influence coefficients of the rings at the collocation points. (b) represents $\vec{n}(\vec{r}') \cdot \left(\vec{U}_b(\vec{r}') - \nabla \times \vec{\Psi} - \vec{U}_\infty\right)$ evaluated at the collocation points.

To get the influence coefficients in $[A]$, we use vortex rings over the wing. The influence of a vortex ring is simply the sum of the influence of each vortex line composing the ring. The velocity induced at a point $P(x, y, z)$ by a straight vortex line extending from (x_1, y_1, z_1) to (x_2, y_2, z_2) with a strength of Γ (see Figure V.3) in the x, y, z direction respectively is

$$\begin{aligned} u &= K \cdot (\vec{r}_1 \times \vec{r}_2)_x \\ v &= K \cdot (\vec{r}_1 \times \vec{r}_2)_y \\ w &= K \cdot (\vec{r}_1 \times \vec{r}_2)_z \end{aligned} \tag{V.19}$$

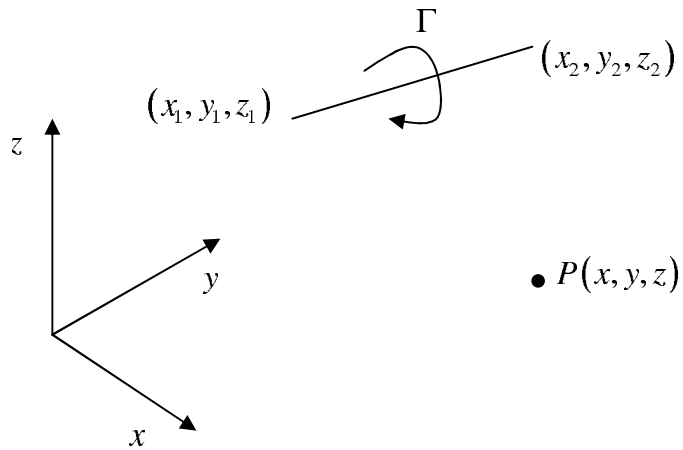

Figure V.3: Influence of a straight vortex line at point $P(x, y, z)$.

with

$$
\begin{aligned}
K &= \frac{\Gamma}{4\pi|\vec{r}_1 \times \vec{r}_2|^2}\left(\frac{\vec{r}_0 \cdot \vec{r}_1}{r_1} - \frac{\vec{r}_0 \cdot \vec{r}_2}{r_2}\right) \\
\vec{r}_i &= \left| \begin{array}{l} x - x_i \\ y - y_i \\ z - z_i \end{array} \right. , i = 1, 2 \\
\vec{r}_0 &= \vec{r}_1 - \vec{r}_2
\end{aligned}
\tag{V.20}
$$

To remove the singularity in K, we introduce a regularization condition. If r_1 or r_2 or $|\vec{r}_1 \times \vec{r}_2|^2$ is less than a small constant ϵ, then K is set to zero.

We are now able to solve Laplace's equation by superposition of vortex rings. To ensure the uniqueness of the solution, the no through flow condition is applied at the center of each ring and provides the strength of each vortex ring. In the next section, I will focus on solving Poisson's equation.

a.3 Poisson's equation

In integral form, the vector potential solution of Poisson's equation, Equation V.9, can be written as

$$
\vec{\Psi}(\vec{r}, t) = \frac{1}{4\pi} \int \int \int_V \frac{\vec{\omega}}{\|\vec{r} - \vec{r}'\|} dV \tag{V.21}
$$

The vorticity in the domain is modeled using a regularized vortex particle method developed by Winckelmans and Leonard [52]. The vorticity in the wake is the summation over the

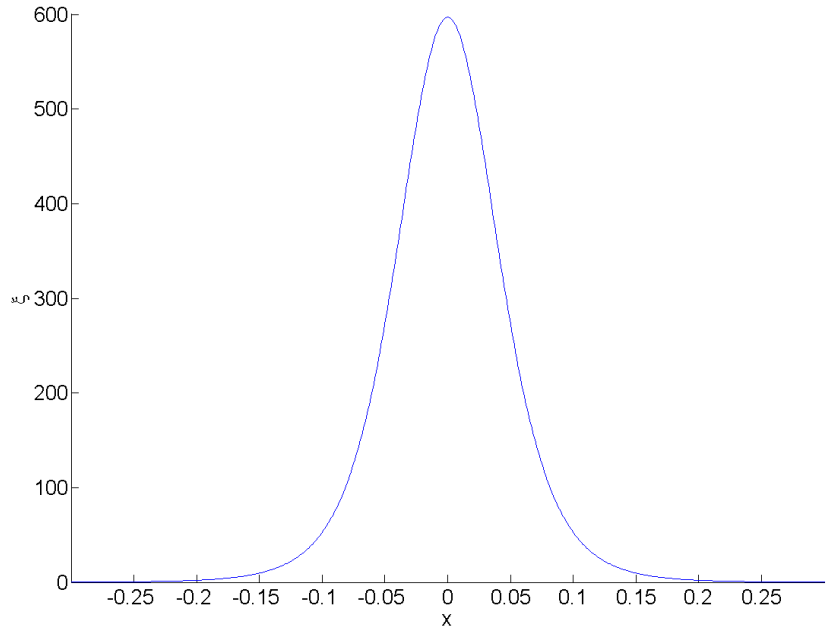

Figure V.4: Regularization function $\xi(x)$ in V.24 with $\sigma = 0.1$.

vorticity of all the particles in the domain,

$$\vec{\omega}_\sigma(\vec{r}, t) = \sum_p \vec{\alpha}^p(t)\, \xi_\sigma(\vec{r} - \vec{r}^p(t)) \tag{V.22}$$

where ξ_σ is a regularization function written as

$$\xi_\sigma(\vec{r}) = \frac{1}{\sigma^3} \xi\left(\frac{\|\vec{r}\|}{\sigma}\right) \tag{V.23}$$

with ξ the following normalized function (Figure V.4):

$$\begin{aligned} &4\pi \int_0^\infty \xi(\rho)\, \rho^2 d\rho = 1 \\ &\xi(\rho) = \tfrac{15}{8\pi} \tfrac{1}{(\rho^2+1)^{7/2}} \end{aligned} \tag{V.24}$$

Consequently by replacing the expression of the vorticity in the domain in Equation V.21, we get

$$\vec{\Psi}_\sigma(\vec{r}, t) = \sum_p \frac{1}{4\pi} \frac{\left(\|\vec{r} - \vec{r}^p(t)\|^2 + \frac{3\sigma^2}{2}\right)}{\left(\|\vec{r} - \vec{r}^p(t)\|^2 + \sigma^2\right)^{3/2}} \vec{\alpha}^p(t) \tag{V.25}$$

Equation V.25 is the solution of Poisson's equation. We will see how to obtain the strength vector $\vec{\alpha}$. We also need to describe the evolution in time of the vortons in the wake. This evolution is characterized by a change of strength and position.

In the Lagrangian representation, the evolution of the position of the particles is the following,

$$\frac{d}{dt}\vec{r}^{p}(t) = \vec{U}\left(\vec{r}^{p}(t), t\right) = \nabla\Phi\left(\vec{r}^{p}(t), t\right) + \nabla \times \vec{\Psi}_{\sigma}\left(\vec{r}^{p}(t), t\right) + \vec{U}_{\infty}(t) \tag{V.26}$$

The first component of Equation V.26 is computing using the induced velocities in the wake by the vortex rings on the wing. The second component is computed by taking the curl of Equation V.25, which can be expressed as

$$\vec{U}_{\sigma}\left(\vec{r}^{p}(t), t\right) = \nabla \times \vec{\Psi}_{\sigma}\left(\vec{r}^{p}(t), t\right) = \sum_{q} \vec{K}_{\sigma}\left(\vec{r}^{p}(t) - \vec{r}^{q}(t)\right) \times \vec{\alpha}^{q}(t) \tag{V.27}$$

with the kernel K_{σ} being

$$\vec{K}_{\sigma}\left(\vec{r}^{p}(t) - \vec{r}^{q}(t)\right) = -\frac{1}{4\pi}\frac{\left(\left\|\vec{r}^{p}(t) - \vec{r}^{q}(t)\right\|^{2} + \frac{5\sigma^{2}}{2}\right)}{\left(\left\|\vec{r}^{p}(t) - \vec{r}^{q}(t)\right\|^{2} + \sigma^{2}\right)^{5/2}}\left(\vec{r}^{p}(t) - \vec{r}^{q}(t)\right) \tag{V.28}$$

After the evolution of the position in time, we can look at the evolution of the particles strength. The particle strength is linked to the vorticity field. Consequently, its evolution is governed by the conservation of momentum derived earlier in Equation V.14. In the Lagrangian approach,

$$\frac{d\vec{\alpha}^{p}(t)}{dt} = \left(\vec{\alpha}^{p}(t) \cdot \nabla\right)\vec{U}\left(\vec{r}^{p}(t), t\right) \tag{V.29}$$

We now need to compute the gradient of the velocity field. The gradient of the freestream is simply zero. The gradient of the velocity field induced by the vortex rings is obtained by a simple differentiation. Finally, the component of the gradient of the vector

potential is as follows,

$$\left(\vec{\alpha}^p(t)\cdot\nabla\right)\vec{U}_\sigma\left(\vec{r}^p(t),t\right)=\frac{1}{4\pi}\sum_q\left[-\frac{\left(\left\|\vec{r}^p(t)-\vec{r}^q(t)\right\|^2+\frac{5\sigma^2}{2}\right)}{\left(\left\|\vec{r}^p(t)-\vec{r}^q(t)\right\|^2+\sigma^2\right)^{5/2}}\vec{\alpha}^p(t)\times\vec{\alpha}^q(t)\right.$$
$$\left.+3\frac{\left(\left\|\vec{r}^p(t)-\vec{r}^q(t)\right\|^2+\frac{7\sigma^2}{2}\right)}{\left(\left\|\vec{r}^p(t)-\vec{r}^q(t)\right\|^2+\sigma^2\right)^{7/2}}\times\left(\vec{\alpha}^p(t)\cdot\left(\vec{r}^p(t)-\vec{r}^q(t)\right)\left(\vec{r}^p(t)-\vec{r}^q(t)\right)\times\vec{\alpha}^q(t)\right)\right] \tag{V.30}$$

To discretize the equations of the evolution of the vortons, we use a forward Euler scheme. First the position of the vorton is updated,

$$\vec{r}^p(t+dt)=\vec{r}^p(t)+\vec{U}\left(\vec{r}^p(t),t\right)dt \tag{V.31}$$

Then the strength of the particle is updated,

$$\vec{\alpha}^p(t+dt)=\vec{\alpha}^p(t)+\left(\vec{\alpha}^p(t)\cdot\nabla\right)\vec{U}\left(\vec{r}^p(t),t\right)dt \tag{V.32}$$

To summuraize, we saw how to solve Poisson's equation by using vortons in the wake. We also presented the two evolution equations of the position and strength of the vortons. We still need to compute the initial strength and position of the vortons when they are created in the wake. In the two following sections, I will detail how the vorticity is shed into the wake and thus, how the vortons are created.

a.4 The Kutta condition

The flow being assumed inviscid, we need a Kutta condition. This condition ensures that the fluid leaves the trailing edge smoothly. A jump in pressure of zero at the center of the trailing edge panels will be imposed. This condition will be detailed in the following section.

a.5 The wake description

The process of wake generation and vortex shedding will be presented in this section. The wake is divided into two parts, a near wake and a far wake. The near wake is modeled

using one row of vortex rings; the far wake is composed of vortons as seen in Figure V.5. The strength of the near wake is unknown and needs to be computed using the Kutta condition. The strength and position of the vortons are updated using the evolution equations, Equation V.31 and V.32.

I will first explain how the conversion of the near wake into a far wake is handled; then I will describe the Kutta condition used in the present method.

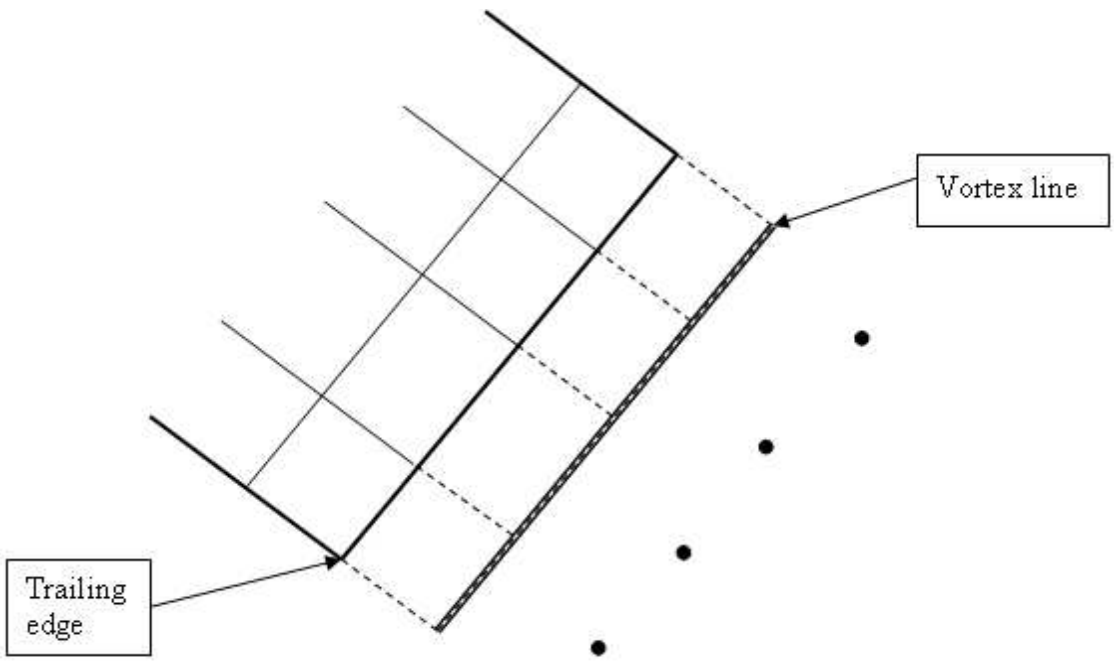

Figure V.5: Description of the near and far wake. The solid lines represent the wing, the dashed lines are the vortex rings of the near wake, the dots are the vortons.

Reviewing the literature, different methods have been used to convert the near wake into a far wake. Willis et al. [11] uses the following approach. The unknown first wake panel (what they call the buffer wake) is convected from the trailing edge at a velocity of $c_w U_\infty$, where c_w is an arbitrary constant between 0.3 and 0.5. The use of such a constant is also described by Katz and Plotkin [12]. Even though using a constant of unity seems more intuitive, we will analyze in a further section the impact of this constant. At the next time step, the near wake is convected then converted into vortons. We proposed six different ways of converting the quadrilateral rings into vortons. They are represented in Figure V.6. The strength $\vec{\alpha}^p(t)$ of the vorton is obtained by integrating the strength of a vortex line,

$$\vec{\alpha}^p(t) = \int \Gamma \overrightarrow{ds} \tag{V.33}$$

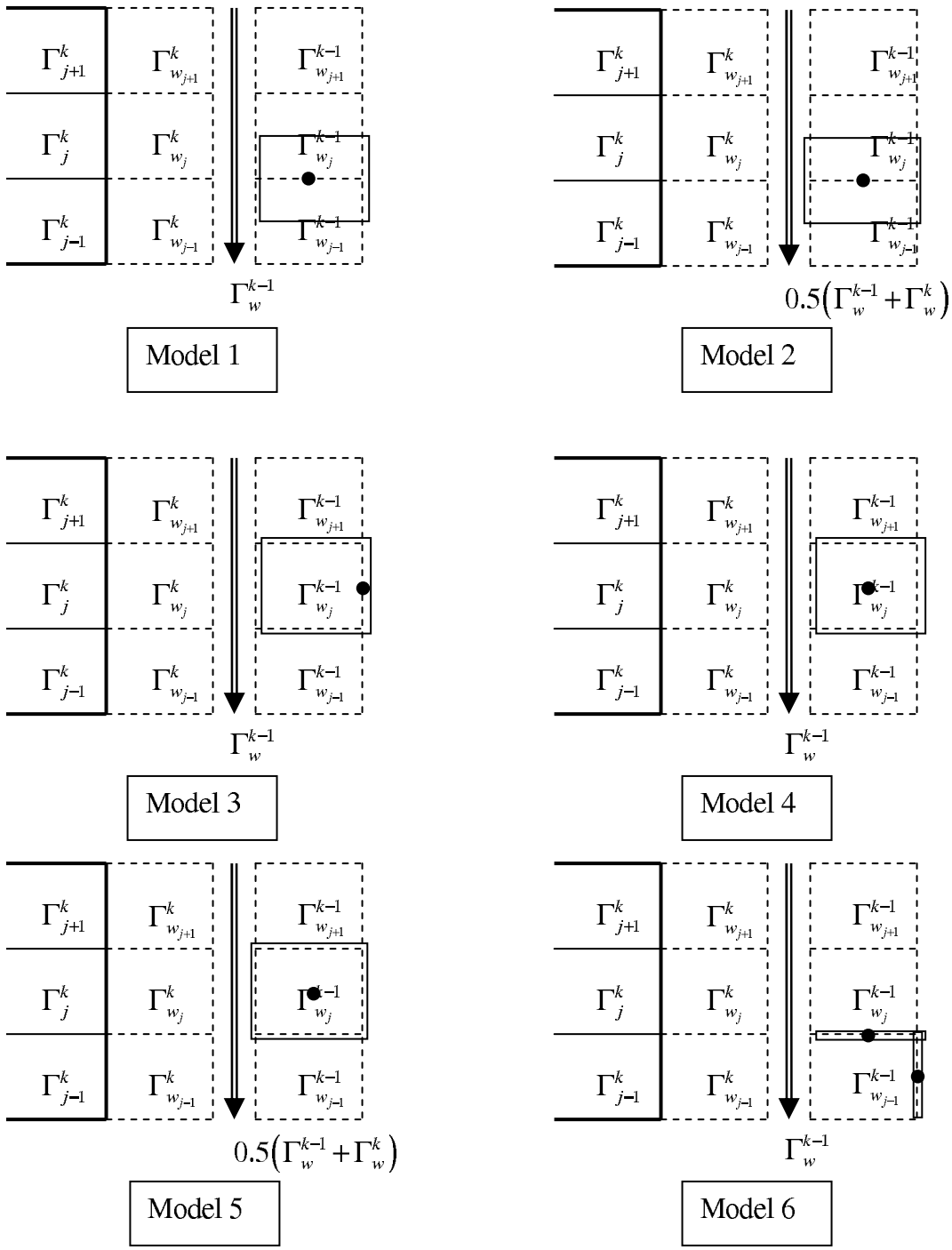

Figure V.6: Six models for the conversion of the near wake rings into vortons. The dashed lines are the vortex rings in the wake, the solid rectangle in the wake is the volume of integration and the double lined arrow is vortex line not included in the integration.

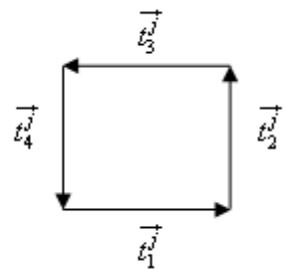

Figure V.7: Notation for a ring panel.

In Figure V.6, the solid line rectangle represents the volume of integration. The conversion is done as followed:

- The four corners of each near wake ring are convected with the local velocity.
- The location and strength of the vortons are computed according to the particular model used.
- The strength of the vortex line between the near and far wake is updated.

For example in the case of Model 3, with the notations of Figure V.7, we have the following strength

$$\vec{\alpha}^j(k) = 0.5\overrightarrow{t_1^i}\left(-\Gamma_{w_{j-1}}^{k-1} + \Gamma_{w_j}^{k-1}\right) + \overrightarrow{t_2^i}\left(\Gamma_{w_j}^{k-1} - \Gamma_{w_j}^{k-2}\right) + 0.5\overrightarrow{t_3^i}\left(\Gamma_{w_j}^{k-1} - \Gamma_{w_{j+1}}^{k-1}\right) \qquad \text{(V.34)}$$

We compared each of the six models to a model with a frozen wake and rings in the wake. Model 3 gives a very close answer for the aerodynamic forces to the theory with rings in the wake. It will be the model used.

As mentioned earlier, the strength of the near wake is unknown. The strength of each panel is found using a Kutta condition. In the literature, this condition is often approximated. For example, Willis et al. [11] uses a steady approximation by saying that the doublet strength of the near wake panel is equal to the doublet strength of the last panel on the wing. This assumption is a quasi steady assumption. This approximation cannot be made for hovering flapping flight which is a fully unsteady process. The condition used

in the present model stipulates that the jump in pressure (pressure difference between the upper and lower pressure) at each time step is zero at the center of the last panels of the wing. The equation for ΔP involves the product of the ring strength of the near wake and the ring strength of the last panels on the wing, leading to a non-linear equation that is solved using an accelerated Newton's method detailed in Press et al. [74]. The jump in pressure is derived by Katz and Plotkin [12] and for the last panels of the wing it can be written as

$$\Delta P^k_{N_i,j} = \rho \left\{ \left[-\vec{U}_b(k) + \vec{U}_w(k) \right]_{N_i,j} \cdot \overrightarrow{t_1^j} \frac{-\Gamma^k_{N_i,j} + \Gamma^k_{N_i-1,j}}{\left\| \overrightarrow{t_1^j} \right\|} \right.$$

$$\left. + \left[-\vec{U}_b(k) + \vec{U}_w(k) \right]_{N_i,j} \cdot \overrightarrow{t_4^j} \frac{\Gamma^k_{N_i,j} - \Gamma^k_{N_i,j-1}}{\left\| \overrightarrow{t_4^j} \right\|} - \frac{\Gamma^k_{N_i,j} - \Gamma^{k-1}_{N_i,j}}{\Delta t} \right\}, \; j = 1, \ldots, N_j \qquad \text{(V.35)}$$

where $\vec{U}_b$ is the velocity of the wing, $\vec{U}_w$ is the velocity induced by the wake, N_i the number of panel in the chordwise direction and N_j the number of panel in the spanwise direction.

Finally, the aerodynamic forces and power are computed the same way as in two-dimensions by using the unsteady Kutta-Joukowsky formula,

$$\vec{F}^k_{i,j} = \rho \left\{ \left(-\vec{U}_b(k) + \vec{U}(k) + \vec{U}_\infty(k) \right) \times \overrightarrow{t_4^{i,j}} \left(\Gamma^k_{i,j} - \Gamma^k_{i-1,j} \right) \right.$$

$$\left. + \left(-\vec{U}_b(k) + \vec{U}(k) + \vec{U}_\infty(k) \right) \times \overrightarrow{t_1^{i,j}} \left(\Gamma^k_{i,j} - \Gamma^k_{i,j-1} \right) - \frac{\Gamma^k_{i,j} - \Gamma^{k-1}_{i,j}}{\Delta t} \frac{\overrightarrow{t_1^{i,j}} \times \overrightarrow{t_4^{i,j}}}{\left\| \overrightarrow{t_1^{i,j}} \times \overrightarrow{t_4^{i,j}} \right\|} \left\| \overrightarrow{t_1^{i,j}} \right\| \cdot \left\| \overrightarrow{t_4^{i,j}} \right\| \right\}$$

$$\text{(V.36)}$$

In this section, we saw how the near wake rings were converted into the far wake vortons. We also saw how to compute the strength of the near wake with the Kutta condition. We can now summurize the entire algorithm. It is composed of the following steps:

1. Compute the location of the wing at time step k.

2. Form the $[A]^k$ matrix and vector $(b)^k$ of Equation V.18.

3. Form the Jacobian matrix $[J]^k$ by differentiating Equation V.18 and V.35.

4. Use the accelerated Newton's method to obtain $[\Gamma_{ij}]^k$ on the wing and $\left[\Gamma_{w_j}\right]^k$ for the near wake.

5. Compute the aerodynamic forces and power acting on the wing using Equation V.36.

6. Update the location of the near wake by convecting its corner and update the location and strength of the far wake using Equations V.26 and V.29.

7. Convert the updated near wake into vortons and go back to step 1.

To conclude, we are now able to solve the inviscid problem. In the following section, we will include the corrective factor that models the effects of viscosity.

b Viscous formulation

To model accurately the effect of viscosity, one should solve the full Navier-Stokes equations. However, the goal in this thesis is to develop methods that can provide quick estimates for preliminary design. Solving the full Navier-Stokes equations in three-dimensions is extremely time consumming. One way of adding the viscous effect is to couple the potential solver to a Boundary-Layer method (see Cebeci [75]). Nevertheless, this method only works for attached flows. In addition, we saw that for highly accelerated flows, inviscid effects were predominant. Thus, we can add the same correction factor as in Chapter IV,

$$\begin{aligned} \vec{F}_{viscous} &= \tfrac{1}{2}\rho c \int_{-B/2}^{B/2} U^2(y)\, C_D(y)\, \frac{\vec{U}(y)}{\left\|\vec{U}(y)\right\|} dy \\ P_{viscous} &= \int_{-B/2}^{B/2} \vec{d}F_{viscous}(y) \cdot \vec{U}_{wing}(y)\, dy \\ \vec{U}(y) &= \text{Induced velocity - wing velocity} \end{aligned} \tag{V.37}$$

where $\vec{U}(y)$ is only a function of the span location and is computed at a point taken along the chord. In practice, $\vec{U}$ is taken as being the velocity given by the actuator disk theory for a given thrust minus the wing velocity at the computed point. Consequently the viscous force can be fully computed during the post-processing of the inviscid results. Thus, it is possible to incorporate different viscous models without re-computing the full inviscid solution.

In the three-dimensional case, we only use the constant drag model based on the experiments of Weis-Fogh [32].

So far, we have described the method behind the theory developed. We now need to test this present model against known limiting results.

V.3.3 Convergence study

In this section, we compare the aerodynamic forces and power provided by the present method to known results from the literature. We will first look at the aerodynamics in the limit case of high aspect ratio wings. We will then look at results for finite aspect ratio wings. Finally we will present the convergence tests in hovering.

a High aspect ratio with small amplitudes

In this section, a frozen wake is used, with rings in the wake as opposed to vortons, and a rectangular wing of high aspect ratio ($AR = 100$). Because the aspect ratio is so high, the use of vortons is not possible. Vortons are discrete points with a vorticity distribution associated to them. These distributions need to overlap to accurately model the vorticity field. With very high aspect ratios, the number of vortons needed becomes high, increasing the computational time. Whereas, rings use vortex lines that spreads across the span of the wing, and thus do not encounter this problem. Consequently, in this section, we will use rings in the wake. The number of panels in the spanwise direction does not influence the solution. Thus, in this section we will only vary the number of panels in the chordwise direction (N_i).

a.1 Sudden change in pitch

For a sudden change in pitch, we can compare the lift computed with the present theory to the Wagner function ϕ. The lift is expressed as

$$L\left(s\right) = 2\pi\rho U^2 b\theta\phi\left(s\right),\ s = \frac{Ut}{b} \tag{V.38}$$

A common approximation of the Wagner function is given by

$$\phi(s) \approx 1 - 0.165e^{-0.0455s} - 0.335e^{-0.3s} \tag{V.39}$$

This first order approximation can be improved. Coller and Chamara [72] developed a higher order approximation,

$$\phi(s) \approx 1 - \sum_{j=1}^{N_\phi} K_j e^{-\sigma_j s} \tag{V.40}$$

with $N_\phi = 4$, $K_1 = 0.2552078488$, $\sigma_1 = 0.1708445093$, $K_2 = 0.1290432917$, $\sigma_2 = 0.5610424665$, $K_3 = 0.09654817188$, $\sigma_3 = 0.04680475392$, $K_4 = 0.01920068755$, $\sigma_4 = 0.006478169099$. As we can see in Figure V.8, there is a relatively good agreement. During the first few iterations, we observe a difference between the two curves. Nevertheless, this difference is not present in the vortex method as we will see in a later section. In addition, the difference for later times could be explained by the fact that the approximation used for the Wagner function is especially good for low values of the non-dimentional time. Even by increasing the order of the approximation by using Coller's approximation, we observe some discrepancies. These differences are not present in the vortex method as we will see in section V.3.3 b.2

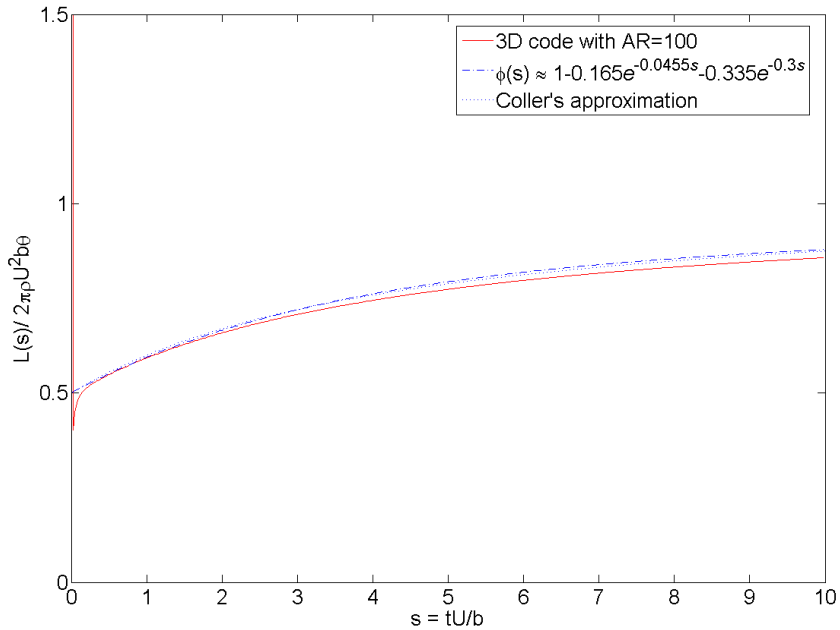

Figure V.8: Non dimensional lift for a sudden change in pitch.

a.2 Plunging motion

In this section, we use a rectangular wing of aspect ratio $AR = 100$, undergoing small amplitude plunging motion. Since the wing has a high aspect ratio, the three-dimensional effects will be neglectible and the aerodynamic forces can be compared to the two-dimensional forces developed by Theodorsen [15] and Garrick [16]. Five cycles are enough to reach convergence. The notation used in Table V.1 is the same as the notation used in the previous chapter.

We can see on Table V.1 that increasing the number of panels or the number of point per flapping cycle does not necessarily mean reducing the error. However we can see that if we both decrease the time step and increase the number of points on the wing, then the error decreases. It can also be noted that for higher reduced frequencies, we observe the same behavior as in the two-dimensional case; the error in the mean thrust and especially in the mean power increase. The explanation for this phenomenon is the same as before; it is due to averaging error. To verify this statement, we compare the value of the peak power given by the present method to the value of the peak power found by Theodorsen

[15] and Garrick [16] and gather the error in Table V.2. This error is relatively smaller for the peak value in coefficient of pressure than for its mean.

k	N_i	NTS	$\langle C_P \rangle$	$\langle C_T \rangle$	$C_{L_{peak}}$
0.39	25	50	0.17%	-1.83%	-0.10%
0.39	25	100	-2.97%	-4.25%	-3.01%
0.39	25	200	-4.49%	-5.17%	-4.56%
0.39	50	50	5.13%	3.18%	5.26%
0.39	50	100	1.10%	-0.18%	1.15%
0.39	50	200	-1.18%	-1.82%	-1.10%
0.39	100	50	8.85%	6.88%	9.45%
0.39	100	100	4.24%	2.83%	4.40%
0.39	100	200	1.27%	0.53%	1.32%
0.79	25	50	2.01%	-3.49%	0.06%
0.79	25	100	-0.25%	-3.47%	-1.60%
0.79	25	200	-1.39%	-3.48%	-2.49%
0.79	50	50	3.67%	-1.72%	1.79%
0.79	50	100	1.30%	-1.63%	0.13%
0.79	50	200	0.13%	-1.63%	-0.77%
0.79	100	50	4.46%	-0.89%	2.66%
0.79	100	100	2.07%	-0.76%	1.00%
0.79	100	200	0.86%	-0.77%	0.09%
1.57	25	50	5.20%	-6.11%	-1.83%
1.57	25	100	1.37%	-6.35%	-3.13%
1.57	25	200	-0.91%	-6.44%	-3.72%
1.57	50	50	7.52%	-2.61%	0.17%
1.57	50	100	3.62%	-2.91%	-1.07%
1.57	50	200	1.26%	-2.95%	-1.64%
1.57	100	50	8.64%	-0.98%	1.21%
1.57	100	100	4.67%	-1.32%	-0.01%
1.57	100	200	1.86%	-1.34%	-0.56%
3.14	25	50	8.49%	-13.50%	-8.23%
3.14	25	100	-0.44%	-14.06%	-8.89%
3.14	25	200	-4.84%	-14.25%	-9.25%
3.14	50	50	14.27%	-7.21%	-4.13%
3.14	50	100	4.47%	-7.47%	-4.84%
3.14	50	200	-0.33%	-7.59%	-5.24%
3.14	100	50	18.69%	-3.52%	-1.34%
3.14	100	100	7.70%	-3.75%	-2.27%
3.14	100	200	2.32%	-3.88%	-2.78%

Table V.1: Error for the mean coefficient of thrust, power and peak lift coefficient obtained by the present three-dimensional method with $AR = 100$ compared to the results of Theodorsen [15] and Garrick [16] for a pure plunging motion.

k	N_i	NTS	$\langle C_P \rangle$	$C_{P_{peak}}$
3.14	50	50	14.27%	-4.10%
3.14	50	100	4.47%	-4.87%
3.14	50	200	-0.33%	-5.30%
3.14	100	50	18.69%	-1.29%
3.14	100	100	7.70%	-2.32%
3.14	100	200	2.32%	-2.84%

Table V.2: Error for the mean coefficient of power and its peak obtained by the present three-dimensional method with $AR = 100$ compared to the results of Theodorsen [15] and Garrick [16] for a pure plunging motion.

We mentioned earlier that Willis et al. [11] use a special treatment for the convection of the first wake panel. They convect the wake at the freestream velocity times a constant c_w taking values from 0.3 to 0.5 (see Figure V.9). This method is also mentioned in Katz and Plotkin [12]. Two problems arise with this method. First they use a non-unity factor to convect the near wake, which does not rely on a physical meaning. Second, the wake is convected at the freestream speed and not the total induced speed. In hovering flapping flight the freestream is zero making it impossible to convect the wake by the method used by Willis et al. Consequently we wanted to see if the presence of this constant would impact on the convergence of the present method. We ran the same plunging simulation, but this time instead of a constant of $c_w = 1$, we used a constant of 0.5. Results are presented in Table V.3. As seen on Table V.3, the errors are similar to those of Table V.1. Thus, the use of this factor is not justified in the present method. This could be explained by the fact that Willis et al. use a steady state Kutta condition introducing approximations in their aerodynamic coefficients and that by using a different near wake panel size, they compensate for this approximation. Thus, hereafter a coefficient of unity will be used in the present method.

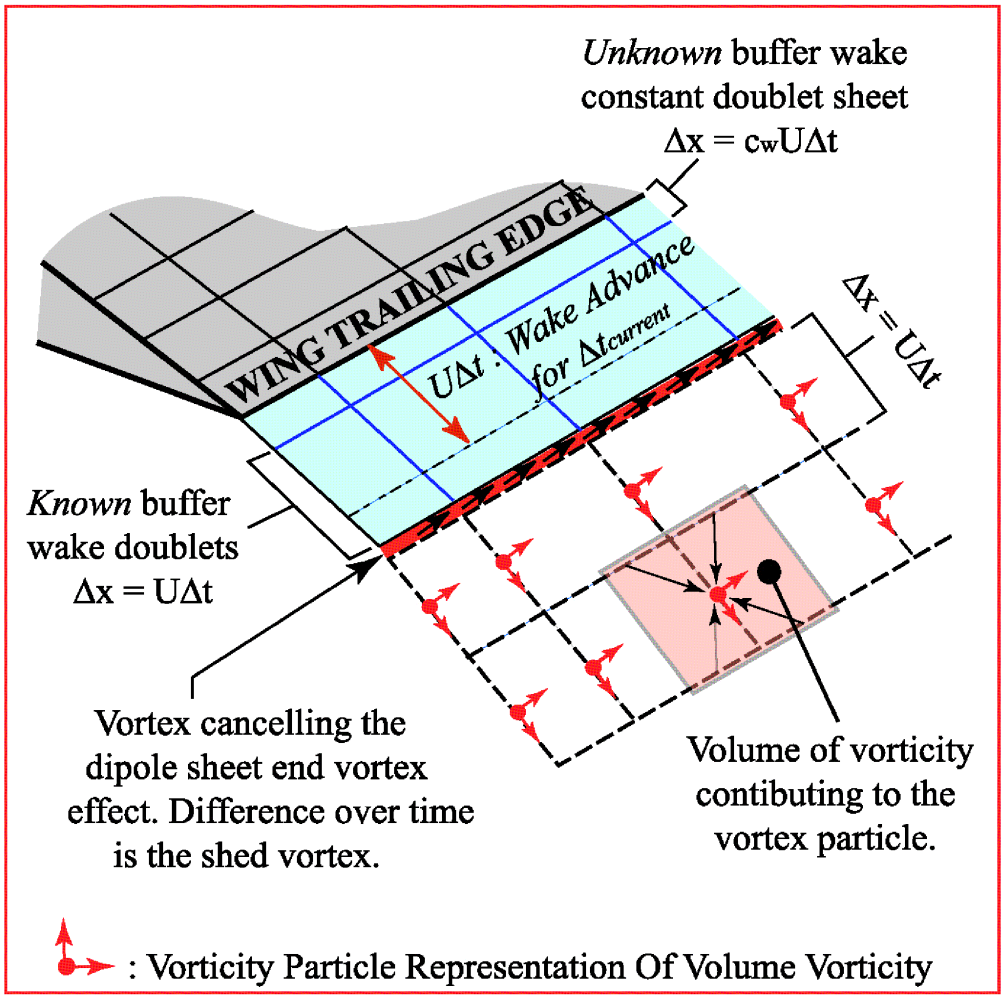

Figure V.9: "A description of the unknown and known buffer wake regions at the trailing edge of a wing. Notice also the conversion of the line vortices resulting from the constant strength dipoles, into point vortices." Reprinted from Willis et al. [11].

k	N_i	NTS	$\langle C_P \rangle$	$\langle C_T \rangle$	$C_{L_{peak}}$
0.39	25	50	-3.81%	-6.30%	-4.12%
0.39	25	100	-4.94%	-6.26%	-5.05%
0.39	25	200	-5.23%	-5.92%	-5.29%
0.39	50	50	-0.57%	-3.12%	-0.85%
0.39	50	100	-2.28%	-3.57%	-2.38%
0.39	50	200	-2.77%	-3.35%	-2.87%
0.39	100	50	1.95%	-0.77%	1.72%
0.39	100	100	-0.43%	-1.84%	-0.50%
0.39	100	200	-1.35%	-1.96%	-1.46%
3.14	25	50	7.76%	-13.45%	-8.37%
3.14	25	100	-0.64%	-14.03%	-8.93%
3.14	25	200	-4.89%	-14.24%	-9.28%
3.14	50	50	12.53%	-7.28%	-4.58%
3.14	50	100	3.90%	-7.47%	-4.99%
3.14	50	200	-0.49%	-7.59%	-5.28%
3.14	100	50	15.17%	-3.94%	-2.40%
3.14	100	100	6.32%	-3.86%	-2.70%
3.14	100	200	1.89%	-3.90%	-2.90%

Table V.3: Error for the mean coefficient of thrust, power and peak lift coefficient obtained by the present three-dimensional method with $AR = 100$ and $c_w = 0.5$ compared to the results of Theodorsen [15] and Garrick [16] for a pure plunging motion.

a.3 Pitching motion

The same convergence study is done for a pure pitching motion about the quarter chord of the wing. The same trend as before can be observed on Table V.4. This time, the error on the mean coefficient of thrust is large. The same test to see if it is a problem with the averaging can be conducted.

We can see on Table V.5 that the error for the peak coefficient of thrust is smaller. The same phenomenon explained above is happening for the coefficient of thrust.

To conclude, we saw that the present method gave good agreement with the Theodorsen's theory. A number of 50 panels in the chordwise direction and 50 points per flapping cycle seem to give good results within a reasonable computing time. These convergence tests were performed on the method that uses rings in the wake in order to compare results to the known two-dimensional results. However, further convergence tests will be needed. First, we need to test if the method using vortons in the wake agrees with the method using rings in the wake for a finite aspect ratio wing with a frozen wake. Second, we can compare the three-dimensional method with vortons for finite aspect ratio wings to results of Willis et al. [11]. Finally, convergence tests on the method using vortons with a free wake will be performed.

k	N_i	NTS	$\langle C_P \rangle$	$\langle C_T \rangle$	$C_{L_{peak}}$
1.57	25	50	-17.98%	-54.78%	-11.90%
1.57	25	100	-19.85%	-48.57%	-13.36%
1.57	25	200	-20.54%	-45.14%	-14.29%
1.57	50	50	-7.13%	-37.78%	-4.43%
1.57	50	100	-10.14%	-31.43%	-6.66%
1.57	50	200	-11.35%	-27.61%	-7.54%
1.57	100	50	0.45%	-26.37%	0.98%
1.57	100	100	-3.30%	-20.76%	-2.27%
1.57	100	200	-5.43%	-17.08%	-3.46%
3.14	25	50	-17.34%	-37.61%	-16.27%
3.14	25	100	-20.02%	-34.80%	-16.92%
3.14	25	200	-21.28%	-33.74%	-17.40%
3.14	50	50	-6.34%	-24.58%	-8.08%
3.14	50	100	-9.91%	-21.35%	-9.14%
3.14	50	200	-11.51%	-20.07%	-9.38%
3.14	100	50	1.56%	-16.37%	-2.70%
3.14	100	100	-3.30%	-13.10%	-4.37%
3.14	100	200	-5.47%	-11.75%	-4.98%

Table V.4: Error for the mean coefficient of thrust, power and peak lift coefficient obtained by the present three-dimensional method with $AR = 100$ compared to the results of Theodorsen [15] and Garrick [16] for a pure pitching motion about the elastic axis.

k	N_i	NTS	$\langle C_T \rangle$	$C_{T_{peak}}$
1.57	25	50	-54.78%	-11.30%
1.57	25	100	-48.57%	-11.87%
1.57	25	200	-45.14%	-12.19%
1.57	50	50	-37.78%	-5.12%
1.57	50	100	-31.43%	-6.17%
1.57	50	200	-27.61%	-6.75%
1.57	100	50	-26.37%	-1.27%
1.57	100	100	-20.76%	-2.28%
1.57	100	200	-17.08%	-3.33%

Table V.5: Error for the mean coefficient of thrust and its peak obtained by the present three-dimensional method with $AR = 100$ compared to the results of Theodorsen [15] and Garrick [16] for a pure pitching motion about the elastic axis.

b Finite aspect ratio wing

When dealing with flapping, I will use the non-dimensional coefficients derived in section I.2,

$$\begin{aligned} C_L &= \frac{L}{2\rho B^4 \varpi^2 \left(\frac{\phi}{180}\right)^3} \\ C_T &= \frac{T}{2\rho B^4 \varpi^2 \left(\frac{\phi}{180}\right)^3} \\ C_P &= \frac{P}{2\rho B^5 \varpi^3 \left(\frac{\phi}{180}\right)^4} \end{aligned} \tag{V.41}$$

b.1 Vortex rings versus vortons in the wake

Having tested the method that uses vortex rings in the wake, we wanted to see if by switching to vortons in the wake we would get the same results. In this case we use a wing of aspect ratio $AR = 3$. Since the method using rings only works for frozen wakes, we used a lightly loaded simulation. The wing was flapping at a reduced frequency of $k = \frac{\omega b}{U_\infty} = 0.0393$, a stroke angle $\phi_1 = 0.2°$. The discretization of the wing and the time step were identical in both cases (40 panels in the chordwise direction and 20 in the spanwise direction). To compare the vorton method to the ring method, we run three simulations

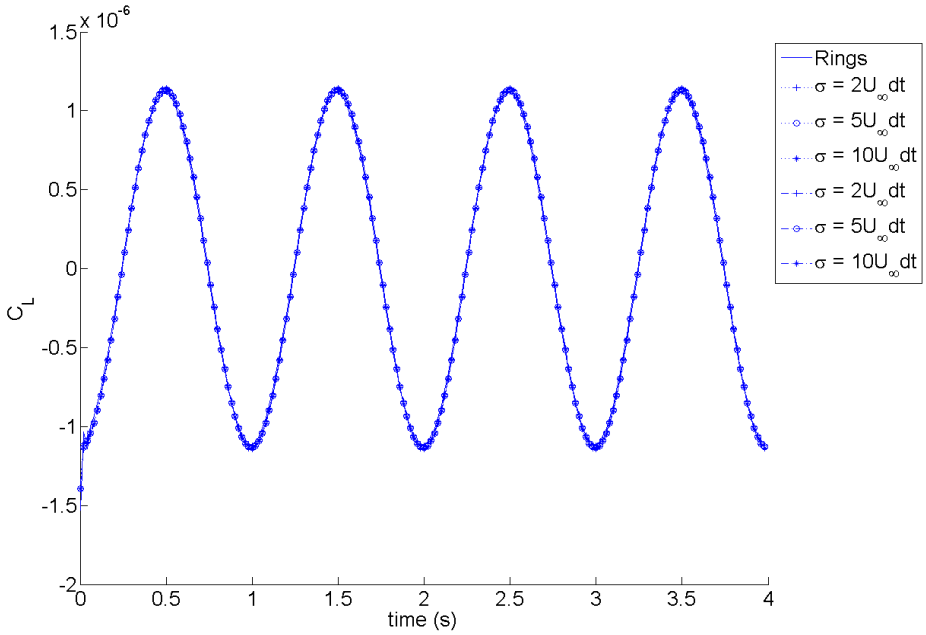

Figure V.10: Coefficient of lift function of time for a wing of aspect ratio $AR = 3$ undergoing flapping motion of $\phi_1 = 0.2°$ at a reduced frequency of $k = 0.0393$. The solid line represents the result with the ring method, the dotted lines the results using vortons with a frozen wake and dash-dot lines the results using vortons with a free wake.

with a frozen wake and three with a free wake. Each of the simulation differs by the value of the cut-off radius (σ) used in the regularization function. The cut-off radius is taken to be a factor times the distance between two vortons (U_∞dt). In the simulations we used a factor of 2, 5 and 10.

As seen in Figure V.10, Figure V.11 and Figure V.12, the curves do not present a difference between each others. This first shows that the vorton method is consistent with the ring method in the case of a frozen wake. Consequently, since the ring method agrees for a high aspect ratio wing with the Theodorsen aerodynamics, and the vorton method agrees for finite aspect ratio wings to the ring method, by induction it shows that the present vorton method gives physical results, at least for the case considered here.

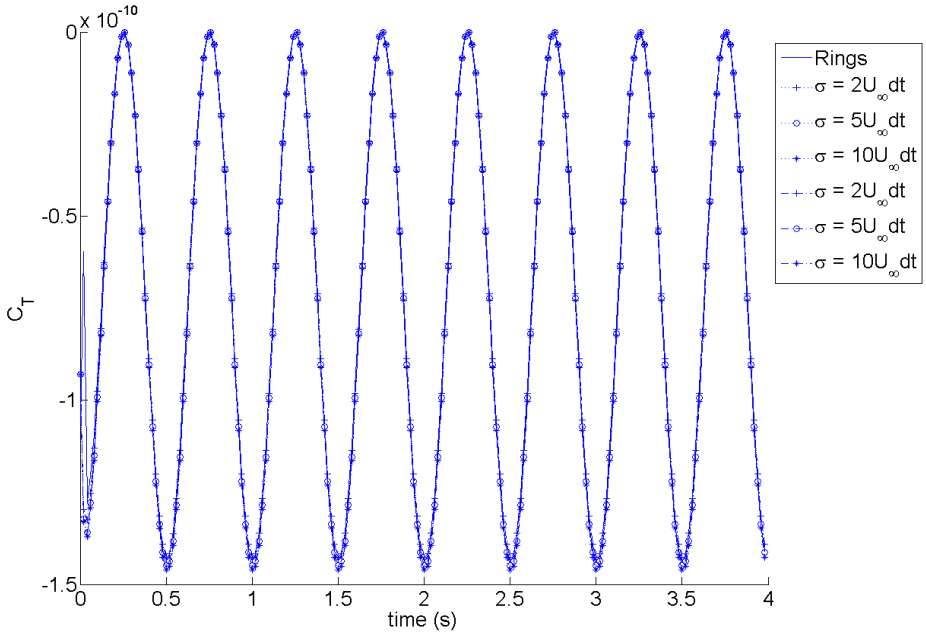

Figure V.11: Coefficient of thrust function of time for a wing of aspect ratio $AR = 3$ undergoing flapping motion of $\phi_1 = 0.2°$ at a reduced frequency of $k = 0.0393$. The solid line represents the result with the ring method, the dotted lines the results using vortons with a frozen wake and dash-dot lines the results using vortons with a free wake.

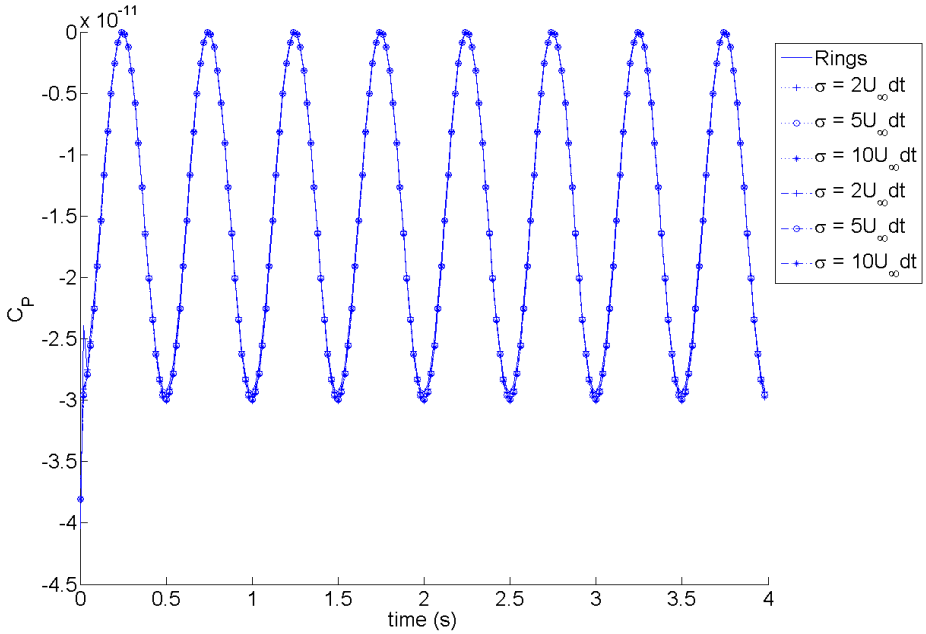

Figure V.12: Coefficient of power function of time for a wing of aspect ratio $AR = 3$ undergoing flapping motion of $\phi_1 = 0.2°$ at a reduced frequency of $k = 0.0393$. The solid line represents the result with the ring method, the dotted lines the results using vortons with a frozen wake and dash-dot lines the results using vortons with a free wake.

In addition, we can see that for lightly loaded wings the aerodynamic coefficients are the same with a frozen and a free wake. This is true for small-amplitude motion only; or more precisely, lightly loaded cases. In the lightly loaded case, the induced velocities of the wake on itself are small and thus the roll-up of the wake is negligible.

To summarize, we saw that for finite aspect ratio wings, the method with rings in the wake and the one with vortons both agree. Nevertheless, we should directly test the results provided by the present vorton method against results found in the literature. This is done in the next section, where we look at a sudden change in pitch for various aspect ratios.

b.2 Sudden change of pitch for finite aspect ratio wings

In this section, we use the present vorton method to compute the lift as a function of time due to a sudden change of pitch for various aspect ratios. Then, we compare the results of the present method to Katz and Plotkin [12] and Willis et al. [11]. As seen in Figure V.13, there is a very good agreement between the present method and Willis' method. This test validates the vortex method in three-dimensions.

After these convergence tests, we can conclude that the vorton method seems to compare well to results provided by the literature. The next step is now to study the convergence in hovering flapping flight.

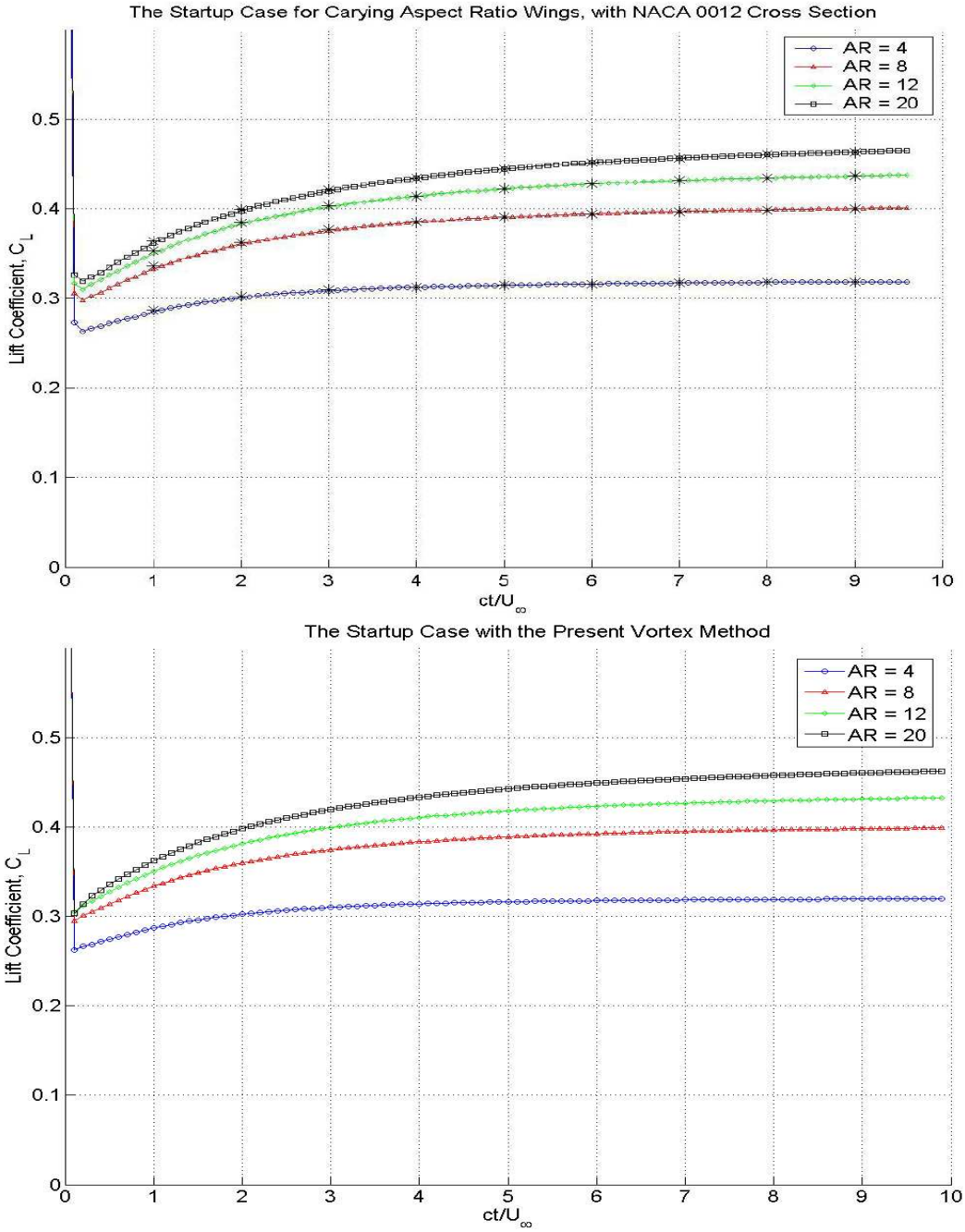

Figure V.13: The C_L evolution with time due to a sudden change of pitch. The top plot is reprinted from Willis et al. [11]. The (*) markers are results of Katz and Plotkin [12]. The bottom plot was obtained with present method.

c Convergence in hovering

In the hovering case we will define the cut-off radius as

$$\sigma = \sigma_K \left[V_{tip}\right]_{\max} dt \tag{V.42}$$

where σ_K is a coefficient of proportionality and $\left[V_{tip}\right]_{\max}$ the maximum speed of the tip of the wing. Consequently the cut-off radius is a multiple of the maximum spacing between two vortons.

Similarly as the two-dimensional case in hovering, a nonzero freestream velocity is imposed over the first few iterations, and is then turned off.

To perform all the convergence tests, we use the same configuration for the wing and its kinematics. The wing is composed of two semi-wings. Each semi-wing has an aspect ratio of 3 and are separated by a gap of $1.35c$. We picked an arbitrary motion to do all the convergence tests. The wing is flapping with a stroke angle of 150°, a pitch angle of 50° about an axis located at $0.2c$ from the leading edge with a phase advance of $\frac{\pi}{2}$ at an arbitrary frequency of $50Hz$. We use 40 panels in the chordwise direction and 20 in the spanwise direction for each semi-wing. Finally, we use 100 points per cycle for the time discretization.

c.1 Convergence in time

The first convergence test looks at the number of cycles needed to reach convergence. As seen in Figure V.14 and Figure V.15 after about 2 cycles, the coefficients seem to converge. Table V.6 confirms the convergence. The values for the mean coefficients only change a little (less than half a percent) when going from an averaging over cycle 350-450 to the cycle after. In additon, we can see that the mean values for cycle 550-650 are axactly the same as the mean values for cycle 350-450. This confirms that convergence was reached at cycle 350-450.

In addition, the simulation takes a long time to run. It takes about 18 hours to run 450 iterations on a Pentium (R) D $2.80GHz$. Consequently, we will use an averaging over cycle 350-450 in the following simulations.

Averaging start (iteration)	Averaging end (iteration)	$\langle C_T \rangle$	$\langle C_P \rangle$	Relative change $\langle C_T \rangle$	Relative change $\langle C_P \rangle$
250	350	-1.035E-02	-1.820E-03		
350	450	-1.051E-02	-1.786E-03	1.61%	-1.84%
450	550	-1.054E-02	-1.782E-03	0.29%	-0.22%
550	650	-1.051E-02	-1.786E-03	0.31%	-0.21%

Table V.6: Averaged mean coefficients of thrust and power for different averaging.

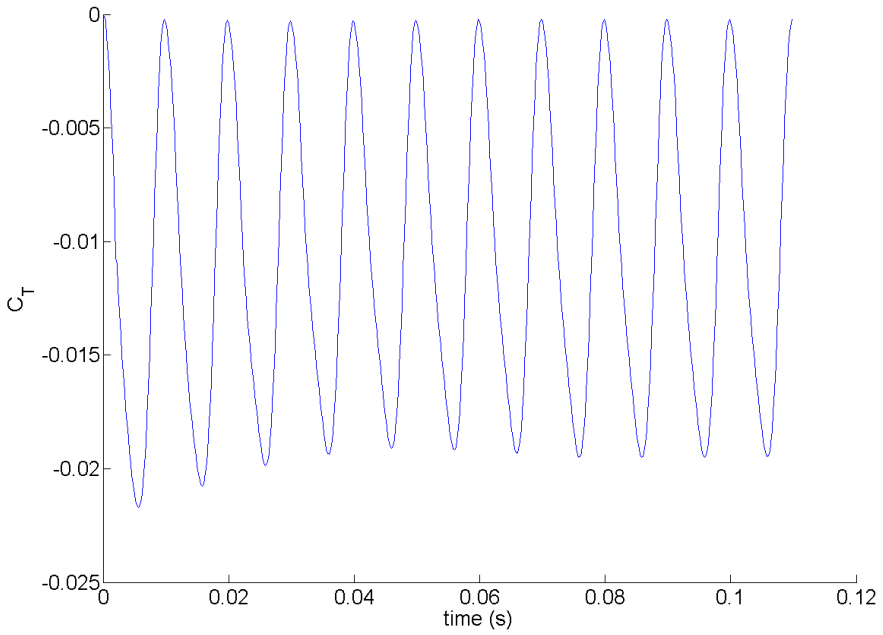

Figure V.14: Coefficient of thrust in hover for a wing in test configuration.

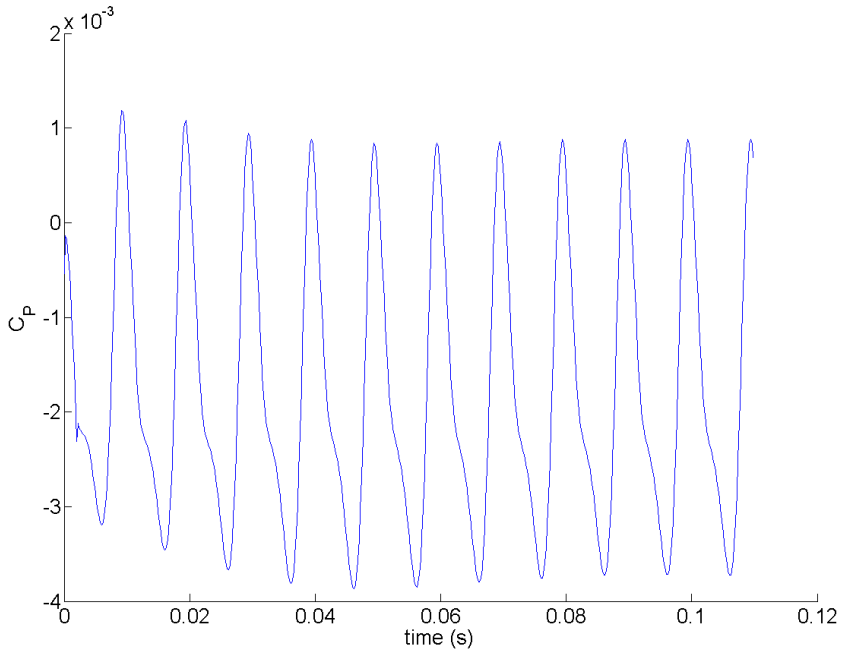

Figure V.15: Coefficient of power in hover for a wing in test configuration.

c.2 Cut-off radius

In this section, the influence of the value of the cut-off radius in the vorton regularized function (see Equation V.23) is studied. Four different cut-off radius coefficients ($\sigma_k = 5, 10, 15, 20$) are used. As seen in Figure V.16 and Figure V.17, after three cycles the coefficients of thrust and power do not change by a lot as the cut-off radius increases. We can notice that the curves with a cut-off radius coefficient of 15 and 20 are almost on top of each other.

On Table V.7, we first notice that the relative changes for the aerodynamic coefficients are within a few percentages. Nevertheless, this relative change is even smaller for σ_K going from 15 to 20. In addition when averaging on the last cycle, the error becomes less than a quarter of a percentage. This result confirms that convergence is reached on the last cycle.

Consequently, we will use a cut-off radius of 15.

σ_K	Averaging start (iteration)	Averaging end (iteration)	$\langle C_T \rangle$	$\langle C_P \rangle$	Relative change $\langle C_T \rangle$	Relative change $\langle C_P \rangle$
5	250	450	-9.233E-03	-1.859E-03		
	350	450	-8.994E-03	-1.847E-03		
10	250	450	-1.028E-02	-1.846E-03	11.34%	-0.73%
	350	450	-1.021E-02	-1.832E-03	13.48%	-0.81%
15	250	450	-1.048E-02	-1.815E-03	1.96%	-1.64%
	350	450	-1.051E-02	-1.786E-03	3.02%	-2.49%
20	250	450	-1.060E-02	-1.800E-03	1.12%	-0.83%
	350	450	-1.054E-02	-1.785E-03	0.26%	-0.04%

Table V.7: Averaged mean coefficients of thrust and power for different cut-off radii. The relative change is computed for an increase in cut-off radius.

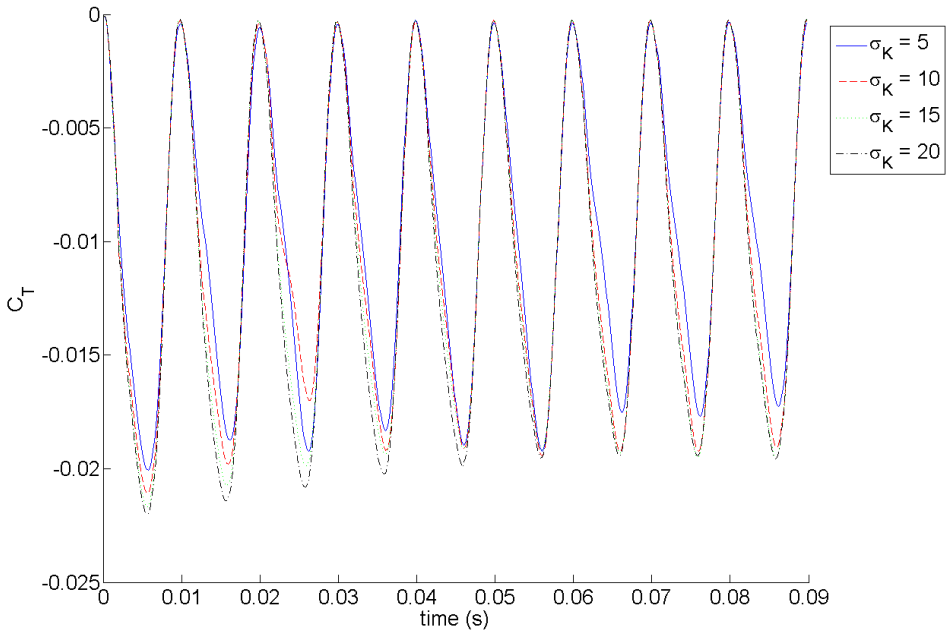

Figure V.16: Coefficient of thrust in hover for a wing in test configuration for different cut-off radii.

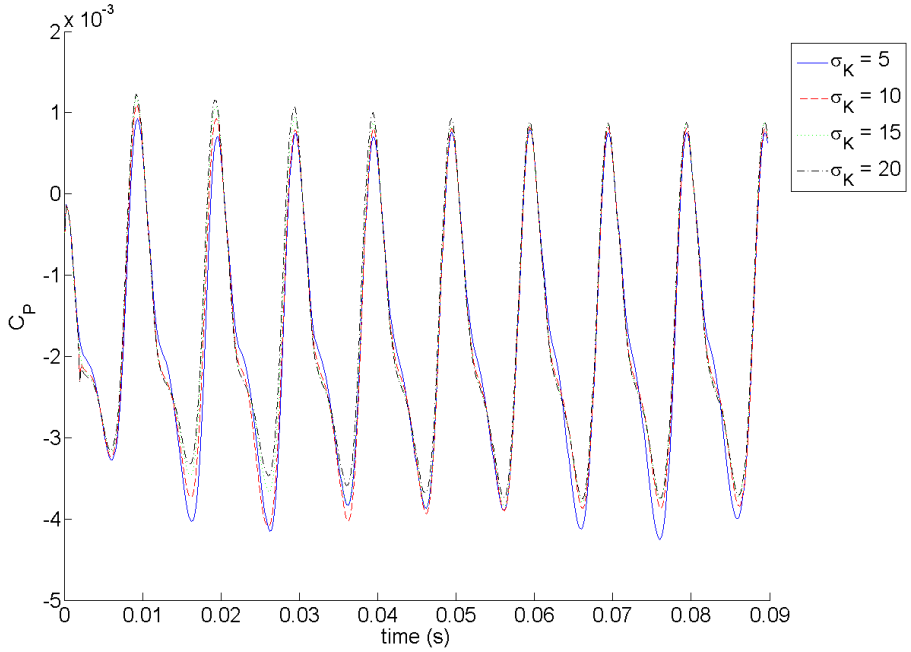

Figure V.17: Coefficient of power in hover for a wing in test configuration for different cut-off radii.

c.3 ϵ in vortex line

As mentioned before, the velocity induced by a vortex filament at a point becomes singular if the point lies on the filament or is aligned with it. Consequently, the use of a cut-off radius becomes necessary when the position of the wake is updated. In other words, a cut-off radius is used in the evaluation of the induced velocities by the first ring wake panel and vortex line on the wake.

Similarly as the cut-off radius for the vortons, a constant of proportionality ϵ_K is introduced,

$$\varepsilon = \varepsilon_K \left[V_{tip}\right]_{\max} dt \tag{V.43}$$

We can see in Figure V.18 and Figure V.19 that for the last cycles, the aerodynamic coefficients with $\epsilon_K = 2.96$ and $\epsilon_K = 0.296$ are on top of each other. For $\epsilon_K = 0.0296$, we observe some discrepancies, nevertheless it seems to converge to the same curve in the last cycle. This is also confirmed by Table V.8. The relative change in aerodynamic coefficients is less than a percent. Consequently, we will use $\epsilon_K = 0.296$ in my simulations.

ϵ_K	Averaging start (iteration)	Averaging end (iteration)	$\langle C_T \rangle$	$\langle C_P \rangle$	Relative change $\langle C_T \rangle$	Relative change $\langle C_P \rangle$
2.96	250	450	-1.048E-02	-1.823E-03		
	350	450	-1.049E-02	-1.798E-03		
0.296	250	450	-1.048E-02	-1.816E-03	0.07%	-0.43%
	350	450	-1.051E-02	-1.786E-03	0.26%	-0.63%

Table V.8: Averaged mean coefficients of thrust and power for different ϵ_K. The relative change is computed for a decrease in ϵ_K.

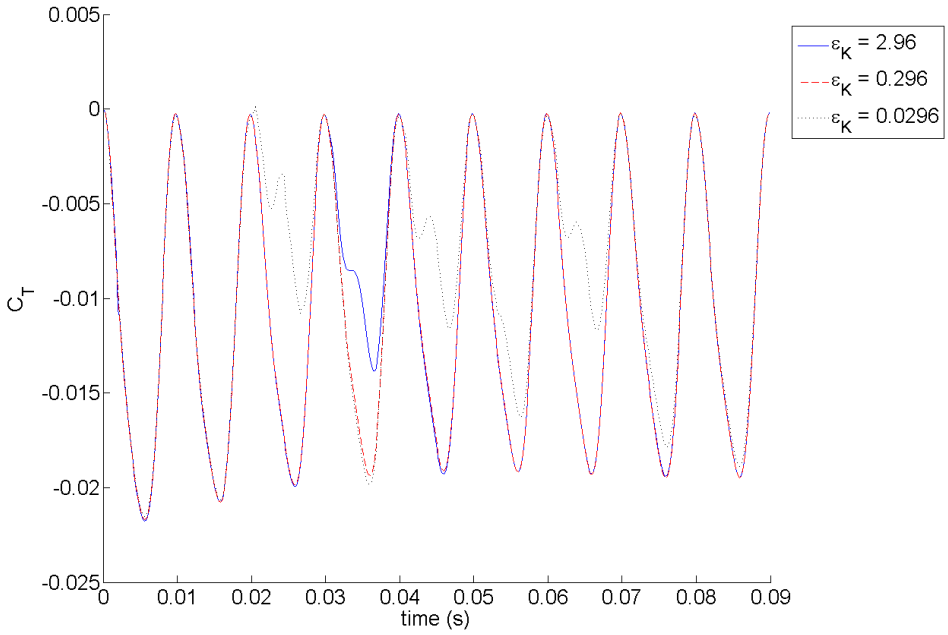

Figure V.18: Coefficient of thrust in hover for a wing in test configuration for different ϵ_K.

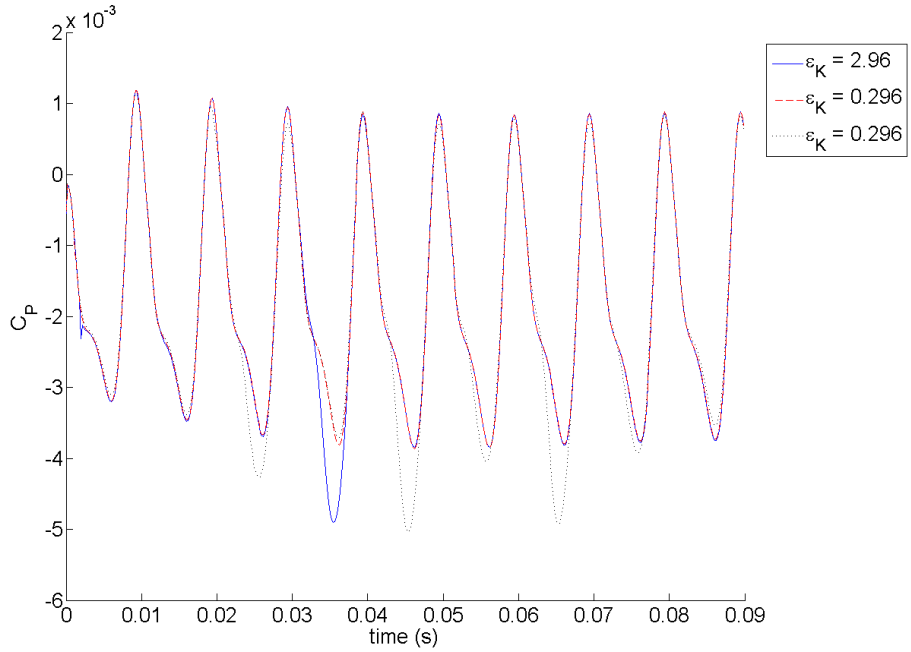

Figure V.19: Coefficient of power in hover for a wing in test configuration for different ϵ_K.

c.4 Freestream velocity

As mentioned earlier, we use a nonzero freestream velocity for the first 10 iterations to initially convect the wake. During these first iterations, the reduced frequency has a finite value. We looked at the influence of the value of that freestream on the averaged aerodynamic coefficients. As seen in Figure V.20 and Figure V.21, for the last cycles the curves are all similar. Furthermore, in Table V.9, we can see that the relative change in aerodynamic coefficients is small, especially going from a reduced frequency of 4.19 to 2.09, this change is almost inexistent. Consequently we will use an initial reduced frequency of 4.19.

k_{start}	Averaging start (iteration)	Averaging end (iteration)	$\langle C_T \rangle$	$\langle C_P \rangle$	Relative change $\langle C_T \rangle$	Relative change $\langle C_P \rangle$
8.38	250	450	-1.052E-02	-1.807E-03		
	350	450	-1.048E-02	-1.792E-03		
4.19	250	450	-1.048E-02	-1.816E-03	-0.35%	0.49%
	350	450	-1.051E-02	-1.786E-03	0.33%	-0.29%
2.09	250	450	-1.048E-02	-1.815E-03	0.00%	-0.01%
	350	450	-1.052E-02	-1.786E-03	0.01%	0.00%

Table V.9: Averaged mean coefficients of thrust and power for different starting velocities. The relative change is computed for a decrease in the reduced frequency.

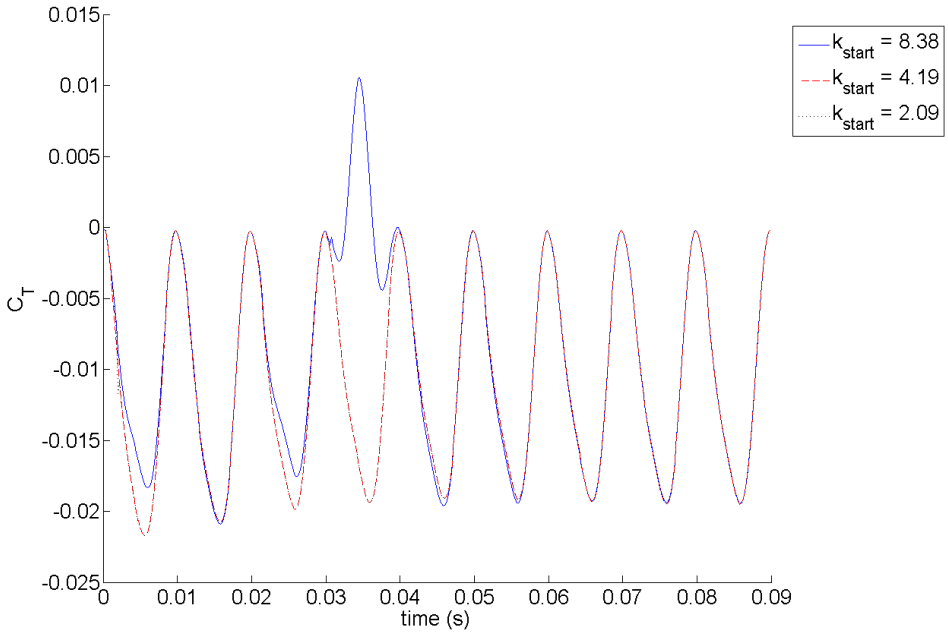

Figure V.20: Coefficient of thrust in hover for a wing in test configuration for different starting reduced frequencies.

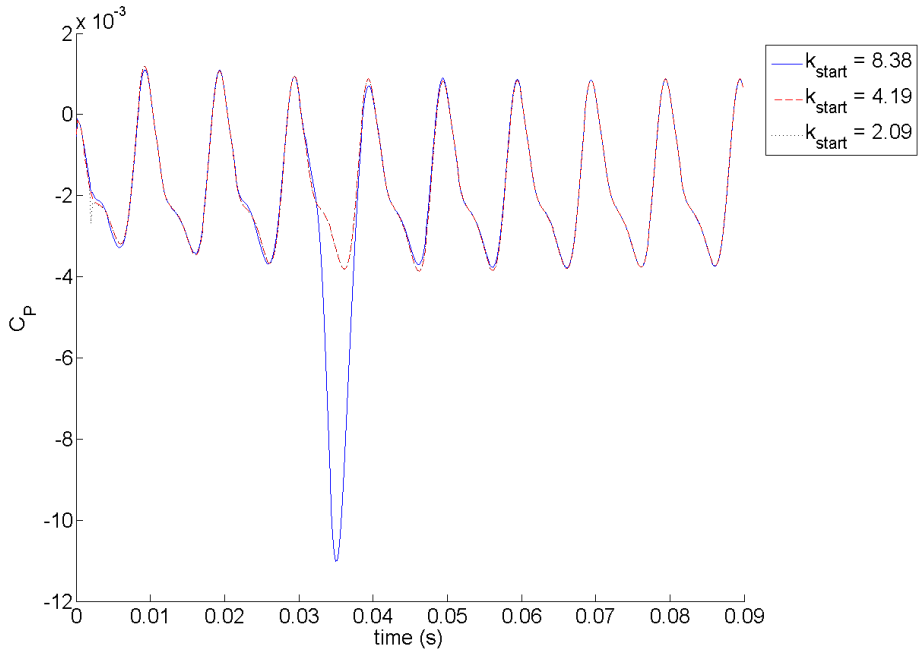

Figure V.21: Coefficient of power in hover for a wing in test configuration for different starting reduced frequencies.

c.5 Number of iterations with the freestream on

To start the convection of the wake during the first few iterations (IT_{start}), the freestream velocity is nonzero. We looked at the influence of the number of iterations during which the freestream is nonzero. As seen in Figure V.22 and Figure V.23, the curves are on top of each other. This is confirmed by the almost zero relative errors in Table V.10. We will use $IT_{start} = 10$ in the following simulations.

IT_{start}	Averaging start (iteration)	Averaging end (iteration)	$\langle C_T \rangle$	$\langle C_P \rangle$	Relative change $\langle C_T \rangle$	Relative change $\langle C_P \rangle$
1	250	350	-1.048E-02	-1.816E-03		
	350	450	-1.052E-02	-1.786E-03		
10	250	350	-1.048E-02	-1.816E-03	0.00%	0.00%
	350	450	-1.051E-02	-1.786E-03	-0.01%	0.00%
20	250	350	-1.048E-02	-1.815E-03	0.02%	-0.01%
	350	450	-1.052E-02	-1.786E-03	0.03%	-0.01%

Table V.10: Averaged mean coefficients of thrust and power for different IT_{start}. The relative change is computed for an increase in the number of iterations.

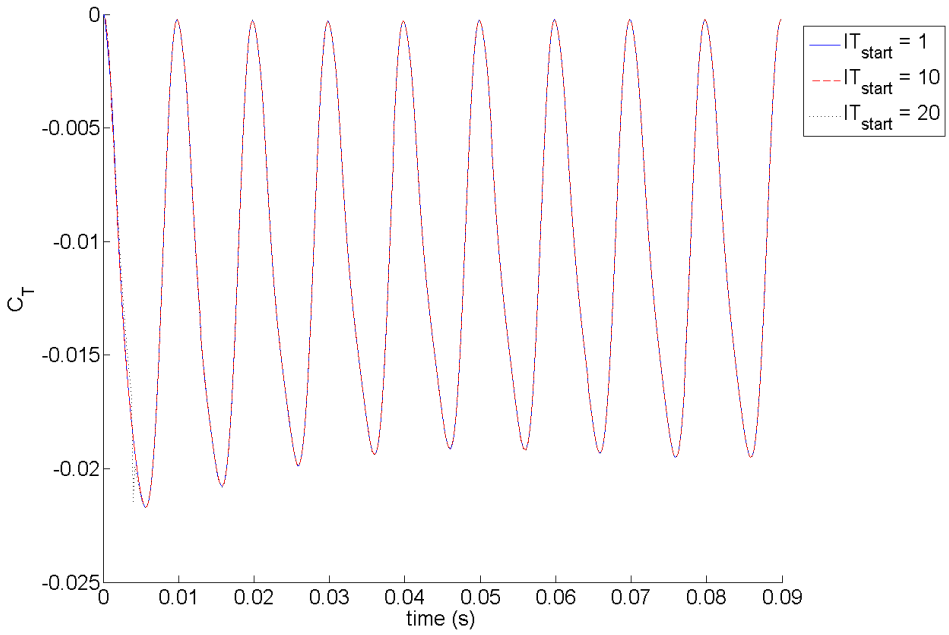

Figure V.22: Coefficient of thrust in hover for a wing in test configuration for different number of iterations with the freestream on (IT_{start}).

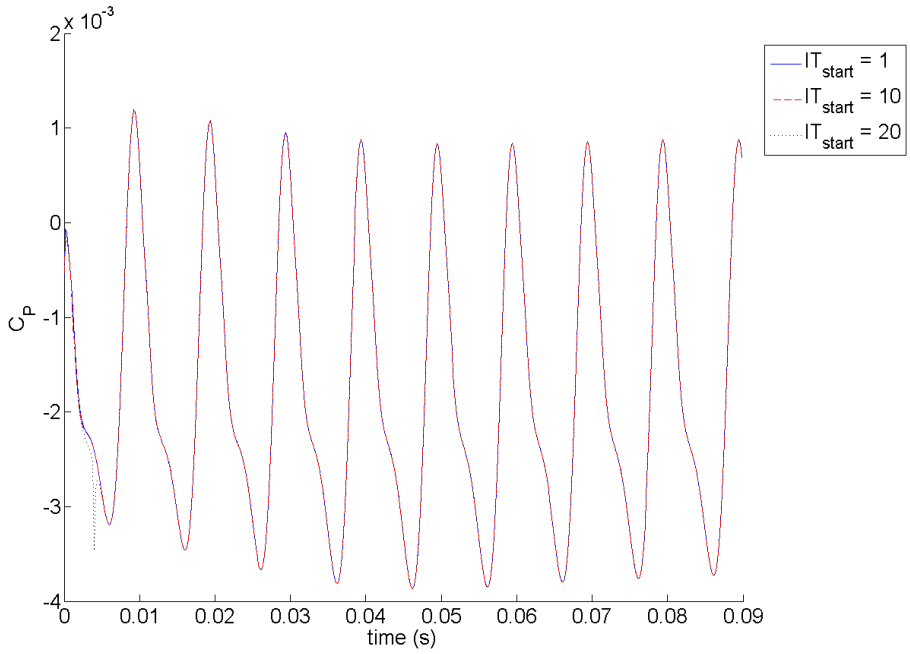

Figure V.23: Coefficient of power in hover for a wing in test configuration for different number of iterations with the freestream on (IT_{start}).

c.6 Time step

In this section, we will look at the influence of the time discretization on the mean aerodynamic coefficients. As seen in Figure V.24 and Figure V.25, after 2 cycles, the curves seem to be almost on top of each other. In addition, in Table V.11 we can see that the relative error remains small. The small error can not only be explained by the influence of the time step in the computation of the aerodynamic forces but also in the averaging. When the time step is smaller, the mean values are computed by averaging a larger number of data points. Nevertheless, it already takes 18 hours to run 450 iterations and a few days to run 900 iterations. Consequently 100 points per cycle will be used in the present method.

NTS	Averaging start (iteration)	Averaging end (iteration)	$\langle C_T \rangle$	$\langle C_P \rangle$	Relative change $\langle C_T \rangle$	Relative change $\langle C_P \rangle$
100	250	350	-1.048E-02	-1.816E-03		
	350	450	-1.051E-02	-1.786E-03		
133	333	466	-1.038E-02	-1.823E-03	-0.95%	0.39%
	467	600	-1.037E-02	-1.819E-03	-1.33%	1.85%
200	500	700	-1.009E-02	-1.828E-03	-2.83%	0.27%
	700	900	-1.014E-02	-1.821E-03	-2.22%	0.09%

Table V.11: Averaged mean coefficients of thrust and power for different NTS. The relative change is computed for an increase in NTS.

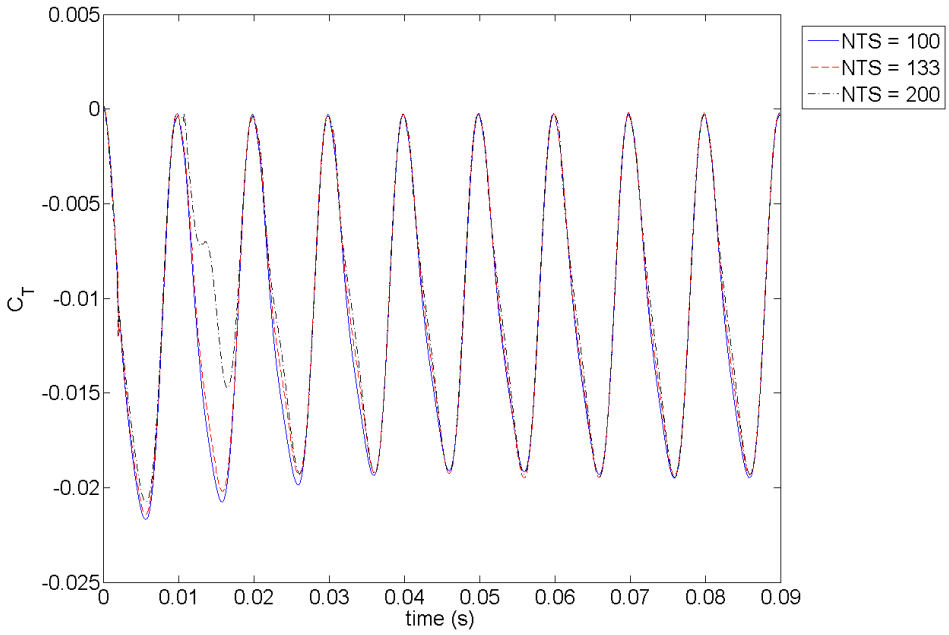

Figure V.24: Coefficient of thrust in hover for a wing in test configuration for different number of iterations per cycle (NTS).

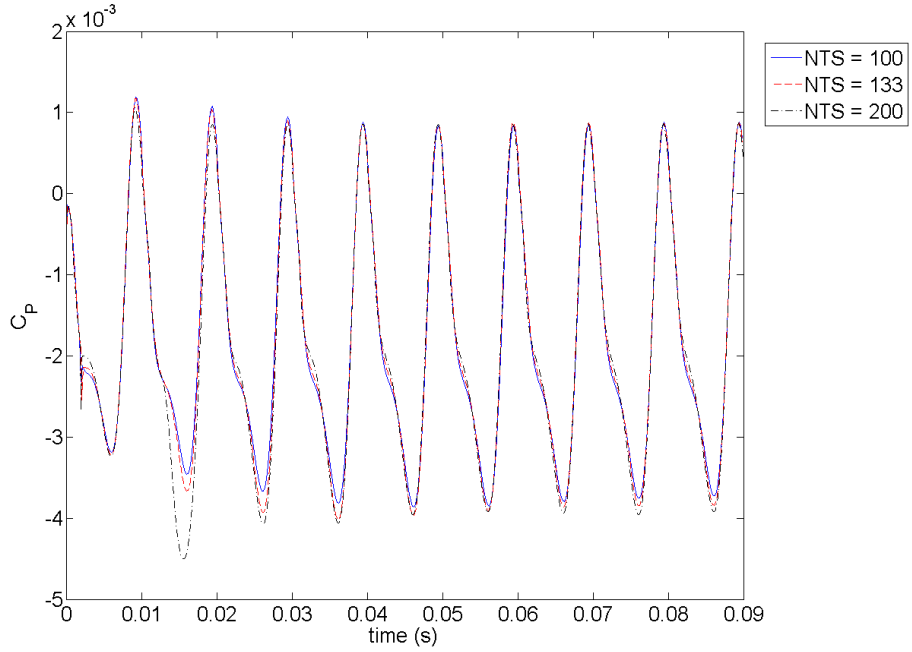

Figure V.25: Coefficient of power in hover for a wing in test configuration for different number of iterations per cycle (NTS).

c.7 Number of panels in the chordwise direction

Finally, we looked at the influence of the number of panels in the chordwise direction. As seen in Figure V.26 and Figure V.27, increasing the number of panels from 40 to 60 does not change the solution. This is confirmed by Table V.12, where the relative error is less than half a percent.

N_i	Averaging start (iteration)	Averaging end (iteration)	$\langle C_T \rangle$	$\langle C_P \rangle$	Relative change $\langle C_T \rangle$	Relative change $\langle C_P \rangle$
40	250	350	-1.048E-02	-1.816E-03		
	350	450	-1.052E-02	-1.786E-03		
60	250	350	-1.050E-02	-1.823E-03	0.21%	0.41%
	350	450	-1.054E-02	-1.795E-03	0.22%	0.46%

Table V.12: Averaged mean coefficients of thrust and power for different N_i. The relative change is computed for an increase in the number of panels.

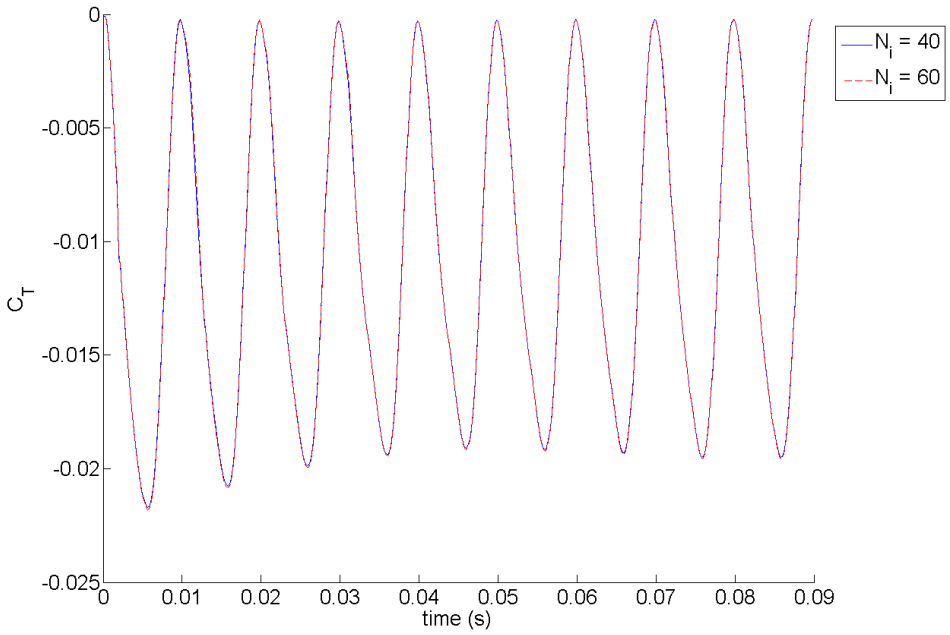

Figure V.26: Coefficient of thrust in hover for a wing in test configuration for different number of panels in the chordwise direction (N_i).

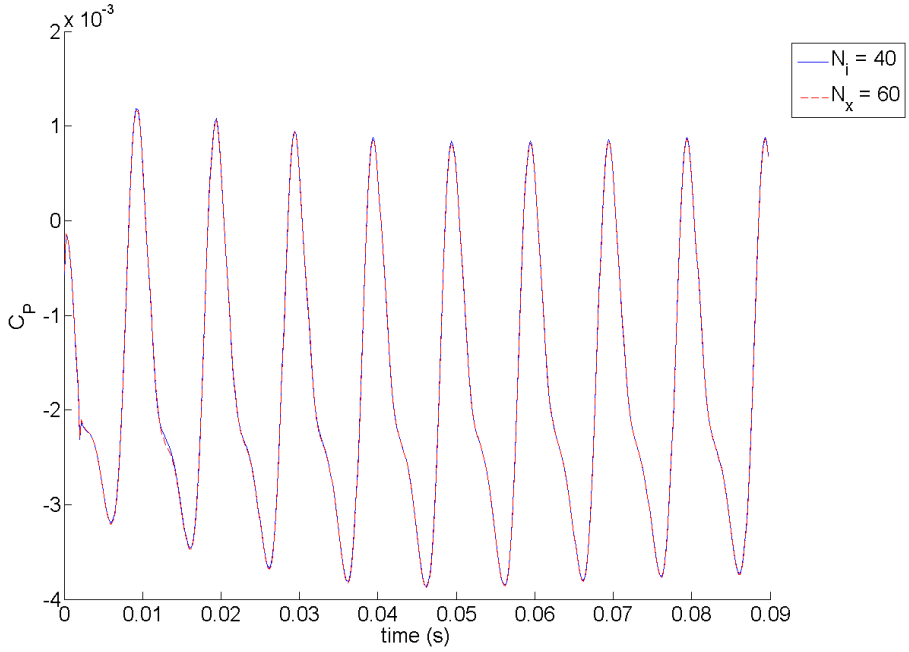

Figure V.27: Coefficient of power in hover for a wing in test configuration for different number of panels in the chordwise direction (N_i).

c.8 Number of panels in the spanwise direction

In the same way, we looked at the influence of the number of panels in the spanwise direction. As seen in Figure V.28 and Figure V.29, increasing the number of panels in the spanwise direction on a half-wing from 20 to 30 does not change the solution. This is confirmed by Table V.13, where the relative error is small.

N_j	Averaging start (iteration)	Averaging end (iteration)	$\langle C_T \rangle$	$\langle C_P \rangle$	Relative change $\langle C_T \rangle$	Relative change $\langle C_P \rangle$
20	250	350	-1.048E-02	-1.816E-03		
	350	450	-1.052E-02	-1.786E-03		
30	250	350	-1.039E-02	-1.818E-03	-0.86%	0.13%
	350	450	-1.040E-02	-1.793E-03	-1.06%	0.36%

Table V.13: Averaged mean coefficients of thrust and power for different N_j. The relative change is computed for an increase in the number of panels.

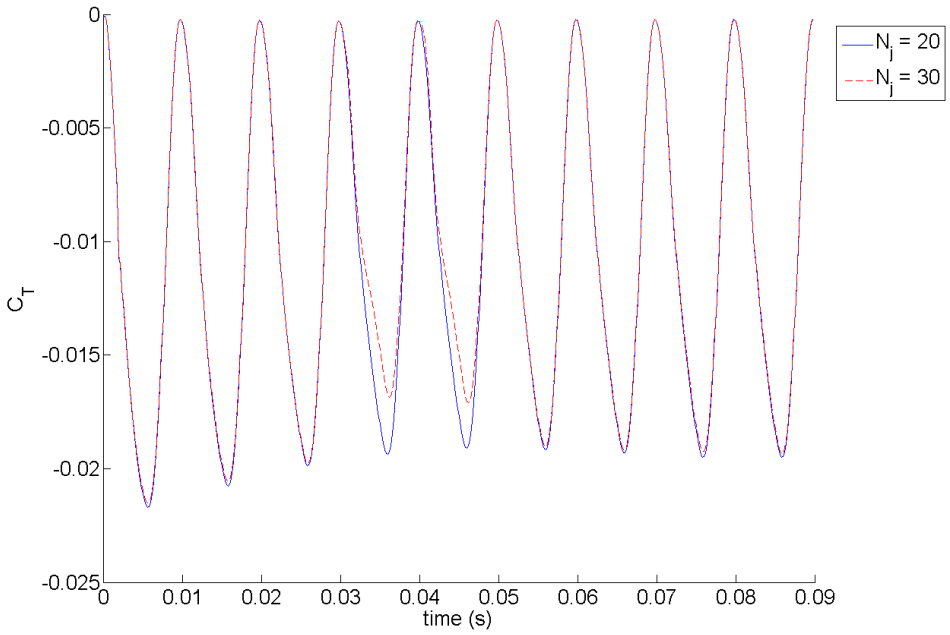

Figure V.28: Coefficient of thrust in hover for a wing in test configuration for different number of panels in the spanwise direction (N_j).

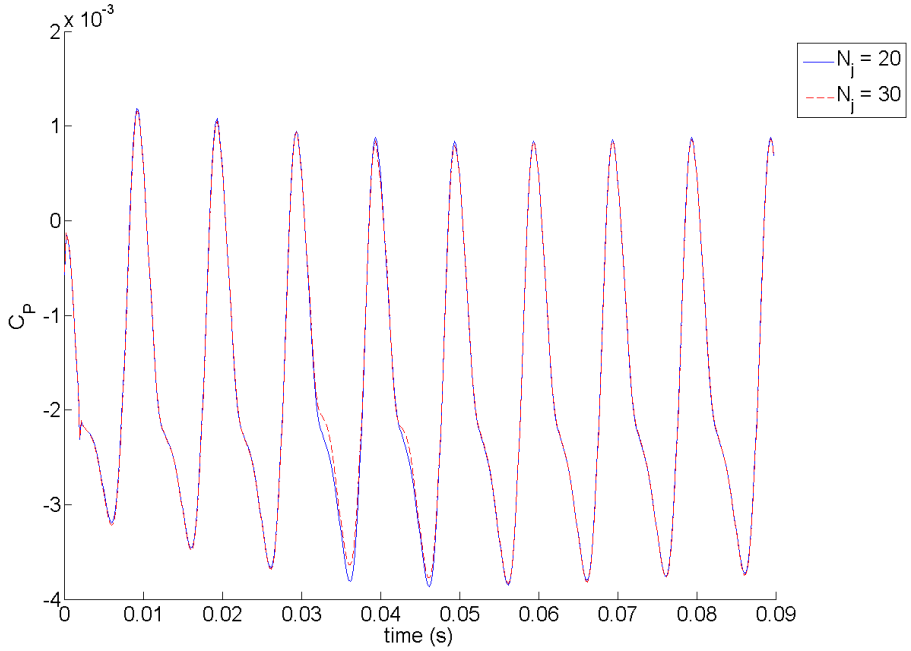

Figure V.29: Coefficient of power in hover for a wing in test configuration for different number of panels in the spanwise direction (N_j).

c.9 Parameters used

To conclude, we saw that convergence was reached for all the parameters used in the present method to simulate hovering flapping flight. We will use the following parameters in all the simulations:

- 4.5 cycles computed and averaging over the last cycle.
- $\sigma_K = 15$.
- $\epsilon_K = 0.296$.
- $k_{start} = 4.19$ over the first 10 iterations.
- 100 iterations per cycle.
- $N_i = 40$.
- $N_j = 20$.

.

V.4 Results

The goal remains the same as in the previous chapter. For a required thrust, we want to find the motion with the least aerodynamic power. We use the same wing configuration as in the previous section.

V.4.1 Inviscid case

a Optimum motion

In this section, surface plots of the figure of merit and the corresponding non-dimensional frequency as a function of the pitch angle and stroke angle will be presented for the inviscid

case. The optimum motion will be deduced from these surface plots. The figure of merit (FOM) was defined previously as

$$\begin{aligned} FOM &= \left(\frac{P}{T^{3/2}}\right)_{Actuator} \Big/ \left(\frac{P}{T^{3/2}}\right) \\ FOM &= \frac{1}{\frac{P}{T^{3/2}}\sqrt{2\rho A}} \end{aligned} \tag{V.44}$$

where A is the area covered by the flapping wing. The non dimensional-frequency ($\tilde{f}$) is defined as

$$\tilde{f} = f\frac{2\pi}{\sqrt{\frac{T}{2\rho c^3 B}}} \tag{V.45}$$

In Figure V.30, the figure of merit is plotted as a function of the pitch angle and the pitch phase advance for a required thrust. The white region corresponds to a region where the present method could not converge. Nevertheless, it is not of importance since in this region the figure of merit seems to be really low. The optimum region is located in the upper right corner of the figure. The optimum motion is obtained for a phase angle of $\frac{\pi}{2}$ and a pitch angle of 65° and a non-dimensional flapping frequency of 0.97, the corresponding aerodynamic coefficients are

$$FOM = 0.76$$

$$C_T = 8.53 \times 10^{-3}$$

$$C_P = 1.17 \times 10^{-3}$$

This motion is close to the motion found with the two-dimensional method. The phase angle is the same, however, the pitch angle is higher in the three-dimensional case. This can possibly be explained by the fact that the figure of merit in the two-dimensional case was obtained by extrapolating the thrust generated by a section of the wing to the entire wing. The value of the maximum figure of merit is really close to the maximum found in two-dimensions (0.74).

In addition, the motion is close to the usual kinematics ("figure of 8" motion) found in flappers during hover. The motion is also close to the "clap-fling" mechanism. At the end of the upstroke, the two wings are close to each other and parallel. At the beginning of the downstroke they start to pitch and form an opened book. Results of the present method would confirm the thrust enhancement of this mechanism.

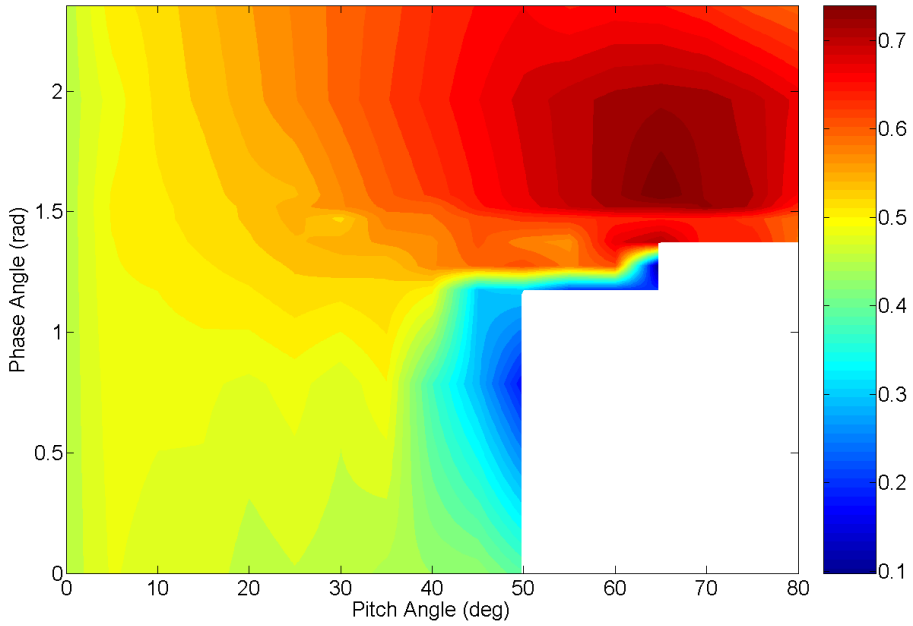

Figure V.30: *FOM* for a required coefficient of thrust function of the pitch angle and the pitch phase advance in the inviscid case.

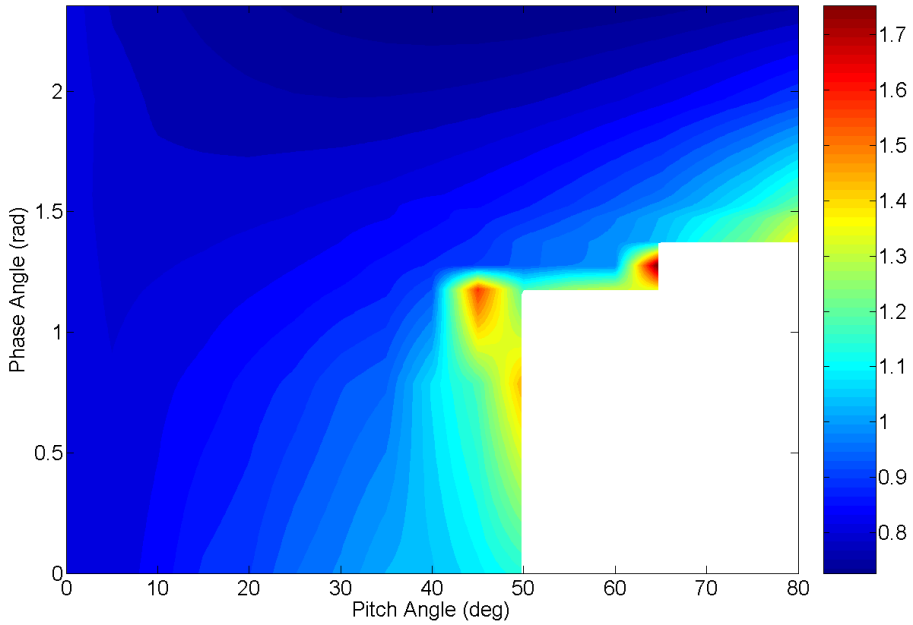

Figure V.31: Flapping frequency for a required coefficient of thrust function of the pitch angle and the pitch phase advance in the inviscid case.

It is also interesting to compare this result to the result of the method developed by Hall et al. To do so, Hall's method was modified to include the gap that exists between the two half-wings. In addition, Hall's method is based on the motion of the trailing edge and not on the entire motion of the wing. Consequently, we used the exact same motion of the trailing edge in Hall's method as the optimum motion found with the present method. In these conditions, Hall's method provides a figure of merit of 0.66 which is 13% lower than the figure of merit of the present method. Even though the two methods are based on different assumptions, both methods give similar answers. The advantage of Hall's method is its computing time. It only takes a few minutes to get the answer, while in the present method, it takes a few hours. Nevertheless, Hall's method is entirely based on the trailing edge motion, thus it is necessary to use the present theory to know the exact motion of the wing that gives the best aerodynamic performance.

Another interesting comparison would be to look at the shed circulation. Hall's method is based on the circulation in the wake. Consequently we plot the non-dimensional shed circulation ($\frac{\Gamma}{B^2\omega}$) function of the non-dimensional time for one converged flapping period across the non-dimensional span (B/c). As seen in Figure V.32, the circulation is sinusoidal, while in Figure V.33 , it has the double local maxima feature already observed previously. The differences are clearer in the contour plots (Figure V.34 and Figure V.35). First of all, we can see that the circulation in the free wake case is shifted in time compared to the circulation computed with Hall's method. This lag could be explained by the nature of the two wakes. In the free wake case, the wake seems to roll first and is then convected; while in the frozen wake case, this one is always convected at the same speed. The roll-up seems to introduce a lag in the peak circulation. The values of the peaks are also slightly different. These differences could explain the differences in the figures of merit. Nevertheless, by considering that the two methods are based on different approximations, the shape of the contour remains surprisingly similar.

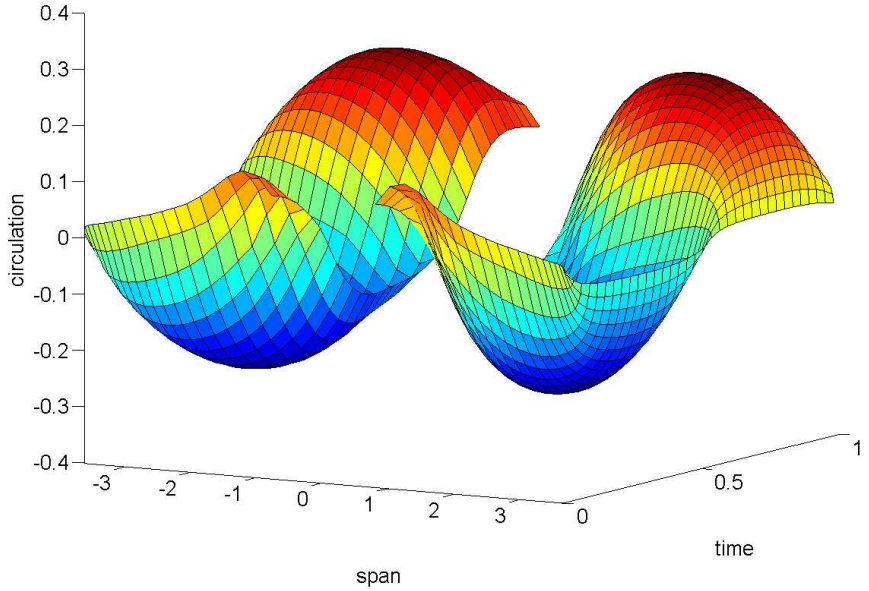

Figure V.32: Non-dimensional shed circulation for one converged flapping period along the non-dimensional span using Hall's method.

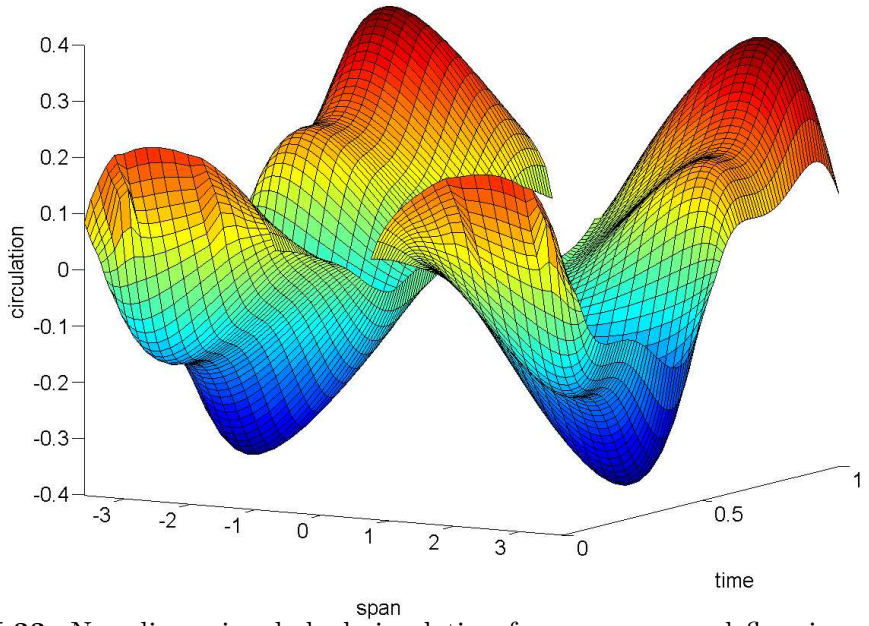

Figure V.33: Non-dimensional shed circulation for one converged flapping period along the non-dimensional span using the present method.

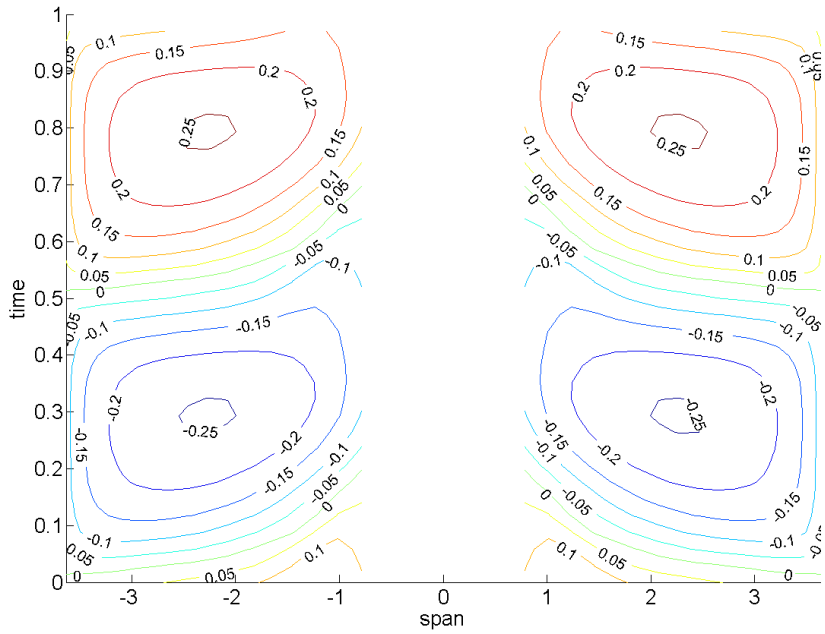

Figure V.34: Contour plot of the non-dimensional shed circulation for one converged flapping period along the non-dimensional span using Hall's method.

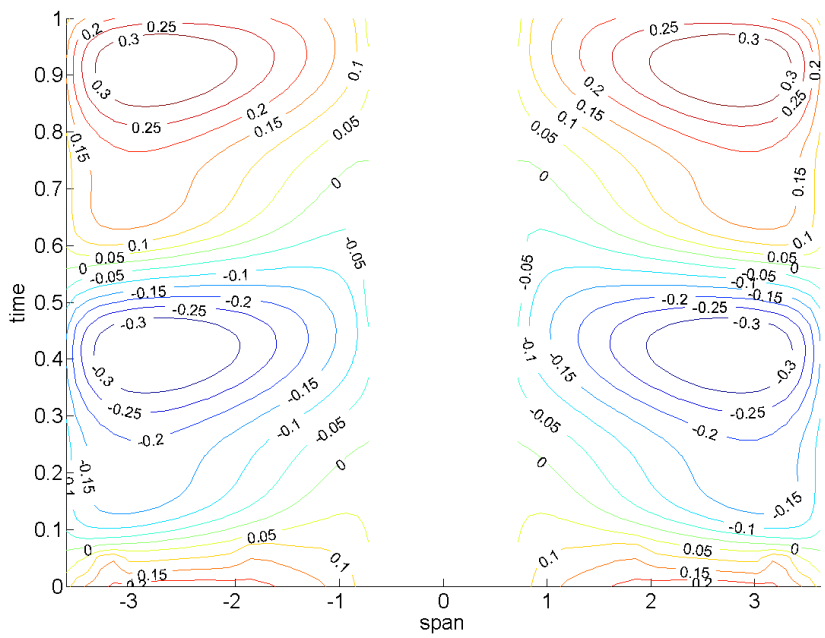

Figure V.35: Contour plot of the non-dimensional shed circulation for one converged flapping period along the non-dimensional span using the present method.

Finally, it is also possible to compare the speed at which the wake is convected in the present method to the convection speed provided by the actuator disk theory. The actuator disk theory gives a speed $U_{\text{actuator}} = \sqrt{\frac{T}{\frac{1}{2}\rho\pi B^2 \frac{\phi}{\pi}}}$. With the present method, the convection speed is directly read in Figure V.36. For one period the length of the wake is $2.90c$, consequently the convection speed is

$$U_{\text{method}} = \frac{2.90c}{1/f} \tag{V.46}$$

By using Equation V.46, we get

$$U_{\text{method}} = \frac{2.90c}{2\pi}\tilde{f}\sqrt{\frac{T}{2\rho c^3 B}} \tag{V.47}$$

We can now compute the ratio ($\tilde{U} = U_{\text{method}}/U_{\text{actuator}}$),

$$\tilde{U} = \frac{2.90\tilde{f}}{2\pi}\sqrt{\frac{\pi AR\frac{\phi}{\pi}}{4}} \tag{V.48}$$

By replacing $\tilde{f} = 0.97$, $AR = 6$, $\phi = 150°$, we get $\tilde{U} = 0.886$, which means that the convection speed provided by the actuator disk theory is 13% higher than the convection speed in the present method. This difference is the same as the difference in the FOM. In addition, we notice that the speed at which the wake is convected in the free wake case is lower than the speed given by the actuator disk theory. This confirms the explanation concerning the presence of a lag in the circulation.

To summarize, we saw that the three-dimensional method provides an optimum motion that is really similar to the motion actual birds use. In the next section, we will present a comparative study between the present method and the work of Ramamurti and Sandberg [13] on a *Drosophila* wing.

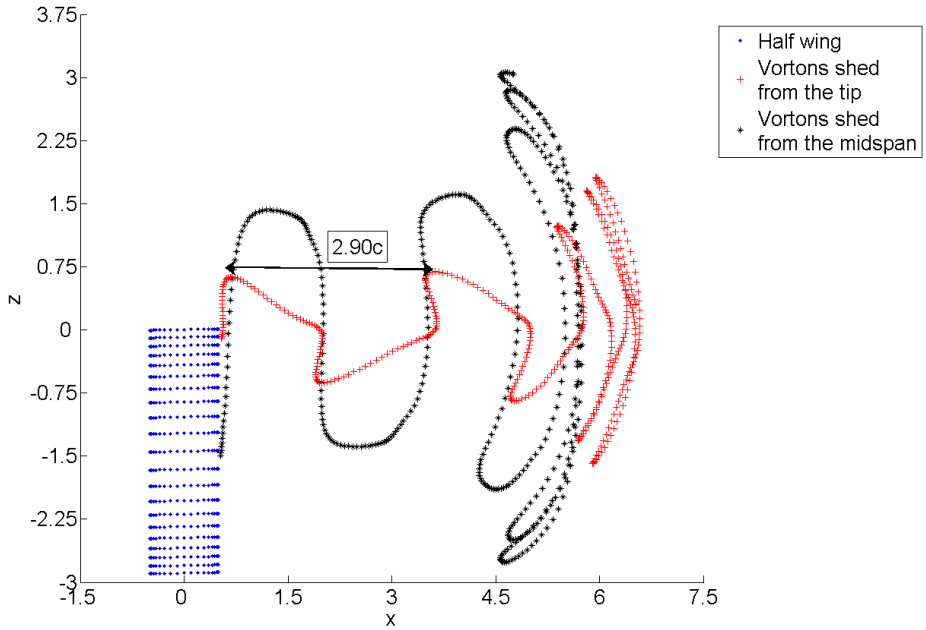

Figure V.36: Top view of the half wing and the vortons shed from the tip and midspan in the optimum motion case, for a non-dimensional flapping frequency of 0.97.

b Comparative study

In this section, I will compare results provided by the present method to results of Ramamurti and Sandberg [13]. Ramamurti and Sandberg [13] studied the idealized motion of one *Drosophila* wing. They used a full Navier-Stokes method to compute the unsteady flow past a three-dimensional *Drosophila* wing undergoing flapping motion in hover. They also compared their results to experimental results of Dickinson et al. [14]. First, I will present the wing model and kinematics they used compared to the wing and kinematics we used.

Ramamurti and Sandberg used a wing derived from the *Drosophila*. Its span seminspan R is $25cm$, thickness is $3.2mm$ and mean chord $\bar{c}$ is $6.7cm$. The wing is undergoing flapping and pitching motion at a frequency of $0.145Hz$. The stroke angle ϕ is $160°$ and the pitch angle is $50°$ with a phase angle of $\pi/2$. The pitch axis is located at $0.2c$ from the leading edge. This flapping mode is called symmetrical. Figure V.37 represents the wing modeled by Ramamurti and Sandberg.

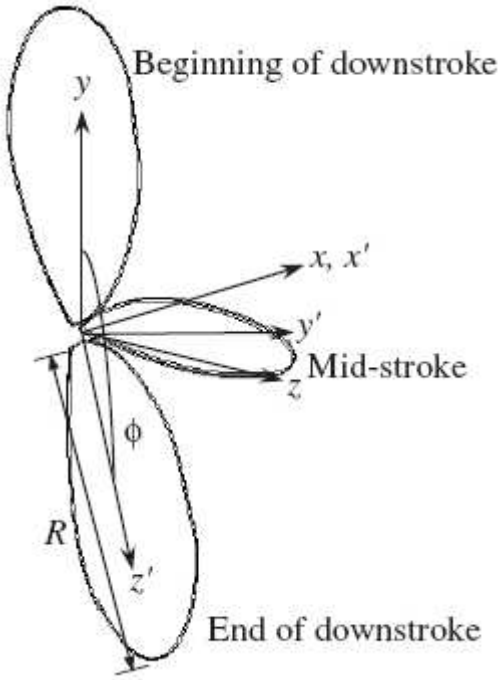

Figure V.37: "Schematic diagram of the flapping *Drosophila* wing. The position of the wing is shown at three different times during the flapping cycle. The coordinate system $(x', y'z')$ is fixed to the wing, and the wing rotates about the z' axis throughout the cycle. R wing length; ϕ wingbeat amplitude." Reprinted from Ramamurti and Sandberg [13]

The simulation was done with mineral oil, thus the Reynolds number based on the mean chord and mean wing-tip velocity U_t was 136, which matches the actual Reynolds number of a typical *Drosophila melanogaster*. The kinematics used by the authors is obtained from the experiments of Dickinson et al. [14] and is plotted in Figure V.38.

In the vortex method, we use a rectangular wing of span $25cm$ and chord of $6.7cm$. The authors did not detail the exact kinematics used in their study. Consequently, we approximated their kinematics. It is represented in Figure V.38.

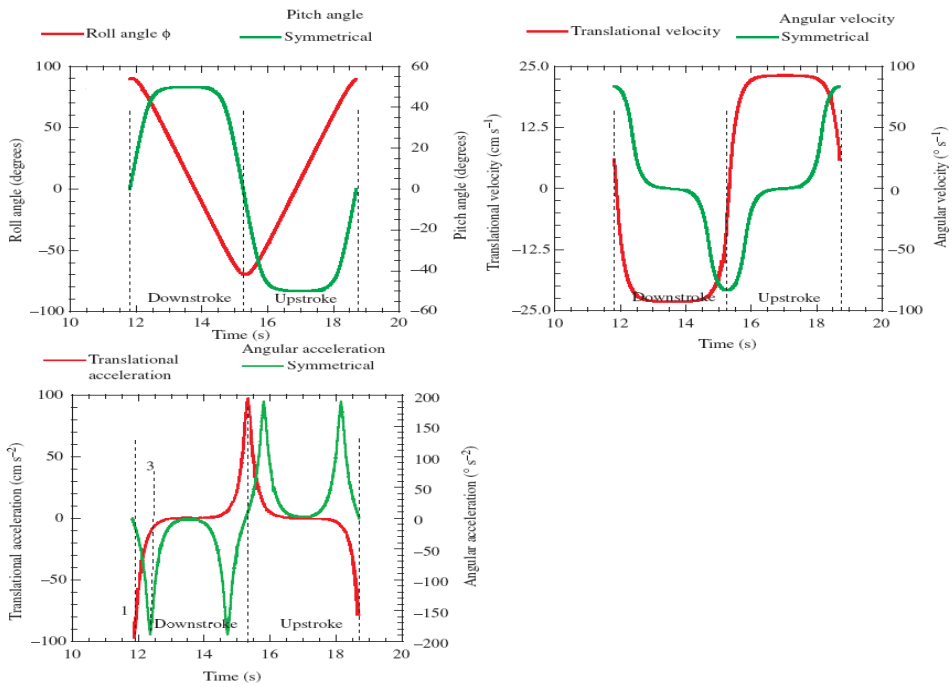

Figure V.38: Kinematics of the flapping wing used by Ramamurti and Sandberg. From left to right, stroke and pitch angle; translational velocity of the wing tip and angular velocity; translational acceleration of the wing tip and angular acceleration as functions of time. Reprinted from Ramamurti and Sandberg [13].

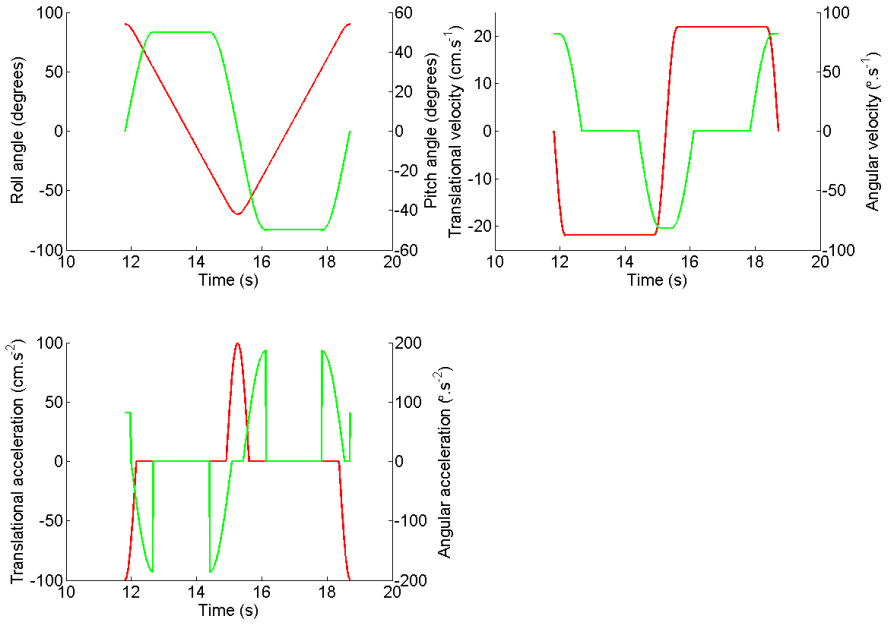

Figure V.39: Kinematics of the flapping wing used in the present method. From left to right, stroke and pitch angle; translational velocity of the wing tip and angular velocity; translational acceleration of the wing tip and angular acceleration as functions of time.

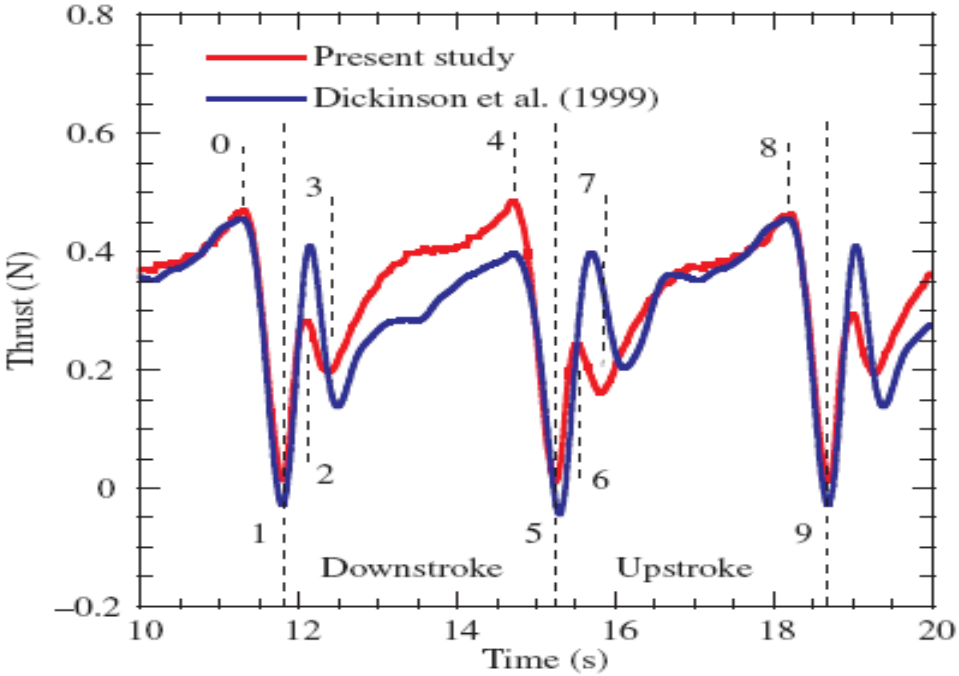

Figure V.40: Thrust as a function of time for one flapping period. The red lines are from Ramamurti and Sandberg [13] and the blue lines from Dickinson et al. [14]. Reprinted from Ramamurti and Sandberg [13].

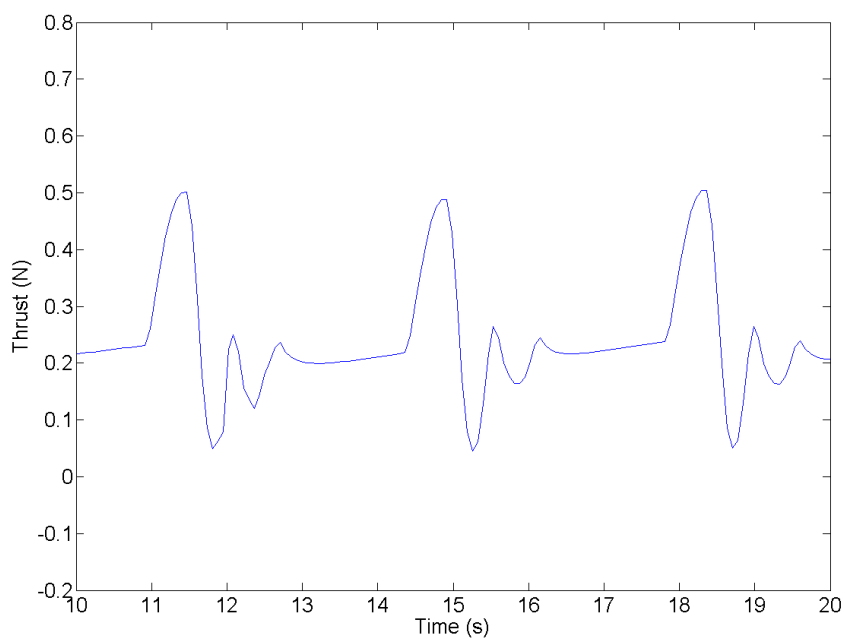

Figure V.41: Thrust as a function of time for one flapping period using the present method.

Ramamurti and Sandberg computed the unsteady solution of the motion described previously. Their computation was carried out for five cycles and the thrust was computed by integration of the surface pressure. They also compared the thrust they obtained to the thrust obtained by Dickinson et al. [14] with his *Drosophila* model. Figure V.40 shows their computed thrust over one cycle as a function of time. The kinematics of the wing can be decomposed into two rotational phases that occur at the end of each half-stroke and two translational phases that occur in between. As seen in Figure V.40, Ramamurti and Sandberg decomposed one stroke into nine intervals ranging from time t_0 to time t_9. From time t_0 to t_1, the thrust decreases. This phase occurs at the end of the upstroke, the wing translates in the $-z$ direction creating a positive thrust, however the translational velocity decreases which causes the thrust to decrease. At the end of the upstroke at time t_1, the wing is in the (x, y) plane. During the period $t_1 - t_2$, the thrust increases. This can be explained by two phenomenon, first the translational velocity starts to increase in the $+z$ direction, nevertheless this acceleration itself is still small at the beginning of the downstroke to explain itself this increase of thrust. Another explanation for this increase of thrust consists of the clap and fling mechanism explained earlier in which the wing captures the shed vorticity of the previous stroke. During the phase $t_2 - t_3$, the thrust decreases, the rotational acceleration becomes large enough to negate some of the translational acceleration resulting in a decrease in the thrust. Between time t_3 and t_4, the translational acceleration is almost constant which should result in a constant thrust. Nevertheless, we can see that the thrust increases, this is explained by the rotational effect. We can notice the presence of a plateau that occurs when the rotational velocity changes sign corresponding to the moment when the trailing edge vortex is shed. During the second half of $t_3 - t_4$, the thrust keeps increasing because the rotation is now in the clockwise direction thus increasing the effect of the translational velocity in the $+z$ direction. Each stroke being symmetrical, the period $t_5 - t_9$ is explained by the exact same reasons.

We can notice in Figure V.41 that the plot of the thrust as a function of time using the present method is similar to the thrust obtained by Ramamurti and Sandberg. The value of

the peaks at times t_4 and t_8 are close on both plots. The peaks at times t_2 and t_6 are higher in the Ramamurti and Sandberg's study than in the present method. The main difference occurs during the period $t_3 - t_4$. The thrust obtained with the present method is almost constant. We already mentioned that with only the effect of translation, the thrust should be constant during this period, however in the case of Ramamurti and Sandberg, the thrust is enhanced by the rotational effect. By looking closely to the kinematics we used, we notice that the rotational acceleration during that period is null, the pitch angle remains constant. Thus in our case, the thrust is not increased by the rotational effects since the wing does not rotate. However, when the wing starts to rotate, we observe an important increase in the thrust. This increase is sharper than in Ramamurti and Sandberg's case because the rotational acceleration is discontinuous and sharply increases in our case. Consequently, the mean thrust in the present method is lower than the mean thrust obtained by Ramamurti and Sandberg.

Nevertheless, the present model agrees surprisingly well with the results of Ramamurti and Sandberg even though the leading edge vortex is not modeled in our case and we used a rectangular wing and not a real *Drosophila* wing model. In addition, Ramamurti and Sandberg [13] showed that the viscous effects in this case were practically inexistent. As seen in Figure V.42, the thrust as a function of time in the viscous and inviscid case are the same. This justifies the use of an inviscid model in the case of highly accelerated flows.

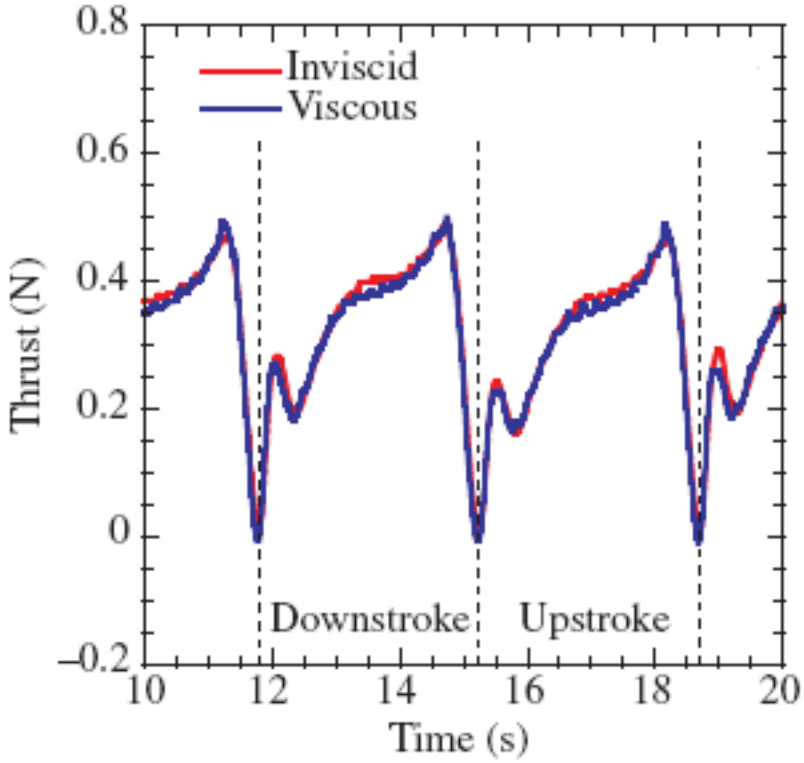

Figure V.42: Thrust as a function of time for one symmetrical flapping cycle in the inviscid case and in the viscous case computed by Ramamurti and Sandberg [13]. Reprinted from Ramamurti and Sandberg [13].

V.4.2 Viscous model 2

To model the effects of viscosity, we use a similar viscous model as in two-dimensions. Equation V.37 represents the corrective terms for the force and power. To fully compute the effect of viscosity, we need to add a drag model. In this case, the viscous model used is based on a constant drag coefficient using the data collected by Weis-Fogh [32]. We use the same drag coefficient ($C_D = 0.12$) and method as in the two-dimensional case.

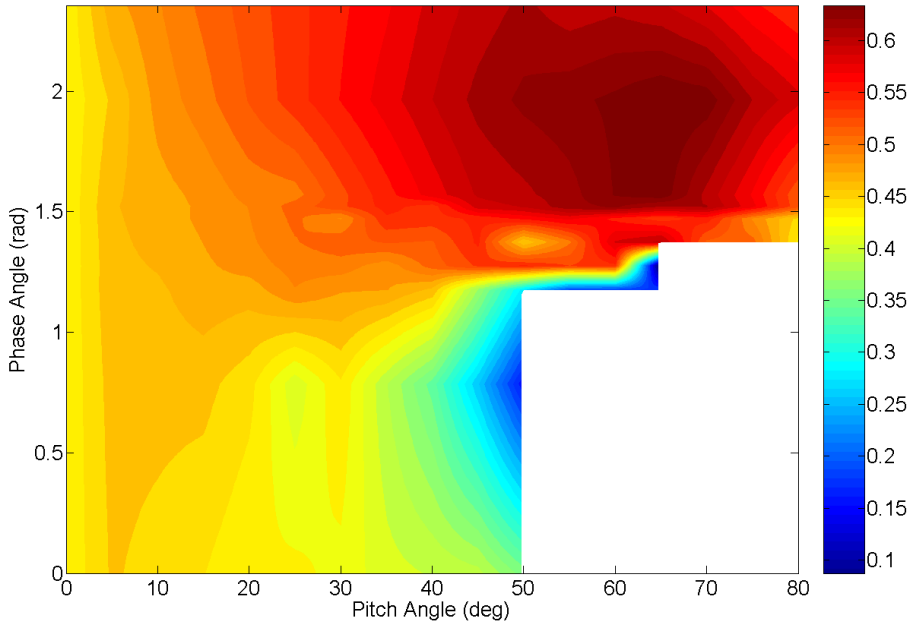

Figure V.43: *FOM* for a required coefficient of thrust function of the pitch angle and the pitch phase advance in the viscous 2 case.

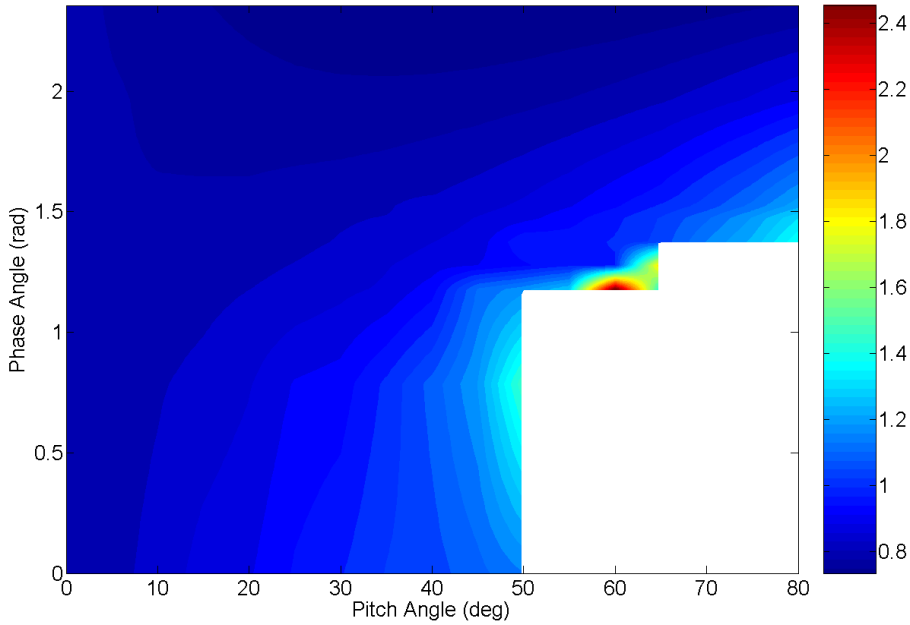

Figure V.44: Flapping frequency for a required coefficient of thrust function of the pitch angle and the pitch phase advance in the viscous 2 case.

The optimum motion is found by ploting the contour of the figure of merit. In Figure V.43, we can notice that the optimum region is almost unchanged. The optimum motion is slightly different, the phase angle is now $\frac{5\pi}{8}$ and the pitch angle remains 65°. The non-dimensional flapping frequency is 0.835. For this motion, we have the following aerodynamic coefficients

$$FOM = 0.65$$
$$C_T = 1.15 \times 10^{-2}$$
$$C_P = 2.13 \times 10^{-3}$$

The figure of merit is logically lower than in the inviscid case (14.5% lower). This order of magnitude is in agreement with the two-dimensional case and with the findings of Wells [27]. He showed that the viscous power was lower than the induced power by a factor of 3.5. The small change in the kinematics is explained by the fact that for this new phase angle, the flapping frequency required to generate the thrust is lower than with a phase angle of $\frac{\pi}{2}$. In the viscous case, the lower the flapping frequency is; the lower the viscous drag and losses are. The drag scales like f^2 and the power like f^3.

It is possible to draw the same conclusions as in the previous chapter. Adding a viscous model lowers the figure of merit since it adds viscous losses. Nevertheless, the optimum motion is a little changed compared to the optimum motion in the inviscid case. This behavior reflects what Hamdani et al. [7] observed. They found that for large accelerated flows, the viscous effects had a limited influence on the aerodynamic coefficients. In a large accelerated flow, which is the case in our simulation, inviscid effects are predominant.

This viscous model remains limited. It does not take into account the unsteadiness of the flow and especially neglect the importance of the leading edge vortex.

Chapter VI

Conclusion and Recommendations

VI.1 Conclusion

To conclude, in this thesis, we have presented different methods to analyze flapping flight with an emphasis on hovering flapping flight.

The first method presented was developed by Hall et al. It is a three-dimensional potential method using a frozen wake, that gives the optimal circulation distribution in the wake for a given trailing edge motion and a required force. In addition, viscous losses are estimated using a steady drag polar model. We also added a chord optimization routine. It provides the shape of the wing that minimizes the total power. In hovering flight, the wake is shed at a speed given by the actuator disk theory. Nevertheless, this model is valid for lightly loaded wings because it neglects the induced velocity of the wake on itself. In addition, it does not reflect the full motion of the wing but only its trailing edge.

Consequently, a two-dimensional potential method using a free wake was developed. For a given kinematics, the method gives the forces generated and the power required. A similar steady drag polar viscous model is used. In a second step, we used a two degrees of freedom model (plunging and pitching motion) to find an optimal motion. We created surface plots of the figure of merit function of the pitch angle and phase shift between the plunge and pitch. This surface plot shows the existence of an optimum motion. The value of the FOM found for the optimum motion agrees well with the value provided by Hall's method. The comparaison to Hall's results also showed the importance of the three-dimensional effects. For low aspect ratios the figure of merit in the same kinematics conditions is lower than for high aspect ratios. Consequently, the principal limitation of the model is its two-dimensionality. Three-dimensional effects become especially important in the case of hovering MAVs.

Thus, we developed a three-dimensional potential method using vortons in the wake. The same analysis as in the two-dimensional case was performed. The optimum motion was also similar to two-dimensional motion. The phase angle for the optimum motion is $\frac{\pi}{2}$. The motion resulting from that optimum is similar to the typical "figure of 8" motion found in hovering birds. The fact that at the end of each stroke, the wings are paralel and then open like a book seems to prove that the motion takes advantage of the clap and fling phenomenon. In addition, it showed surprisingly good agreements with the method developed by Hall et al. The surface plots of the shed circulation using both methods had some similarities; the main difference being the presence of a time lag in the vorton method. This lag was explained by the roll-up of the wake occuring in the vorton method and not in Hall's method. The present method also agreed to some extend with the evolution in time of the thrust of a single wing of a *Drosophila* simulated by Ramamurti and Sandberg [13] with their unsteady Navier-Stokes method.

Finally, in various studies (Wells [27], Hamdanim [7] and Ramamurti [13]), it was showed that the effects of viscosity were limited in the case of highly accelerated flows.

VI.2 Further research

A first interesting study that should be conducted is the increase of the number of harmonics used in the kinematics of the wing. We used a single harmonic and should now conduct the same study with more harmonics to find a better optimum motion.

Another improvement would be to add the influence of the viscosity. Even though studies show that in hovering, induced power is greater by a factor of 3.5 than viscous losses; the role of the leading-edge vortex in delaying the onset of stall seems important. The methods developed do not reflect the leading-edge separation since they are inviscid methods. The vortex method can be modified to include the effect of viscosity. For example a separation line could be adding near the leading edge. The intensity of shedding could be found using an ONERA model.

Few aeroelastic studies have been conducted on flapping flight. Another improvement would be to add the coupling of the structure response to the aerodynamic excitation. This coupling could be investigated and would lead to a design of actively controlled wings.

Appendix A

Flow relations

A.1 Potential flow identity

The second form of Green's theorem gives us

$$\int\int\int_V \left(\phi_1 \nabla^2 \phi_2 - \phi_2 \nabla^2 \phi_1\right) dV = -\int\int_A \left(\phi_1 \vec{\nabla} \phi_2 - \phi_2 \vec{\nabla} \phi_1\right) \cdot \vec{n} dA \tag{A.1}$$

If we take $\phi_1 = \phi, \phi_2 = \delta\phi$, we have

$$\int\int\int_V \left(\phi \nabla^2 \delta\phi - \delta\phi \nabla^2 \phi\right) dV = -\int\int_A \left(\phi \vec{\nabla} \delta\phi - \delta\phi \vec{\nabla} \phi\right) \cdot \vec{n} dA \tag{A.2}$$

Since ϕ satisfies the Laplace's equation, the left-hand side of Equation A.2 is 0. Thus we have

$$\int\int_A \left(\phi \vec{\nabla} \delta\phi - \delta\phi \vec{\nabla} \phi\right) \cdot \vec{n} dA = 0 \tag{A.3}$$

Now by using the symmetry properties of ϕ and knowing that the jump in ϕ across the wake is Γ, we get

$$\int\int_W \left(\Gamma \delta\vec{w} - \delta\Gamma \vec{w}\right) \cdot \vec{n} dA = 0 \tag{A.4}$$

A.2 Actuator disk theory

The flow considered is potential and follows Bernoulli's equation. By using Bernoulli's equation on each side of the disk, we have

$$\begin{aligned} P_0 + 0.5\rho V_0^2 &= P_1 + 0.5\rho V_d^2 \\ P_0 + 0.5\rho V_e^2 &= P_2 + 0.5\rho V_d^2 \end{aligned} \tag{A.5}$$

The force applied on the disk is as followed

$$T = A\left(P_2 - P_1\right) = 0.5A\left(V_e^2 - V_0^2\right) \tag{A.6}$$

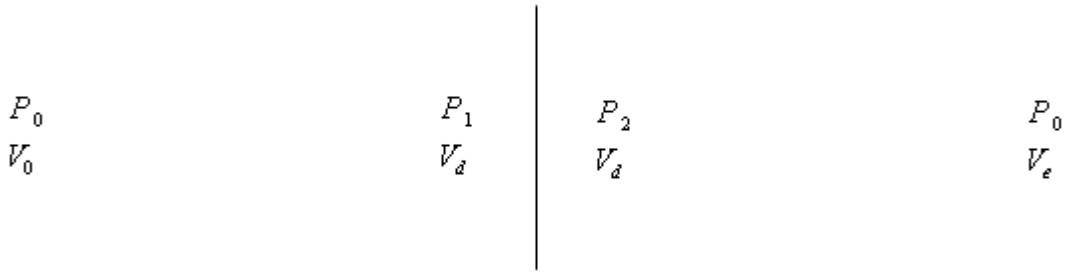

Figure A.1: Actuator disk theory.

In addition the force is also equal to the change in momentum,

$$T = \dot{m}\left(V_e - V_0\right) = \rho A V_d \left(V_e - V_0\right) \tag{A.7}$$

Thus from Equation A.6 and Equation A.7, we get

$$V_d = 0.5\left(V_e + V_0\right) \tag{A.8}$$

Thus in the hover case, $V_0 = 0, V_d = V_h$, we get the thrust

$$T = 2\rho A V_h^2 \tag{A.9}$$

Appendix B

Mathematical methods

B.1 Newton's Method

Newton's method is an iterative method to solve non-linear equations represented as

$$F(x) = 0 \tag{B.1}$$

where $F : \Re^n \rightarrow \Re^n$ is a continuously differentiable function.

The Newton's method starts with an initial guess x^0 for x. At each iteration k we compute the new vector with the following serie,

$$x^{k+1} = x^k - \left[J\left(x^k\right)\right]^{-1} F\left(x^k\right) \tag{B.2}$$

where $\left[J\left(x^k\right)\right]$ is the Jacobian matrix expressed as

$$\left[J\left(x^k\right)\right]_{ij} = \frac{\partial F_i}{\partial x_i}\left(x^k\right) \tag{B.3}$$

Bibliography

[1] H. Tennekes. *The simple science of flight (from insects to jumbo jets).* MIT Press, 1996.

[2] C. J. Pennycuick. Predicting wingbeat freqeuncy and wavelength of birds. *Journal of experimental biology*, 150, 1990.

[3] M. Rosén, G. R. Spedding, and A. Hedenström. The relationship between wingbeat kinematics and vortex wake of a thrush nightingale. *The Journal of Experimental Biology*, 207:14, 2004.

[4] M. H. Dickinson and K. G. Gotz. The wake dynamics and flight forces of the fruit fly drosophila melanogaster. *Journal of experimental biology*, 199, 1996.

[5] S. P. Sane. The aerodynamics of insect flight. *Journal of experimental biology*, 206, 2003.

[6] M. H. Dickinson. The effects of wing rotation on unsteady aerodynamic performance at low reynolds numbers. *Journal of experimental biology*, 192, 1994.

[7] H. Hamdanim and M. Sun. Aerodynamic forces and flow structures of an airfoil in some unsteady motions at small reynolds number. *Acta Mechanica Sinca*, 145, 2000.

[8] J. M. V. Rayner. Mathematical modelling of the avian flight power curve. *Mathematical methods in the applied sciences*, 24, 2001.

[9] K. D. Jones, C. M. Dohring, and M. F. Platzer. Wake structures behind plunging airfoils: a comparison of numerical and experimental results, 1996.

[10] M. F. Platzer and K. D. Jones. The unsteady aerodynamics of flapping-foil propellers, 2000.

[11] D. J. Willis, J. Peraire, and J. K. White. A combined pfft-multipole tree code, unsteady panel method with vortex particle wakes. *International Journal for numerical methods in fluids*, 00, 2000.

[12] J. Katz and A. Plotkin. *Low-Speed Aerodynamics.* Cambridge, 2001.

[13] R. Ramamurti and W. C. Sandberg. A three-dimensional computational study of the aerodynamic mechanisms of insect flight. *Journal of experimental biology*, 205, 2002.

[14] M. H. Dickinson, F-O. Lehmann, and S. Sane. Wing rotation and the aerodynamic basis of insect flight. *Science*, 284, 1999.

[15] T. Theodorsen. General theory of aerodynamic instability and the mechanism of flutter. Technical report, 1935.

[16] I. E. Garrick. Propulsion of a flapping and oscillating airfoil. Technical report, 1937.

[17] W. Shyy, M. Berg, and D. Ljungqvist. Flapping and flexible wings for biological and micro air vehicles. *Progress in Aerospace Sciences*, 35, 1999.

[18] V. A. Tucker. Bird metabolism during flight: evaluation of a theory. *Journal of experimental biology*, 58, 1973.

[19] C. H. Greenewalt. The flight of birds. *Transactions of the American philosophical society*, 65, 1975.

[20] C.J. Pennycuick. Power requirements for horizontal flight in the pigeon columba livia. *Journal of experimental biology*, 49, 1968.

[21] G.R. Spedding, A. Hedenström, and M. Rosén. Quantitative studies of the wakes of freely flying birds in a low-turbulence wind tunnel. *Experiments in Fluids*, 34:13, 2003.

[22] M. H. Dickinson, F-O. Lehmann, and K. G. Gotz. The active control of wing rotation by drosophila. *Journal of experimental biology*, 182, 1993.

[23] G.R. Spedding and P. B. S. Lissaman. Technical aspects of microscale flight systems. *Journal of Avian Biology*, 29, 1998.

[24] D. L. Altshuler, W. B. Dickson, J. T. Vance, S. P. Roberts, and M. H. Dickinson. Short-amplitude high-frequency wing strokes determine the aerodynamics of honeybee flight. *Proceedings of the National Academy of Sciences*, 102, 2005.

[25] D. L. Altshuler and R. Dudley. Kinematics of hovering hummingbird flight along simulated and natural elevational gradients. *Journal of experimental biology*, 206, 2003.

[26] R. Dudley. Extraordinary flight performance of orchid bees (apidae euglossini) hovering in heliox (80 *Journal of experimental biology*, 198, 1994.

[27] D. J. Wells. Muscle performance in hovering hummingbirds. *Journal of experimental biology*, 178, 1993.

[28] P. Chai and D. Millard. Flight and size constraints: hovering performance of large hummingbirds under maximal loading. *Journal of experimental biology*, 200, 1997.

[29] U. M. Norberg, T. H. Kunz, J. F. Steffensen, Y. Winter, and O. von Helversen. The cost of hovering and forward flight in a nectar-feeding bat, glossophaga soricina, estimated from aerodynamic theory. *Journal of experimental biology*, 182, 1993.

[30] S. Mao and D. Gang. Lift and power requirements of hovering insect flight. *Acta Mechanica Sinca*, 19, 2003.

[31] C. R. Betts and R. J. Wootton. Wing shape and flight behaviour in butterflies (lepidoptera, papilionoidea and hesperioidea) a preliminary analysis. *Journal of experimental biology*, 138, 1988.

[32] T. Weis-Fogh. Quick estimates of flight fitness in hovering animals, including novel mechanisms for lift production. *Journal of experimental biology*, 59, 1973.

[33] K. C. Hall and S. R. Hall. Minimum induced power requirements for flapping flight. *Journal of Fluid Mechanics*, 323:21, 1996.

[34] K. C. Hall and S. A. Pigott. Power requirements for large-amplitude flapping flight. *Journal of Aircraft*, 35(3):10, 1998.

[35] U. M. Norberg. *Vertebrate flight: mechanics, physiology, morphology, ecology and evolution*. Springer, 1990.

[36] A. Azuma, S. Azuma, I. Watanabe, and T. Furuta. Flight mechanics of a dragonfly. *Journal of experimental biology*, 116, 1985.

[37] A. Azuma and T. Watanabe. Flight performance of a dragonfly. *Journal of experimental biology*, 137, 1988.

[38] J. M. Wakeling and C. P. Ellington. Dragonfly flight, ii. velocities, accelerations and kinematics of flapping flight. *Journal of experimental biology*, 200, 1997.

[39] B. Singh, M. Ramasamy, I. Chopra, and J. G. Leishman. Insect-based flapping wings for micro hovering air vehicles: experimental investigations, 2004.

[40] M. Sun, J. Wang, and Y. Xiong. Dynamic flight stability of hovering insects. *Acta Mechanica Sinca*, 2007.

[41] C. P. Ellington, C. Van Den Berg, A. P. Willmott, and A. L. R. Thomas. Leading-edge vortices in insect flight. *Nature*, 384, 1996.

[42] F-O. Lehmann and S. Pick. The aerodynamic benefit of wing-wing interaction depends on stroke trajectory in flapping insect wings. *Journal of experimental biology*, 210, 2007.

[43] S. P. Sane and M. H. Dickinson. The control of flight force by a flapping wing: lift and drag production. *Journal of experimental biology*, 204, 2001.

[44] S. P. Sane and M. H. Dickinson. The aerodynamic effects of wing rotation and a revised quasi-steady model of flapping flight. *Journal of experimental biology*, 205, 2002.

[45] K. D. Jones and M. F. Platzer. Numerical computation of flapping-wing propulsion and power extraction, 1997.

[46] M. V. Ol. Vortical structures in high frequency pitch and plunge at low reynolds number, 2007.

[47] A. Azuma and M. Okamoto. Theoretical study on two-dimensional aerodynamic characteristics of unsteady wings. *Journal of Theoretical Biology*, 234, 2005.

[48] T. Y-T. Wu. Hydromechanics of swimming propulsion. part 1. swimming of a twon-dimensional flexible plate at variable forward speeds in an inviscid fluid. *Journal of Fluid Mechanics*, 46, 1971.

[49] A. R. Ahmadi and S. E. Widnall. Energetics and optimum motion of acillating lifting surfaces of finite span. *Journal of Fluid Mechanics*, 162, 1986.

[50] B. C. Basu and G. J. Hancock. The unsteady motion of a two-dimensional aerofoil in incompressible inviscid flow. *Journal of Fluid Mechanics*, 87, 1978.

[51] H. Kagemoto, M. J. Wolfgang, D. K. P. Yue, and M. S. Triantafyllou. Force and power estimation in fish-like locomotion using a vortex-lattice method. *Journal of Fuids Engineering*, 2000.

[52] G. S. Winckelmans and A. Leonard. Contributions to vortex particle methods for the computation of three-dimensional incompressible unsteady flows. *Journal of Computational Physics*, 109, 1993.

[53] G-H. Cottet and P. Poncet. Advances in direct numerical simulations of 3d wall-bounded flows by vortex-in-cell methods. *Journal of Computational Physics*, 193, 2003.

[54] P. Koumoutsakos, A. Leonard, and F. Pepin. Boundary conditions for viscous vortex methods. *Journal of Computational Physics*, 113, 1994.

[55] P. Ploumhans and G. S. Winckelmans. Vortex methods for high-resolution simulations of viscous flow past bluff bodies of general geometry. *Journal of Computational Physics*, 165, 2000.

[56] P. Ploumhans, G. S. Winckelmans, J. K. Salmon, A. Leonard, and M. S. Warren. Votex methods for direct numerical simulation of three-dimensional bluff body flows: application to the sphere at re=300, 500, and 1000. *Journal of Computational Physics*, 178, 2002.

[57] P. Degond and S. Mas-Gallic. The weighted particle method for convection-diffusion equations. i: The case of an isotropic viscocity. ii: The anisotropic case. *Mathematics of Computation*, 53, 1989.

[58] J. D. Eldredge. Efficient tools for the simulation of flapping wing flows, 2005.

[59] G-H. Cottet and P. D. Koumoutsakos. *Vortex methods: theory and practice*. Cambridge University Press, 2000.

[60] Z. J. Wang. Numerical simulation of flapping-wing insect hovering flight at unsteady flow. *Journal of Fluid Mechanics*, 410, 2000.

[61] I. Akhtar, R. Mittal, G. V. Lauder, and E. Drucker. Hydrodynamics of a biologically inspired tandem flapping foil configuration. *Theoretical and Computational Fluid Dynamics*, 21, 2007.

[62] J. M. V. Rayner. Estimating power curves of flying vertebrates. *Journal of experimental biology*, 202, 1999.

[63] W. Z. Stepniewski. *Rotatory Wing Aerodynamics*. Dover, 1984.

[64] J. M. Wakeling and C. P. Ellington. Dragonfly flight, iii. lift and power requirements. *Journal of experimental biology*, 200, 1997.

[65] C. Van Den Berg and J. M. V. Rayner. The moment of inertia of bird wings and the inertial power requirement for flapping flight. *Journal of experimental biology*, 198, 1995.

[66] N. H. Teng. *The development of a computer code for the numerical solution of unsteady, inviscid and incompressible flow over an airfoil*. PhD thesis, Naval Postgraduate School, 1987.

[67] H. B. Keller and T. Cebeci. Accurate numeriical methods for boundary-layer flows, pt. 2, two dimensional turbulent flows. *AIAA Journal*, 10, 1972.

[68] D. F. Kurtulus, L. David, A. Farcy, and N. Alemdaroglu. Aerodynamic characteristics of flapping motion in hover. *Experiments in Fluids*, 2006.

[69] D. Zuo, S. Peng, W. Chen, and W. Zhang. Numerical simulation of flapping-wing insect hovering flight at unsteady flow. *International Journal for numerical methods in fluids*, 53, 2007.

[70] H. Liu, C. P. Ellington, K. Kawachi, C. Van Den Berg, and A. P. Willmott. A computational fluid dynamic study of hawkmoth hovering. *Journal of experimental biology*, 201, 1998.

[71] M. Sun and J. Tang. Unsteady aerodynamic force generation by a model fruit fly wing in flapping motion. *Journal of experimental biology*, 205, 2002.

[72] B. D. Coller and P. A. Chamara. Structural non-linearities and the nature of the classic flutter instability. *Journal of Sound and Vibration*, 277, 2004.

[73] A. M. O. Smith. The panel method: Its original development. *Applied computational aerodynamics*, 125, 1990.

[74] W. H. Press, S. A. Teukolsky, W. T. Vetterling, and B. P. Flannery. *Numerical Recipes in C++*. Cambridge University Press, 2003.

[75] T. Cebeci. *An Engineering Approach to the Calculation of Aerodynamic Flows*. Springer, 1999.

[76] J. M. Anderson, K. Streitlien, D. S. Barrett, and M. S. Triantafyllou. Oscillating foils of high propulsive efficiency. *Journal of Fluid Mechanics*, 360, 1998.

[77] A. Gharakhani and A. F. Ghoniem. Three-dimensional vortex simulation of time dependant incompressible internal viscous flows. *Journal of Computational Physics*, 134, 1997.

[78] K. Kamemoto. On contribution of advanced vortex element methods toward virtual reality of unsteady vortical flows in the new generation of cfd. *Journal of the Brazilian Society of Mechanical Sciences and Engineering*, 26, 2004.

[79] O. M. Knio and A. F. Ghiniem. Numerical study of a three-dimensional vortex method. *Journal of Computational Physics*, 86, 1990.

[80] L. Lan, J. Feng, F. Jian-ren, and C. Ke-fa. Recent development of vortex method in imcompressible viscous bluff body flows. *Journal of Zhejiang University SCIENCE*, 4, 2005.

[81] D. J. Lee. Numerical prediction of rotor tip-vortex roll-up in axial flights by using a time-marching free-wake method, 1999.

[82] D. J. Lee and S. U. Na. Numerical simulations of wake structure generated by rotating blades using a time marching, free vortex blob method. *European Journal of Mechanics*, 18, 1999.

[83] A. Leonard, P. Koumoutsakos, and G. Winckelmans. Vortex methods for three-dimensional separated flows, 1994.

[84] M. Nitsche and R. Krasny. A numerical study of vortex ring formation at the adge of a circulat tube. *Journal of Fluid Mechanics*, 276, 1994.

[85] J. H Strickland, G. F. Homicz, V. L. Porter, and A. A. Gossler. A 3-d vortex code for parachute flow predictions: version 1.0. Technical report, Sandia National Laboratories, 2002.

[86] S. G. Voutsinas. Vortex methods in aeronautics: how to make things work. *International Journal of Computational Fluid Dynamics*, 20, 2006.

[87] S. G. Voutsinas and D. G. Triantos. Aerodynamic and aeracoustic analysis of full helicopter configurations. Technical report, National Technical University of Athens.

[88] D. J. Willis, J. Peraire, M. Drela, and J. K. White. A numerical exploration of parameter dependance in power optimal flapping flight, 2006.

[89] Q. Zhu, M. J. Wolfgang, D. K. P. Yue, and M. S. Triantafyllou. Three-dimesnional flow structures and vorticity control in fish-like swimming. *Journal of Fluid Mechanics*, 468, 2002.

Biography

Sidney Lebental was born May 1, 1982 in Paris, France, to Annick and Jacques Lebental. After graduating from Saint-Michel High School in Saint-Mande, France, in 2000, he obtained a M.S. in engineering from the Ecole Centrale de Lyon in 2005. He then received his M.S. from Duke University in 2006 and his thesis was entitled, Cavitation onset prediction and verification on rudders with leading edge tubercles. This dissertation fulfills the requirements of Ph.D. in mechanical engineering from Duke University, which she obtained in 2008 under the advisement of Dr. Kenneth C. Hall. His research interests include unsteady computational fluid dynamics (CFD); aeronautics; aeroelasticity.